JOURNAL OF THE AERONAUTICAL SCIENCES

UNIVERSITY OF MICHIGAN
APR 20 1954
ENGINEERING LIBRARY

VOLUME 21 APRIL, 1954 NUMBER 4

CONTENTS

The Ultimate Strength of Aluminum-Alloy Formed Structural Shapes in Compression. . . . . ROBERT A. NEEDHAM 217

Linearized Theory of the Oscillating Airfoil in Compressible Subsonic Flow. . . . . R. TIMMAN 230

Calculation of Compressible Cascade Flow by the Method of Flux Analysis. . . . . SHIGEO UCHIDA 237

A Vector Method Approach to the Analysis of the Dynamic Lateral Stability of Aircraft. . . . . L. STERNFIELD 251

Results of Some Base Pressure Experiments at Intermediate Reynolds Numbers with $M = 2.84$. . . . . L. L. KAVANAU 257

The Flow over a Flat Plate with a Small Angle of Attack at Mach Number 1. . . . . GOTTFRIED GUDERLEY 261

Readers' Forum: "An Exact Solution for Two-Dimensional Linear Panel Flutter at Supersonic Speeds," by Martin Goland and Yudell L. Luke; "Nose Shapes for Minimum Pressure Drag at Supersonic Mach Numbers," by Leland H. Jorgensen; "Streamline Curvature Effects for Finite Wings in Wind Tunnels," by Alan Pope; "Wind-Tunnel Model Position for Transonic Testing," by Alan Pope; "Similar Solutions of Compressible Laminar Boundary-Layer Equations," by Clarence B. Cohen; "The Method of Superposition of Planar Wave Systems," by Wallace D. Hayes; "Comments On 'Ripple-Type Buckling of Sandwich Columns,'" by Paul Seide; "Spin Effect on Base Pressure of Cone-Cylinders," by R. Lehnert and S. M. Hastings; "Buckling Loads for Columns of Variable Cross Section," by B. E. Gatewood. 275–288

Published by
INSTITUTE OF THE AERONAUTICAL SCIENCES, INC.

JOURNAL OF THE AERONAUTICAL SCIENCES

Editor: HUGH L. DRYDEN, *Director, NACA*

Associate Editor: ROBERT R. DEXTER *Managing Editor:* BERNEICE H. JARCK

Editorial Committee

Aerodynamics

Francis Clauser
Howard Emmons
Antonio Ferri
Alexander Flax
R. Paul Harrington
R. T. Jones
Carl Kaplan
H. W. Liepmann
C. C. Lin
H. F. Ludloff
Harold Luskin
John R. Markham
Clark B. Millikan
Shatswell Ober
W. Bailey Oswald
Allen E. Puckett
Elliott G. Reid
H. J. E. Reid
Russell Robinson
G. B. Schubauer
W. R. Sears
John Stack
Theodore Theodorsen
Theodore von Kármán

Air Transport

Charles Froesch
J. A. Herlihy
R. D. Kelly
Otto E. Kirchner
Jerome Lederer
John C. Leslie
R. Dixon Speas

Flight Testing

W. K. Ebel
R. R. Gilruth
Melvin N. Gough
E. G. Stout

Structures and Materials

W. B. Bleakney
E. W. Conlon
L. H. Donnell
E. C. Hartmann
N. J. Hoff
Samuel Levy
E. E. Lundquist
Alfred S. Niles
W. Ramberg
F. R. Shanley
H. W. Sibert
C. R. Strang
S. Timoshenko
H. S. Tsien
Chi-Teh Wang

Rotating Wing Aircraft

F. B. Gustafson
K. H. Hohenemser
Bartram Kelley
R. B. Maloy
Ralph McClarren
R. H. Miller
R. H. Prewitt
Igor I. Sikorsky

Vibration and Flutter

Lee Arnold
M. A. Biot
R. L. Bisplinghoff
William Bollay
Chieh-Chien Chang
J. P. Den Hartog
I. E. Garrick
Martin Goland
Theodore Theodorsen

Aircraft Design

W. E. Beall
W. K. Ebel
Hall L. Hibbard
Richard Hutton
C. L. Johnson
A. A. Kartveli
C. J. McCarthy
Fred E. Weick
Robert J. Woods

Electronics in Aviation

K. C. Black
E. F. Herzog
David S. Little
D. K. Martin
George Rappaport
Paul Rosenberg
L. M. Sherer

Physiologic Problems

H. G. Armstrong
Louis H. Bauer
Robert J. Benford
Eugene Du Bois
W. Randolph Lovelace, II
Ross A. MacFarland

Fuels and Oils

D. P. Barnard
J. H. Doolittle
Graham Edgar
R. T. Goodwin
S. D. Heron
A. M. Rothrock

Flight Propulsion

George W. Brady
Frank W. Caldwell
L. S. Hobbs
E. E. Johnson
Joseph Keenan
R. P. Kroom
Hans Reissner
Abe Silverstein
C. Fayette Taylor
E. S. Taylor
P. Taylor
E. S. Thompson
H. S. Tsien

Instruments

Allan G. Binnie
J. R. Bradburn
Charles H. Colvin
C. S. Draper
S. G. Eskin
O. E. Esval
H. W. Holzapfel
W. L. Howland
George H. Purcell
C. F. Savage
O. Hugo Schuck
C. L. Seward, Jr.
L. D. Statham
R. C. Sylvander
D. K. Warner

Meteorology

C. F. Brooks
D. M. Little
E. J. Minser
F. W. Reichelderfer
H. C. Willett

SUBSCRIPTION RATES

JOURNAL OF THE AERONAUTICAL SCIENCES, Published Monthly.—United States and Possessions: 1 Year, $12.00; Single Copies, $1.50. Foreign Countries Including Canada (American Currency Rates): 1 Year, $13.00; Single Copies, $1.50.

AERONAUTICAL ENGINEERING REVIEW, Published Monthly.—United States and Possessions: 1 Year, $3.00; Single Copies, $0.50. Foreign Countries Including Canada (American Currency Rates): 1 Year, $3.50; Single Copies, $0.50.

Notices of change of address should be sent to the Institute at least 30 days prior to actual change of address.

Manuscripts for publication, proofs, and all correspondence should be addressed to the Editorial Office of the JOURNAL.

Correspondence regarding subscriptions may be addressed to Publication Office, 20th and Northampton Sts., Easton, Pa., or to the Editorial Office of the JOURNAL OF THE AERONAUTICAL SCIENCES, 2 East 64th Street, New York 21, New York.

Copyright, 1954, by the Institute of the Aeronautical Sciences, Inc

Entered as Second Class Matter at the Post Office, Easton, Pa., May 1, 1937. Acceptance for mailing at a special rate of Postage provided for in the Act of August 24, 1912. Authorized April 29, 1937.

VOL

T
P

A n
stress
presen
that a
elemen
variou
ing.
is obta
gle sec
structu

Emp
basic
mately
75S-T
ysis w
agreem
to be v

a
A
b
b'
b_e
C_c
E
f_{ss}
F_{cc}
F_{cr}
F_{cy}
k
R
t

Rec
* A
for the
of Cali
† As

JOURNAL OF THE AERONAUTICAL SCIENCES

VOLUME 21 APRIL, 1954 NUMBER 4

The Ultimate Strength of Aluminum-Alloy Formed Structural Shapes in Compression*

ROBERT A. NEEDHAM†

University of California at Los Angeles

ABSTRACT

A new method of predicting the maximum average (crippling) stress of formed sheet-metal structural shapes in compression is presented. The proposed method is based on the assumption that a formed structural shape consisting of a series of flat plate elements can be treated as a series of angle sections possessing various degrees of edge support parallel to the direction of loading. A weighted crippling stress of the formed structural shape is obtained by summing the crippling loads of the individual angle sections and dividing this summation by the gross area of the structural shape.

Empirical equations for predicting the crippling stress of the basic angle sections were obtained from the analysis of approximately 200 tests of formed angles and channels of 24S-T3 and 75S-T6 aluminum-alloy sheet. The proposed method of analysis was applied to 24 typical aircraft stringer shapes. The agreement of the predicted and test crippling stresses was found to be very good.

NOTATION

a = width of channel or angle flange, in.
A = area, sq.in.
b = width of flat plate or half width of channel web, in.
b' = equivalent width, $(a + b)/2$, in.
b_e = effective width, in.
C_e = crippling coefficient for angle section
E = Young's modulus, lbs. per sq.in.
f_{se} = stress at junction of flat plate elements, lbs. per sq.in.
F_{ce} = crippling or maximum average stress, lbs. per sq.in.
F_{cr} = critical plate buckling stress, lbs. per sq.in.
F_{cy} = compression yield stress, lbs. per sq.in.
k = plate buckling coefficient
R = bend radius, in.
t = sheet thickness, in.
η = effective modulus ratio, dimensionless
μ = Poisson's ratio, dimensionless

Received October 15, 1953.

* A thesis submitted in partial satisfaction of the requirements for the degree Master of Science in Engineering at the University of California at Los Angeles, September, 1953.

† Associate Research Engineer.

INTRODUCTION

THE PRIMARY STRUCTURE of the modern airplane usually contains many wide, thin plate elements loaded in compression. Thin-walled round, square, and rectangular tubes and flat or curved sheet to which are riveted formed or extruded structural shapes are but a few of the examples of this type of construction. These members are analyzed as columns.

As the length of a column of compact cross section decreases, the stress at primary failure increases, and the failure stress is accurately predicted by the Euler equation employing the tangent modulus.[17] If, however, the cross section of the column is made up of thin plate elements, the stress at failure will be modified by localized plate buckling of these elements. When the column slenderness ratio is large, the stress for general column failure is less than that at which plate buckling takes place, and the Euler equation predicts correctly the failure stress. As the slenderness ratio decreases, a point is reached at which the stress for general column failure and the stress at which a plate element of the column cross section becomes unstable will be equal. It is at this point that the experimental column curve begins to depart from the theoretical column curve. Failure above this point is an interaction of general and local failure. In the short column range (slenderness ratios in the order of 20), failure is due almost entirely to the plate buckling phenomenon—i.e., the column strength is not materially affected by length. The stress in this region is the upper allowable of the column stress and is variously referred to as the *crippling*, *crushing*, or *maximum average* stress.

Plate Buckling

When flat plates are subjected to edge compression, the critical stress at which the plate becomes unstable and buckles is expressed by the well-known relationship

$$F_{cr}/\eta = k\pi^2 Et^2/12(1 - \mu^2)b^2 \qquad (1)$$

The nondimensional coefficient, η, takes into account the reduction of the modulus of elasticity for stresses above the elastic range. Methods of evaluating η are discussed in reference 1. Eq. (1) may be used to predict the stress at which a flat plate will buckle, provided the degree of edge fixity of the plate is known. Thin-walled equal angles and square tubes are examples of structural shapes with known boundary conditions. Thin-walled zee and channel sections are also examples of structural shapes for which the buckling coefficients are known. In these cases, however, the buckling coefficients vary with the ratio of the flange width to the back width, and Eq. (1) is written as

$$\frac{F_{cr}}{\eta} = \frac{k_w \pi^2 Et^2}{12(1 - \mu^2)b^2} = k_w' E(t/b)^2 \qquad (2)$$

Values of k_w are obtained from charts such as shown in Fig. 1.[2]

The National Advisory Committee for Aeronautics has conducted extensive investigations in order to determine plate compressive strengths of a number of aircraft structural materials. The results of these tests are summarized in reference 3. An obvious and highly significant fact brought out by these tests was that the maximum stress developed by the sections tested was always higher than the stress at which plate buckling occurred. In the discussion that follows, the maximum average stress developed by a structural shape will be referred to as the *crippling stress*. Existing methods of predicting this stress will be discussed, and, finally, a new method of crippling stress prediction, based on the results of over 200 tests, will be presented.

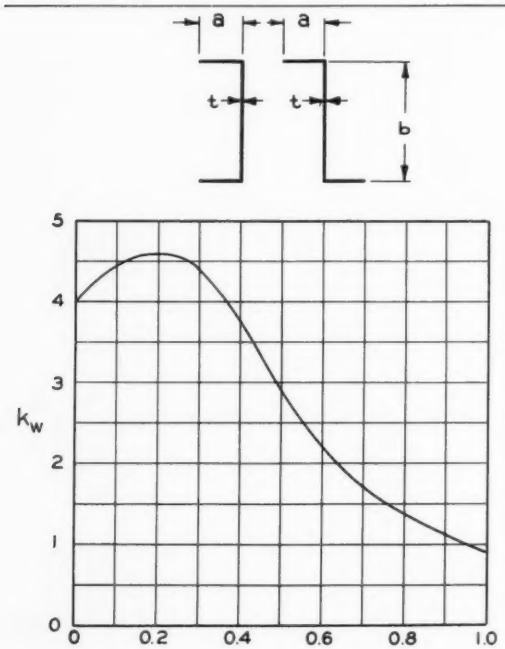

FIG. 1 - K_W FOR BUCKLING OF Z-, AND [-SECTIONS

Existing Methods of Predicting Crippling Stresses

Early in the development of thin-sheet structural analysis techniques, a method of crippling stress prediction proposed by several authors was that of subdividing a given cross section into a series of flat plate elements. The elements were assumed to possess various degrees of edge support, usually hinged. The buckling load for each element was calculated from Eq. (1) ($\eta = 1.0$) and the area of the element. The crippling stress of the section was taken as the summation of the buckling loads of the individual elements divided by the total area of the section. (See, for example, reference 4.) There are two obvious discrepancies in this technique. After buckling of contiguous flat elements of a structural shape, narrow strips along the junctions of the plate elements continue to support load and, actually, may permit the section to carry load several times greater than the theoretical buckling load of the strongest flat plate element of the cross section. Further, the assumption that adjacent elements provide mutual support equivalent to simply supported (hinged) edges is often overconservative.

A method of crippling stress prediction that has found wide usage in the aircraft industry was proposed by Crockett[5] in 1942. The method is empirical and is based on design curves that are trial-and-error variations of the theoretical to give the best possible agreement with test data (see reference 5, page 501). Crockett's method of crippling stress prediction is somewhat the same as the technique outlined above—that is, the method consists of summing the crippling loads of the components and dividing by the section area to obtain the crippling stress. In the Crockett method, however, the crippling stress of curved elements, formed at the junctions of the flat plate elements, is accounted for. The principal disadvantage of this method lies in the fact that a considerable amount of computation time is involved in analyzing complex shapes.

Schuette[6] has made a comprehensive study of the results of the NACA channel- and zee-section crippling strength tests. According to his findings, the crippling stress of formed sheet-metal sections of 17S-T and 24S-T aluminum alloys may be expressed by

$$F_{cc}/F_{cr} = K(F_{cr}/F_{cy})^{-0.75} \qquad (3)$$

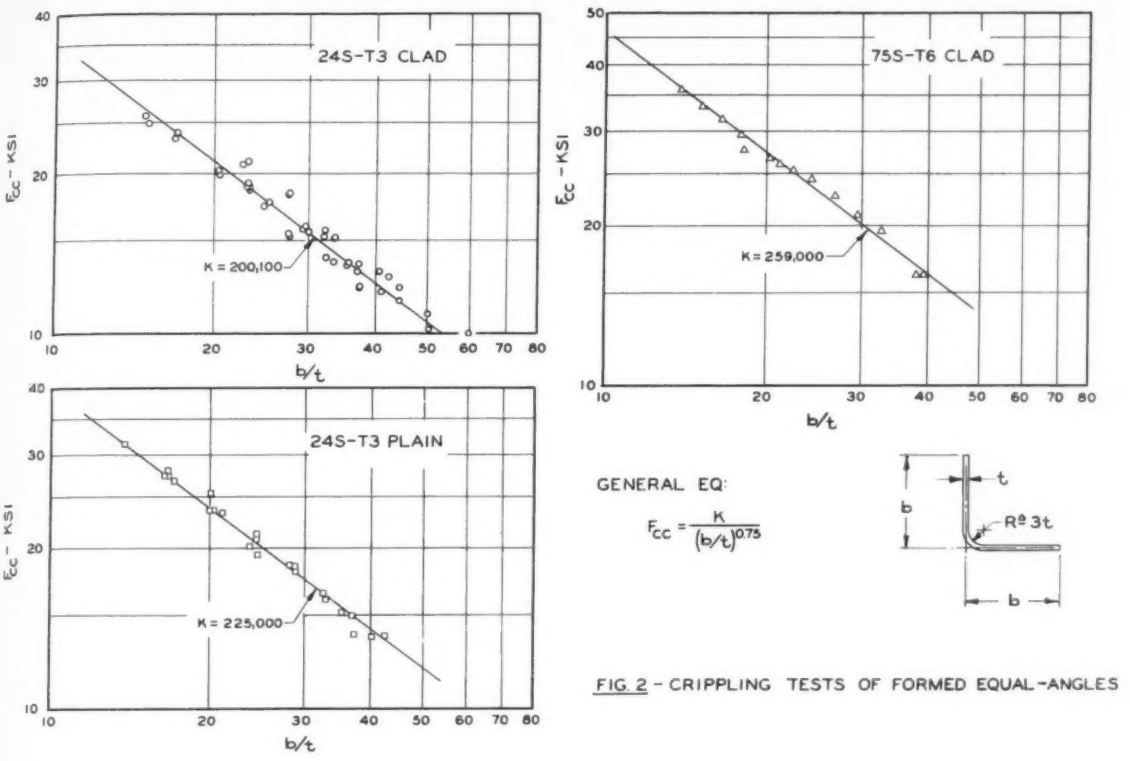

FIG. 2 - CRIPPLING TESTS OF FORMED EQUAL-ANGLES

Eq. (3) was derived from logarithmic plots of F_{cc}/F_{cr} against F_{cr}/F_{cy}. Here, as before, the critical stress, F_{cr}, is the stress at the start of plate buckling and may be calculated from Eq. (1). The coefficient, K, was introduced to account for the fact that the ratio F_{cc}/F_{cr} is also a function of the b/t ratio of the section (Fig. 1). The variation of K with b/t is given in Table I.

TABLE I
(From Reference 6, Page 6)

b/t	20	30	40	50	100
K	0.90	0.82	0.75	0.71	0.63

The values of K given in this table apply to plates formed at the edges to an inside bend radius of three times the sheet thickness (see reference 6, page 6).

Schuette's equations were used by The Dow Chemical Company in preparing a set of crippling stress curves for magnesium-alloy formed structural shapes.[7]

A New Method of Crippling Stress Prediction

The various methods of crippling stress prediction just discussed are all based on the assumption that a structural shape can be treated as a series of isotropic flat plate elements, the strengths of which can be predicted by the classical buckling equations. It is well established, however, that substantial increases in the compression yield stress occur in the vicinity of bend lines of formed shapes. In some aluminum alloys this increase may amount to as much as 25 per cent over the yield stress of the unformed sheet.[8] A flat element of a formed structural shape then becomes, in effect, a plate possessing variable mechanical properties normal to the direction of loading, and there are no provisions in the plate buckling equations for this effect.

It occurred to the writer that a more rational approach to the problem of predicting crippling stresses could be effected by considering the basic structural element as an angle section rather than a plate. Further, it was believed that the strength of these angle sections could be established experimentally in such a way that the local increase in yield stress at the bend, brought about by cold-forming the shape, could be accounted for. Observations of tests of formed sheet-metal shapes in compression indicate that initial instability starts with the flat plate elements and that complete failure of the section occurs when the buckle pattern passes through the bends. Hence, if the edges of the flanges of the basic angle section are taken to the centers of contiguous flat plate elements (see, for example, Fig. 5b), the "cut" is made at the least sensitive region of the plate.

A series of tests was conducted on formed 24S-T3 plain (unclad), and 24S-T3 and 75S-T6 clad, aluminum-alloy equal and unequal angles and channels as part of a test program to establish crippling stress equations. Because of the large number of tests conducted (over 200), tabulated results have not been included in this paper. All specimens were formed

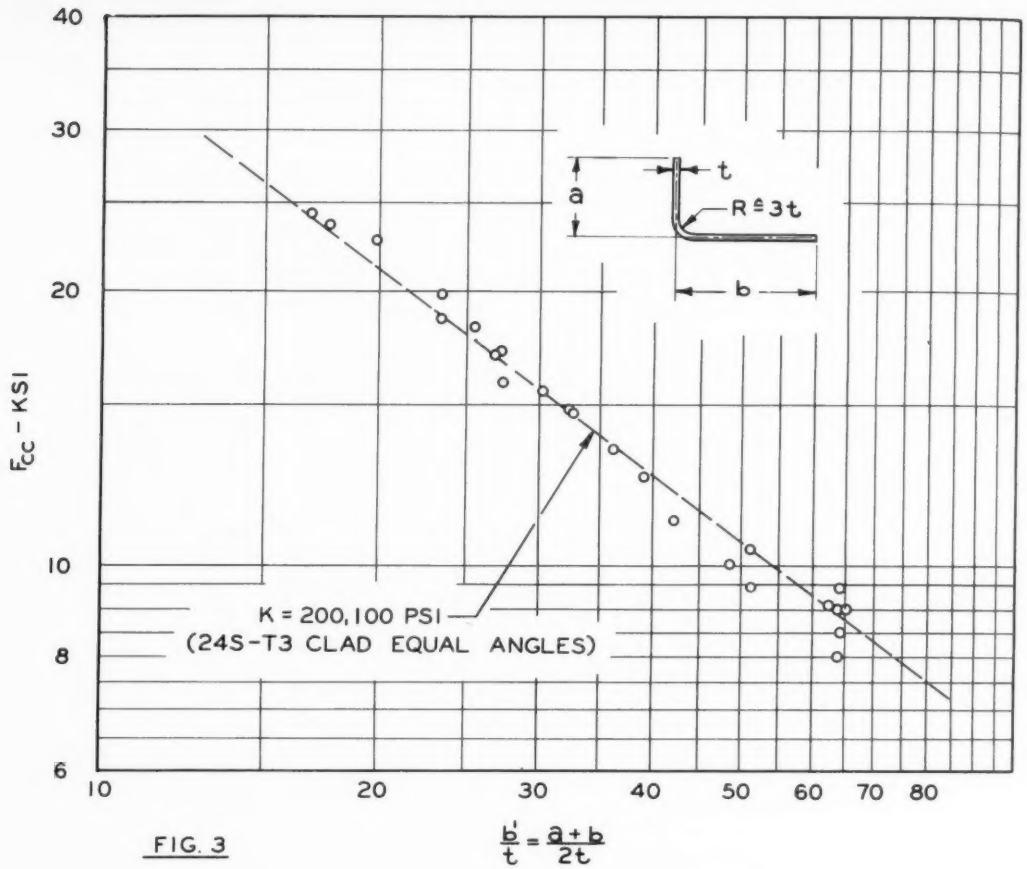

FIG. 3

on a leaf brake and had inside bend radii of approximately three times the sheet thickness. The specimens were cut to a length corresponding to a pin-ended slenderness ratio of approximately 20. The ends of the specimens were ground flat and parallel, and areas were calculated from the weights and lengths of the specimens using a material density of 0.100 lb. per cu.in.

The tests of this series were made in a Tinius-Olsen hydraulic testing machine having a maximum capacity of 120,000 lbs. and an intermediate load range of 20,000 lbs. The machine had been calibrated just prior to the start of the test program, and it is believed that the errors in the load readings were less than ±1 per cent of the load range used. The specimens were tested flat-ended with the ends of the sections bearing directly on the guided platens of the machine. Maximum care was exercised in obtaining uniform contact of the ends of the sections and the testing machine platens, and in some instances it was necessary to regrind the ends of the specimens to ensure good contact. The maximum load reached in the test was recorded, and this load divided by the gross area of the section was taken as the experimental crippling stress.

The first group of sections tested consisted of 78 equal angles. Logarithmic plots of crippling stress, F_{cc}, against the parameter b/t are shown in Fig. 2. The solid lines on the plot represent least square fits of equations of the form

$$F_{cc} = k/(b/t)^{0.75} \tag{4}$$

where k, the stress intercept, is as follows:

24S-T3 clad:	k = 200,100 lbs. per sq.in.
24S-T3 plain:	k = 225,000 lbs. per sq.in.
75S-T6 clad:	k = 259,000 lbs. per sq.in.

In Eq. (4) the flange width b is measured to the centerline of the adjacent web. The experimental scatter appears to be random and is characteristic of compression tests of thin-sheet sections.

The majority of structural shapes that are of interest are made up of angle sections with unequal leg widths. Here, a suitable buckling parameter may be defined by

$$b'/t = (a + b)/2t$$

Thus, b'/t will be referred to as the "equivalent" b/t and is simply the average flange width, $(a + b)/2$, divided by the sheet thickness. Fig. 3 is a plot of the tests of 24 unequal angles of 24S-T3 clad aluminum. Here, the abscissa is the equivalent b/t of the sections as defined above. Included also is the curve for 24S-T3 clad equal angles of Fig. 2. The agreement of the two sets of data is good and definitely establishes

$(a + b)/2t$ as a suitable parameter for the buckling of unequal angles.

The excellent agreement of the two sets of tests just discussed immediately pointed to the possibility of treating a symmetrically formed channel as two unequal angles supported at the midpoint of the web. The effective b/t of the section would then be, as in the case of the unequal angle, $(a + b)/2t$. Here, the dimension b is the half-width of the web of the channel. Fig. 4 includes logarithmic plots of the channel tests for the three materials investigated. In all three cases the test data yield equations analogous to Eq. (4), the only difference being in the constants k, which, in the case of the channels, are higher than the corresponding k-values for the angles. This is obviously due to the fact that the "channel angles" were restrained along one unloaded edge, whereas the angle sections were not. The k-values for the channels are as follows:

24S-T3 clad: $k = 221,300$ lbs. per sq.in.
24S-T3 plain: $k = 244,000$ lbs. per sq.in.
75S-T6 clad: $k = 272,000$ lbs. per sq.in.

The above results are based on the results of 127 tests. The 24S-T3 and 75S-T6 clad specimens (98 tests) were conducted by the writer, while the 24S-T3 plain channel test data were taken from reference 9. The range of sheet gages covered in both the angle and channel tests is listed in Table II.

TABLE II

Material	Shape	Sheet Gages Tested
24S-T3 Clad	Equal angles	0.016, 0.020, 0.025, 0.032, 0.040, 0.051
	Unequal angles	0.032, 0.040, 0.051
	Channels	0.016, 0.020, 0.032, 0.040, 0.051
24S-T3 Plain	Equal angles	0.025, 0.032, 0.040, 0.051
	Channels	0.102
75S-T6 Clad	Equal angles	0.040, 0.051, 0.072
	Channels	0.025, 0.040, 0.051

Formed sheet-metal structural shapes appear in a variety of forms such as zee's, lipped channels, and hats, and presenting empirical crippling stress curves for such a variety of structural sections is a practical impossibility. It is interesting to note, however, that many of these shapes can be considered as being made up of a series of unequal angle sections with various degrees of edge support. Consider, for example, the unbalanced zee-section shown in Fig. 5b. This shape is made up of three unequal angles. Elements 1 and 3 are unequal angles that are supported on one unloaded edge and free on the other, while element 2 is an unequal angle that is supported on both unloaded edges. (Included also in Fig. 5 is the method of subdividing the shape as proposed by Crockett in reference 5.) If it is assumed that the crippling load of the entire shape is equal to the summation of the crippling loads of the three angles, the weighted crippling stress will be given

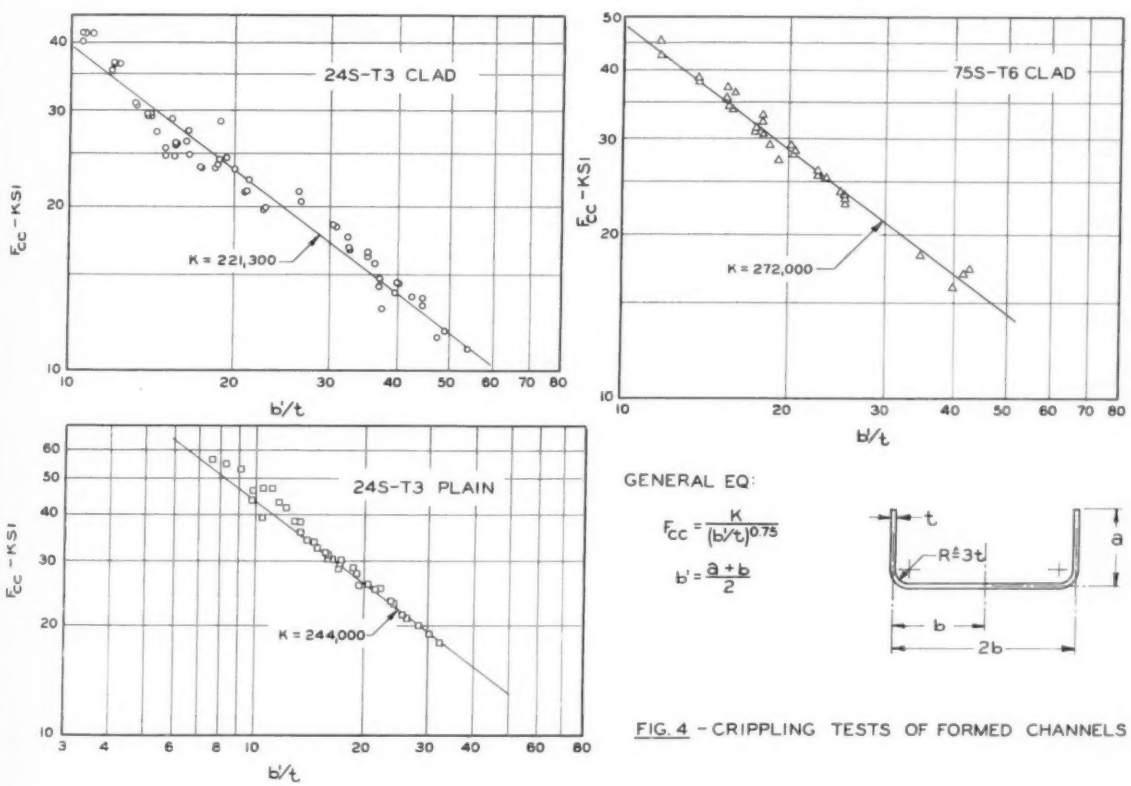

FIG. 4 - CRIPPLING TESTS OF FORMED CHANNELS

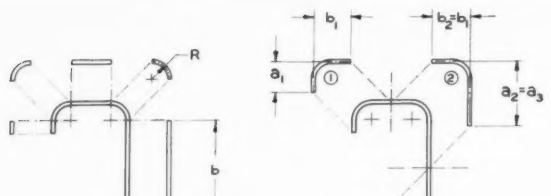

(a) - CROCKETT METHOD (b) - AUTHOR'S METHOD

FIG. 5 - SUBDIVISION OF SECTION FOR CRIPPLING ANALYSIS

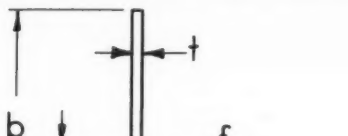

FIG. 6 - IDEALIZED ANGLE-SECTION

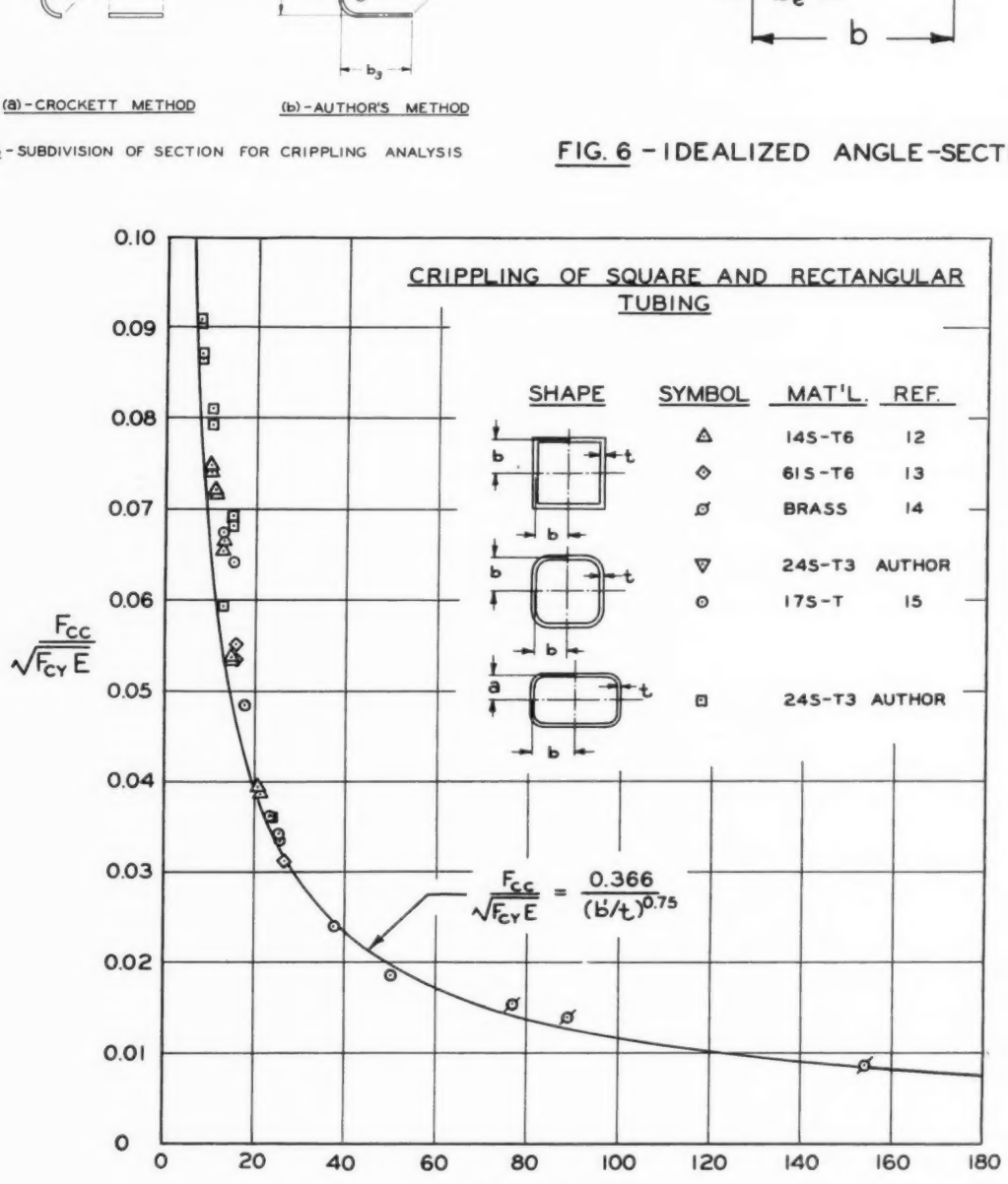

FIG. 7 - COMPARISON OF CRIPPLING TESTS WITH EQ. (15)

by

$$F_{cc} = \frac{\sum \text{(crippling loads of angles)}}{\sum \text{(area of angles)}}$$

The above discussion assumes that equations are available to predict the crippling strength of unequal angles possessing support along both unloaded edges (no edge free). Empirical equations for this condition of support could be obtained from tests. Such a procedure is not necessary, however, if the rational assumption is made that the percentage increase in crippling strength of the no-edge-free angle over the one-edge-free angle is the same as the increase of the one-edge-free angle over the angle with both unloaded edges free. For example, consider the angle and channel tests of the 24S-T3 clad alloy of Figs. 2 and 4. Thus,

$$k_{\text{no edge free}} = 221,300 + (221,300 - 200,100)$$
$$= 242,500 \text{ lbs. per sq.in.}$$

The stress intercept values for the three materials investigated in this paper are listed in Table III.

TABLE III
Stress Intercept (k) Values for $F_{cc} = k/(b'/t)^{0.75}$

Material	k (Two Edges Free)	k (One Edge Free)	k (No Edge Free)
24S-T3 Clad	200,100	221,300	242,500
24S-T3 Plain	225,000	244,000	263,000
75S-T6 Clad	259,000	272,000	285,000

DISCUSSION

The fact that the experimental plots of F_{cc} against b'/t of Figs. 2, 3, and 4 all follow a 0.75 power law is intriguing. One possible explanation for this may be found by considering the sections in the light of effective width theories.

According to von Kármán,[10] the major portion of the load supported by a thin plate in edge compression is carried by narrow strips along the edges parallel to the direction of loading of the plate. These "effective widths" of sheet, acting at a uniform edge stress, f_{se}, take the place of the total sheet width in considering the ultimate strength of the plate. The original equation suggested by von Kármán for calculating these effective widths is

$$b_e = kt\sqrt{E/f_{se}} \tag{5}$$

The constant, k, in Eq. (5) depends upon the degree of edge support along the unloaded edges of the plate. If this equation is applied to the equal-angle section of Fig. 6 and if it is assumed that the edge at the junction of the two legs of the angle is hinged, $k = 0.60$, and the total load supported by the angle is

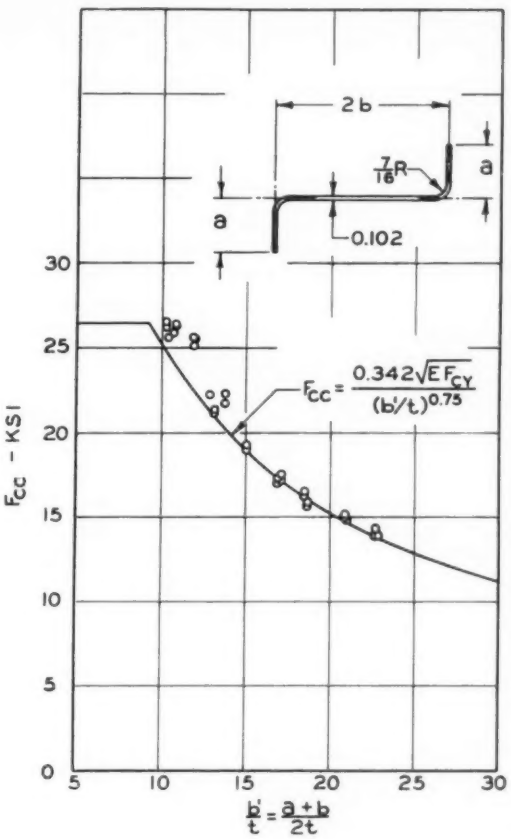

FIG. 8 - CRIPPLING OF FS-1h MAG. ALLOY ZEE'S

$$P_{cc} = f_{se}2b_e t = 1.20 f_{se} t^2\sqrt{E/f_{se}}$$

and since the area of the angle is $2bt$, the average crippling stress is

$$F_{cc} = P_{cc}/2bt = 0.60(t/b)\sqrt{f_{se}E}$$

or

$$F_{cc} = k_1/(b/t) \tag{6}$$

where $k_1 = 0.60\sqrt{f_{se}E}$. In reference (11) Marguerre proposes the equation

$$2b_e = b\sqrt[3]{F_{cr}/f_{se}} \tag{7}$$

as the expression for the total effective width. Here, F_{cr} is the critical edge stress of the plate. If it is again assumed that the edges of the plate elements of the angle of Fig. 6 are simply supported, $F_{cr} = 0.4E(t/b)^2$, and the crippling stress is given by

$$F_{cc} = k_2/(b/t)^{3/2} \tag{8}$$

where $k_2 = 0.37\sqrt[3]{f_{se}^2 E}$. Thus Eqs. (6) and (8), based on the effective width equations of von Kármán and Marguerre, yield exponents for the b/t ratio that bracket the experimentally derived value of 0.75.

Eq. (3) of this paper is an expression for the crippling strength of zee and channel sections derived by Schuette

TABLE IV

Material	F_{cy}	E	$\sqrt{F_{cy}E}$	Values of C: Two edges free	One edge free	No edge free
24S-T3 Clad sheet $t \leq 0.051$	42,000	10,000,000	653,000	0.307	0.339	0.372
24S-T3 Plain (unclad)	45,100	10,500,000	694,000	0.324	0.352	0.379
75S-T6 Clad sheet $t > 0.032$	66,200	10,000,000	814,000	0.318	0.334	0.350
			Average values	0.316	0.342	0.366

from NACA test data. The coefficient K is a function of the b/t ratio of the section (here, b is the width of the web of the zee or channel section). Values of K for various b/t ratios are given in Table I. The variation of K with b/t given in this table can be expressed closely by the equation

$$K = 1.90/(b/t)^{0.25} \tag{9}$$

Substituting Eq. (9) in Eq. (3) and solving for F_{cc},

$$F_{cc} = 1.90 F_{cr}^{0.25}/(b/t)^{0.25}\, F_{cy}^{-0.75} \tag{10}$$

But, from Eq. (2), $F_{cr} = k'\eta E(t/b)^2$, and Eq. (10) becomes

$$F_{cc} = C'/(b/t)^{0.75} \tag{11}$$

The coefficient C' is a function of the effective modulus of elasticity, the flange-web ratio, and the mechanical properties of the material. It is interesting to note, however, that Schuette's equation for crippling is of the same general form as Eq. (4) obtained by the writer.

In the preceding discussion, certain similarities between the empirical crippling equation proposed by the writer and those of other investigators have been pointed out. In the light of this discussion, it may be reasonably concluded that the variation of crippling stress with the b'/t ratio for angle sections possessing various degrees of edge support is correctly expressed by equations of the form

$$F_{cc} = k/(b'/t)^n \tag{12}$$

The exponent n has been assigned a value of 0.75, which, while not necessarily the value for best fit of the test results, is at least sufficient for the present purposes. There remain, however, two questions to be answered with regard to Eq. (12). The first question is that of the physical significance of the constant k. The effective width investigations based on the equations of von Kármán and Marguerre [Eqs. (5) and (7)] suggest the form of k to be

$$k = C \sqrt[m]{f_{se}^{m-1} E} \tag{13}$$

Assuming a value of m of 2 and letting $f_{se} = F_{cy}$,

$$k = C \sqrt{F_{cy} E}$$

and Eq. (12) becomes

$$F_{cc} = C \sqrt{F_{cy} E}/(b'/t)^{0.75} \tag{14}$$

The writer has studied the results of compression stress-strain tests of several investigators, and as a result of these studies, average values of F_{cy} and E for the three materials covered in this paper were found to be as listed in Table IV. Values of C in Eq. (14) are also listed in Table IV for the various degrees of edge support. It is significant that the variations of C are in no case greater than 8 per cent for given edge conditions. If it is assumed that this variation is attributable to inaccuracies in arriving at the values of k from test, a single set of dimensionless crippling stress equations is obtained by taking the average values of C listed in Table IV. The equations, applicable to all three materials, are

$$F_{cc}/\sqrt{F_{cy}E} = C_e/(b'/t)^{0.75} \tag{15}$$

where

$C_e = 0.316$ (two edges free)
$C_e = 0.342$ (one edge free)
$C_e = 0.366$ (no edge free)

The second question brought out by the foregoing discussion arises from the assumption upon which the no-edge-free curves are based—namely, that the percentage increase in crippling strength of the no-edge-free angle over the one-edge-free angle is the same as the increase of the one-edge-free angle over the angle with both unloaded edges free. Evidently, for this assumption to be correct, correlation between the no-edge-free curve and crippling tests of square and rectangular tubes should exist. Table V contains the results of crippling tests of square tubes obtained from references 12 to 15, together with additional tests on both square and rectangular tubes of 24S-T aluminum alloy conducted by the writer. Fig. 7 is a plot of Eq. (15) for the case where $C_e = 0.366$ (no edge free). Included on this plot are the test results listed in Table V. It will be observed that the agreement of Eq. (15) with the test results is very good for b'/t values above 20. Below this value, Eq. (15) exhibits a considerable degree of conservatism with respect to the tests. It is interesting to note, also, that good agreement exists for materials and alloys other than those upon which Eq. (15) was developed.

An additional check (Fig. 8) on Eq. (15) was obtained by a comparison with the crippling tests on FS-1h magnesium-alloy formed zee sections conducted by Gallaher.[16] Here, $C_e = 0.342$ (angles with one edge free), and for the FS-1h material, $E = 6{,}500$ kips per sq.in. and $F_{cy} = 26.3$ kips per sq.in. Again, good agreement between test and theory exists.

Design Curves

A design chart based on Eq. (15) is shown in Fig. 9. It will be noted upon examination of the logarithmic plots of the angle and channel tests (Figs. 2, 3, and 4) that few of the sections tested possessed b'/t values below 10. Further, the power equation, Eq. (15), is of hyperbolic form and is asymptotic with the zero b'/t ordinate at an infinite stress. Since the available test data furnished no clue as to the nature of the true crippling stress curve below b'/t values of about 10, the upper limit of the crippling stress was arbitrarily fixed at the yield stress of the material (0.2 per cent offset method). The yield stress cutoffs for the dimensionless crippling stress curves of Fig. 9 would be obtained by substituting F_{cy} for F_{cc} in Eq. (15) and solving for the cutoff $(b'/t)_0$. Thus,

$$(b'/t)_0 = C_e^{4/3} (E/F_{cy})^{2/3} \qquad (16)$$

and it is seen that the yield stress cutoff varies somewhat with the edge support condition. Inasmuch as this variation is small, an average cutoff is used in lieu of the three cutoffs dictated by Eq. (16).

The design chart of Fig. 9 can be placed in a more useful form by plotting dimensionless crippling load against b'/t. The area of an unequal angle section of flange widths a and b, and inside bend radius R is given by

$$A = [(b'/t) - 0.214(R/t)]2t^2 \qquad (17)$$

where, as before, $b'/t = (a + b)/2t$. The crippling load of the angle is, from Eq. (15),

$$P_{cc} = [C_e \sqrt{F_{cy}E}/(b'/t)^{0.75}] A$$

- TABLE V -

CRIPPLING TESTS OF SQUARE AND RECTANGULAR TUBES

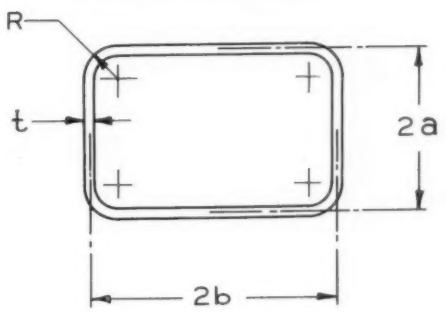

TABLE V

Material and Reference	2a (In.)	2b (In.)	t (In.)	R (In.)	b'/t	E (Kips per Sq.In.)	F_{cc} (Kips per Sq.In.)	F_{cy} (Kips per Sq.In.)	$\frac{F_{cc}}{\sqrt{F_{cy}E}}$
14S-T6[12]	6.85	6.85	0.158	0.094	21.6	10,700	31.6	62.2	0.0388
14S-T6[12]	6.85	6.85	0.158	0.094	21.6	10,700	31.5	62.2	0.0387
14S-T6[12]	4.83	4.83	0.153	0.094	15.8	10,700	43.5	61.4	0.0537
14S-T6[12]	4.84	4.84	0.156	0.094	15.5	10,700	43.2	61.4	0.0532
14S-T6[12]	4.09	4.09	0.154	0.094	13.3	10,700	53.9	63.2	0.0656
14S-T6[12]	4.09	4.09	0.154	0.094	13.3	10,700	54.7	63.2	0.0665
14S-T6[12]	3.58	3.58	0.153	0.094	11.7	10,700	57.6	60.0	0.0720
14S-T6[12]	3.58	3.58	0.153	0.094	11.7	10,700	57.9	60.0	0.0723
14S-T6[12]	3.34	3.34	0.153	0.094	10.9	10,700	61.6	63.0	0.0752
14S-T6[12]	3.34	3.34	0.153	0.094	10.9	10,700	61.0	63.0	0.0744
14S-T6[12]	3.34	3.34	0.153	0.094	10.9	10,700	61.0	63.0	0.0744
61S-T6[13]	2.00	2.00	0.062	0	15.6	10,700	37.8	44.0	0.0552
61S-T6[13]	2.00	2.00	0.062	0	15.6	10,700	36.8	44.0	0.0537
61S-T6[13]	2.50	2.50	0.047	0	26.1	10,700	21.4	44.0	0.0312
Brass[14]	1.00	1.00	0.0065	0	77.0	16,400	11.2	31.4	0.0156
Brass[14]	1.00	1.00	0.0056	0	89.2	16,000	9.4	28.6	0.0139
Brass[14]	2.00	2.00	0.0065	0	154.0	16,400	6.3	31.4	0.0087
17S-T[15]	4.00	4.00	0.040	...	50.0	10,000	12.5	46.0	0.0185
17S-T[15]	3.00	3.00	0.040	...	37.5	10,000	16.1	46.0	0.0239
17S-T[15]	2.00	2.00	0.041	...	25.0	10,000	23.2	46.0	0.0342
17S-T[15]	1.00	1.00	0.040	...	12.5	10,000	45.6	46.0	0.0674
17S-T[15]	0.938	0.938	0.031	...	15.1	10,000	42.3	44.0	0.0643
17S-T[15]	0.813	0.813	0.016	...	25.4	10,000	22.2	44.0	0.0335
17S-T[15]	0.688	0.688	0.016	...	21.5	10,000	24.0	44.0	0.0362
17S-T[15]	0.563	0.563	0.016	...	17.6	10,000	32.2	44.0	0.0486
24S-T*	0.930	1.176	0.070	0.156	7.5	10,500	59.8	45.0	0.0870
24S-T*	0.934	1.176	0.070	0.156	7.5	10,500	59.3	45.0	0.0863
24S-T*	0.948	1.694	0.052	0.250	12.7	10,500	40.8	45.0	0.0594
24S-T*	0.948	1.696	0.052	0.250	12.7	10,500	40.8	45.0	0.0594
24S-T*	1.160	1.974	0.033	0.188	23.7	10,500	24.7	45.0	0.0360
24S-T*	1.160	1.974	0.033	0.188	23.7	10,500	24.8	45.0	0.0361
24S-T*	1.670	1.670	0.084	0.375	10.0	10,500	55.7	45.0	0.0810
24S-T*	1.670	1.670	0.084	0.375	10.0	10,500	54.4	45.0	0.0792
24S-T*	0.702	0.702	0.050	0.094	7.0	10,500	62.2	45.0	0.0905
24S-T*	0.702	0.702	0.050	0.094	7.0	10,500	62.4	45.0	0.0908
24S-T*	1.692	1.692	0.058	0.375	14.6	10,500	46.9	45.0	0.0682
24S-T*	1.692	1.692	0.058	0.375	14.6	10,500	46.8	45.0	0.0681

* Tests conducted by writer. Compression yield stress assumed equal to 45,000 lbs. per sq.in.

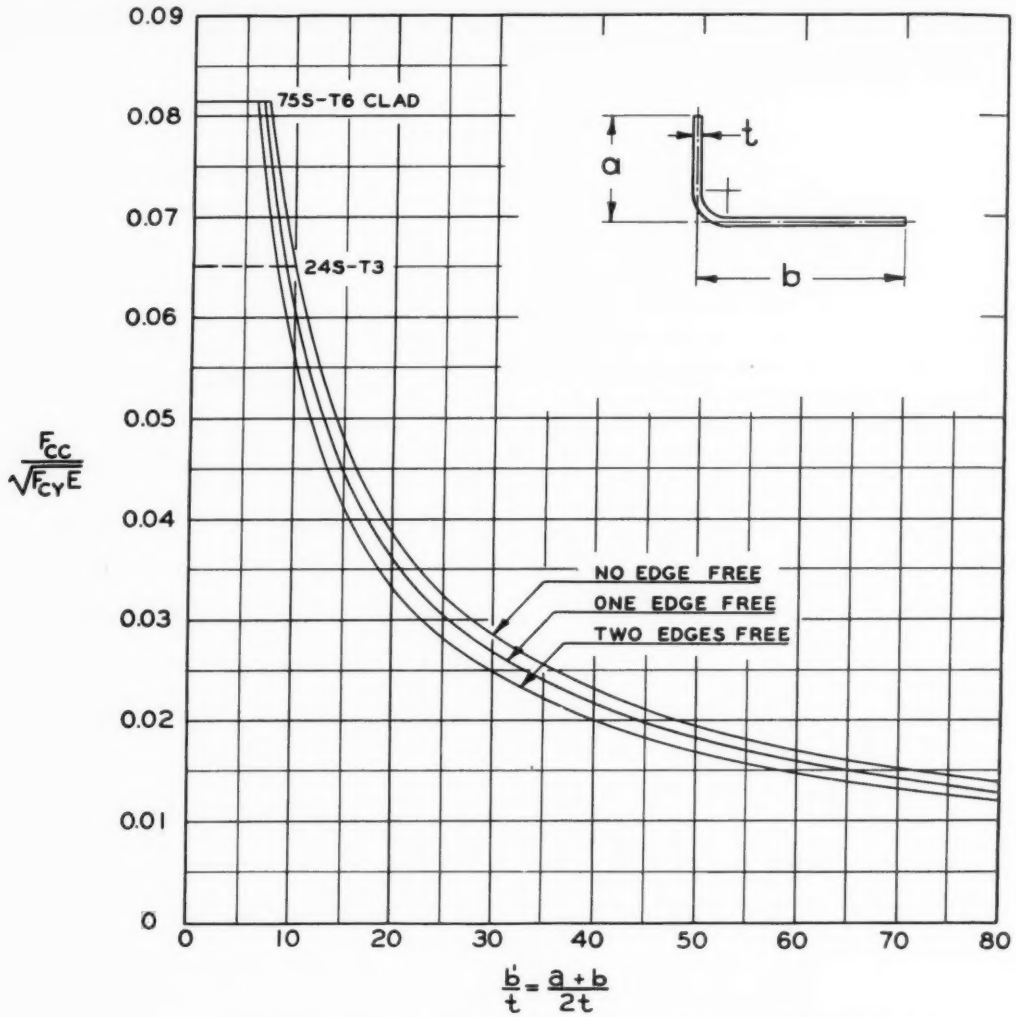

FIG. 9 – DIMENSIONLESS CRIPPLING STRESS vs. b/t

or, from Eq. (17),

$$\frac{P_{cc}}{t^2\sqrt{F_{cy}E}} = 2C_e\left[1 - 0.214\left(\frac{R/t}{b'/t}\right)\right](b'/t)^{0.25}$$

If the ratio of bend radius to thickness, R/t, is taken as three (standard aircraft practice),

$$\frac{P_{cc}}{t^2\sqrt{F_{cy}E}} = 2C_e\left(\frac{b'}{t}\right)^{0.25}\left[1 - \frac{0.642}{b'/t}\right] \qquad (18)$$

Eq. (18) is plotted in Fig. 10 for the three degrees of edge support. A dimensionless area curve (A/t^2 vs. b'/t) is also included in this plot.

Crippling of Formed Structural Shapes

In order to check the accuracy of the proposed method of crippling stress prediction, the 24 typical structural shapes of Table VI (Fig. 11) were fabricated from 24S-T3 clad sheet. The dimensions of the various shapes of Table VI are mid-line dimensions, and the inside bend radii in all cases were $^1/_8$ in. The specimens were fabricated with the grain direction coinciding with the direction of loading.

The testing technique employed in this series of tests was identical with the angle and channel tests of Figs. 2, 3, and 4. The tests were made in a Baldwin-Southwark testing machine having a maximum capacity of 60,000 lbs. and intermediate load ranges of 24,000 and 6,000 lbs.

The analysis technique employed by the writer is shown in Fig. 12. Dimensionless crippling loads were obtained from Fig. 10 and were converted to dimensional quantities using the average values of F_{cy} and E of Table IV. The calculated area of the section is $t^2\sum(A/t^2)$ or $(0.0255)^2(180.4) = 0.1173$ sq.in. The

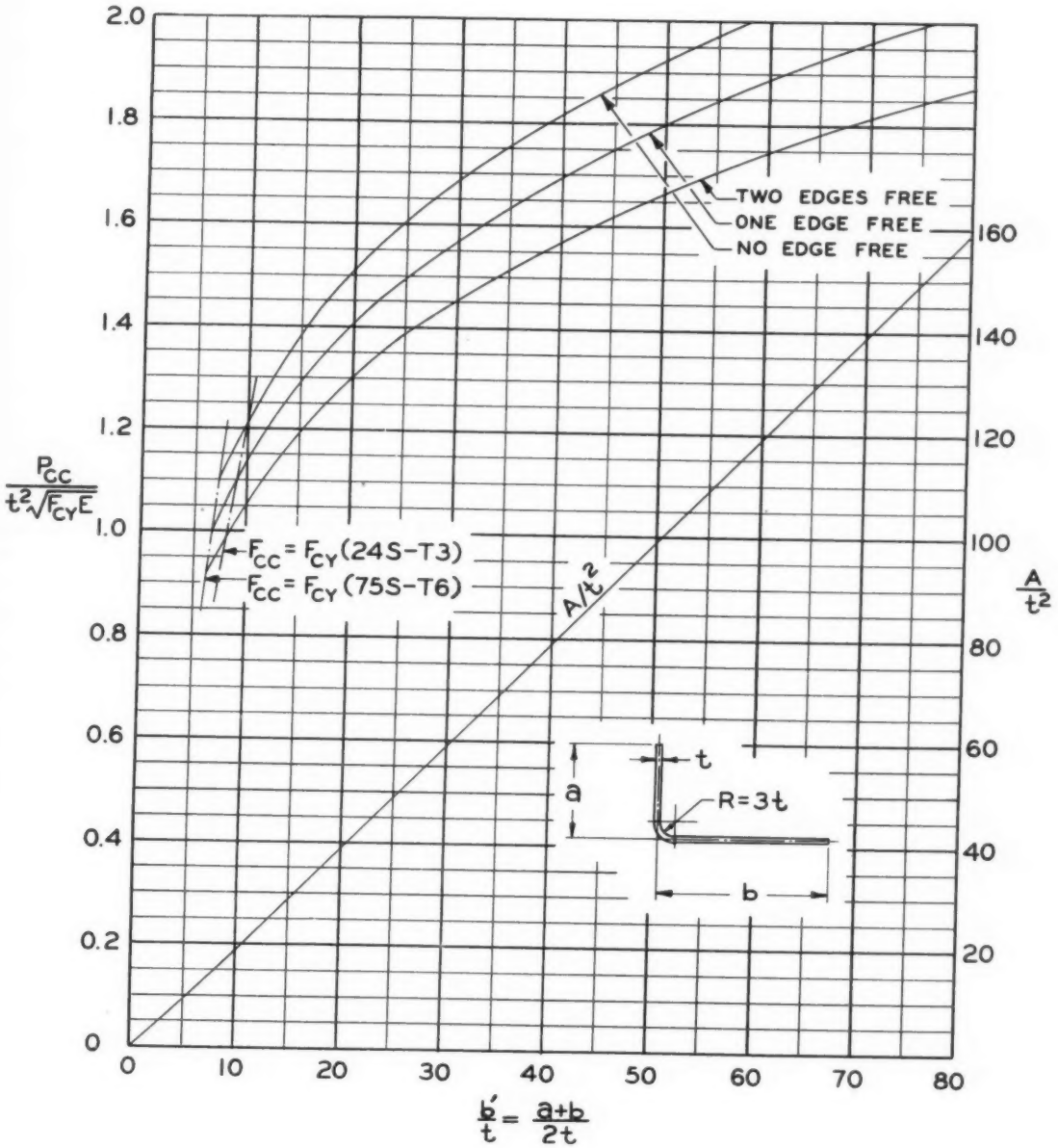

FIG. 10 – DIMENSIONLESS CRIPPLING LOAD vs. b'/t

TABLE VI
Results of Crippling Tests of 24S-T3 Clad Formed Structural Shapes

Shape	a	b	c	d	e	t	A	Test F_{cc}	Prediction F_{cc}
A1	1.000	0.434	...	...	...	0.0250	0.0672	26.2	25.0
A2	1.568	0.437	...	...	...	0.0315	0.1188	22.9	23.0
B1	1.205	1.340	1.236	0.447	...	0.0255	0.1833	20.8	22.3
B2	1.198	1.610	1.001	0.445	...	0.0320	0.2040	27.1	27.0
C1	2.457	0.980	0.449	...	...	0.0200	0.0989	17.3	16.6
C2	2.487	0.987	0.414	...	...	0.0315	0.1571	24.1	23.6
C3	2.412	0.892	0.408	...	...	0.0382	0.1892	27.5	28.3
C4	2.236	1.262	0.428	...	...	0.0505	0.2660	31.4	32.1
C5	1.813	0.862	0.425	...	...	0.0258	0.1045	24.0	24.4
D1	1.231	2.260	0.853	0.443	0.443	0.0203	0.0984	17.4	17.1
D2	1.255	2.195	0.875	0.429	0.429	0.0382	0.1870	28.2	27.8
D3	0.847	1.887	0.847	0.431	0.431	0.0258	0.1070	23.3	24.2
D4	1.244	1.950	1.244	0.423	0.423	0.0252	0.1261	19.0	20.0
D5	1.250	1.904	1.250	0.415	0.415	0.0383	0.1886	27.7	26.4
E1	1.991	0.653	0.961	...	...	0.0252	0.0868	15.8	15.1
E2	1.032	0.492	0.844	...	...	0.0253	0.0558	22.6	20.9
E3	2.141	0.418	1.028	...	...	0.0504	0.1715	24.7	25.4
E4	1.213	0.408	0.935	...	...	0.0255	0.0620	21.0	19.7
F1	2.331	0.856	1.241	0.424	0.424	0.0318	0.1571	23.9	23.0
F2	2.118	0.976	1.266	0.732	0.442	0.0318	0.1651	23.8	23.1
F3	1.788	0.443	0.953	0	0.438	0.0500	0.1680	35.0	34.8
G1	0.977	1.561	0.881	0.422	...	0.0318	0.1127	26.2	23.9
G2	0.936	2.457	0.863	0.425	...	0.0255	0.1141	17.8	17.4
H	3.668	1.528	0.393	0.943	...	0.0318	0.1933	25.0	24.9

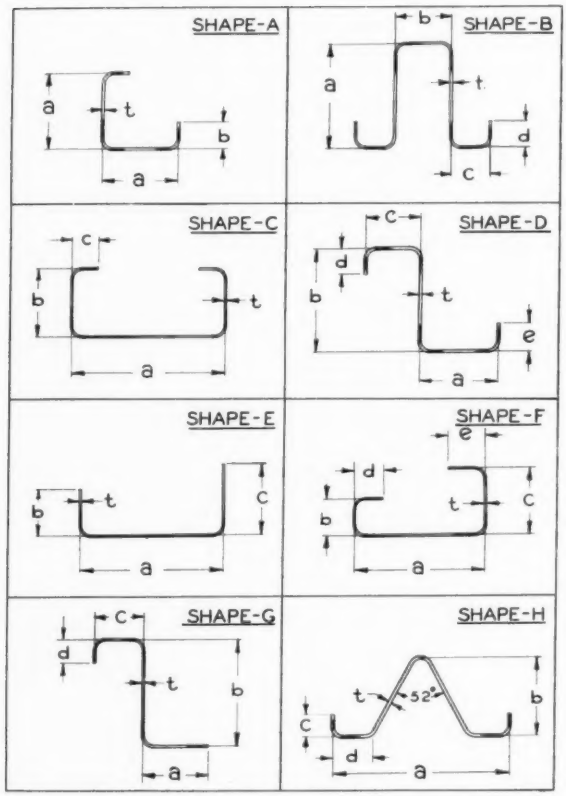

FIG. 11

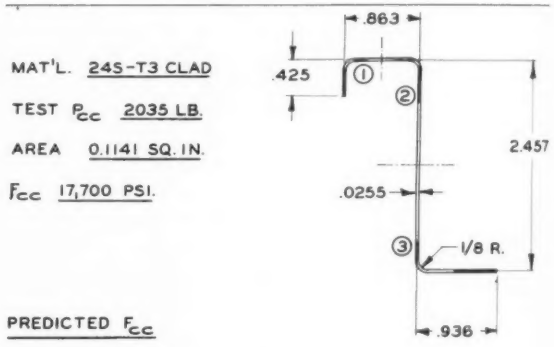

MAT'L. 24S-T3 CLAD

TEST P_{cc} 2035 LB.

AREA 0.1141 SQ. IN.

F_{cc} 17,700 PSI.

PREDICTED F_{cc}

ELEM.	$\frac{a+b}{2t}$	$\frac{P_{cc}}{t^2\sqrt{F_{cy}E}}$	$\frac{A}{t^2}$	EDGE COND.
1	16.8	1.332	32.5	O.E.F.
2	32.6	1.720	64.0	N.E.F.
3	42.5	1.720	83.9	O.E.F.
Σ	-	4.772	180.4	-

$$\frac{F_{cc}}{\sqrt{F_{cy}E}} = \frac{\Sigma(P_{cc}/t^2\sqrt{F_{cy}E})}{\Sigma(A/t^2)} = \frac{4.772}{180.4} = 0.0265$$

$$F_{cc} = 0.0265\sqrt{F_{cy}E} = (0.0265)(653{,}000) = \underline{17400 \text{ PSI}}$$

$$A = 180.4(.0255)^2 = 0.1173 \text{ SQ. IN.}$$

FIG. 12

measured area of the shape (obtained by weighing the specimen and using a material density of 0.100 lb. per cu.in.) was 0.1141. The disagreement of area values is due to the fact that the design chart was developed for sections having an R/t ratio of 3, whereas the test specimen R/t was 4.90. A comparison of test and predicted crippling tests is shown in the last two columns of Table VI. The ratio of predicted-to-test crippling stress for the 24 shapes tested shows a scatter between 0.912 and 1.121, while the average ratio is 0.993.

Predicting Crippling Stresses at Elevated Temperatures

Eq. (15) is in a form that is readily adaptable to predicting crippling stresses at elevated temperatures. All that is required is to have on hand curves giving the variation of F_{cy} and E with temperature.* While the physical significance of C_e in Eq. (15) is not known, an analysis of Schuette's equation [Eqs. (3) and (11)] indicates C_e to be a function of the effective modulus of elasticity and the compression yield stress, both of which vary with temperature. The present investigation demonstrates, however, that at room temperatures C_e is a constant for a given edge condition. Furthermore, an analysis by the author of the elevated temperature crippling tests of extruded H-sections conducted by Heimerl[18] indicates that Eq. (15) will yield reasonably accurate values of the crippling stress of these sections. Unfortunately, no test data on elevated temperature crippling of formed sheet-metal sections are known to the author; hence, the absolute certainty of the accuracy of Eq. (15) at elevated temperatures cannot yet be established.

Conclusions

From the results of this investigation the following conclusions on the proposed method of crippling stress prediction have been drawn:

(1) The crippling stress of equal and unequal angles, channels, zees, and rectangular tubes can be predicted directly from the equation

$$F_{cc} = C_e\sqrt{F_{cy}E}/(b'/t)^{0.75} \qquad (15)$$

where

F_{cy} = compression yield stress, lbs. per sq.in.
E = Young's modulus in compression, lbs. per sq.in.
b'/t = equivalent b/t of section = $(a + b)/2t$
C_e = coefficient that depends on the degree of edge support along the edges of contiguous angle elements. Specifically, these values are: 0.316 for angles with two edges free, 0.342 for angles with one edge free, and 0.366 for angles with no edge free

* This assumes that time effects are negligible—i.e., that creep buckling need not be considered.

(2) The crippling stress of structural shapes other than those mentioned above can be determined by dividing the shape into a series of angle sections and computing the crippling loads of the individual angles from Eq. (15) and the areas. The weighted crippling stress is obtained from

$$F_{cc} = \frac{\sum(\text{crippling loads of angles})}{\sum(\text{area of angles})}$$

(3) Although experimental evidence is lacking, the proposed crippling stress equation is believed to apply to the crippling of formed structural shapes at elevated temperatures, provided the variation of compression yield stress and Young's modulus with temperature is known.

References

[1] Stowell, E. Z., *A Unified Theory of the Plastic Buckling of Columns and Plates*, NACA TN No. 1556, April, 1948.

[2] Kroll, W. D., Fisher, G. P., and Heimerl, G. J., *Charts for Calculation of the Critical Stress for Local Instability of Columns with I-, Z-, Channel-, and Rectangular-Tube Sections*, NACA ARR No. 3K04, November, 1943.

[3] Heimerl, G. J., *Determination of Plate Compressive Strengths*, NACA TN No. 1480, December, 1948.

[4] Sechler, E. E., and Dunn, L. G., *Airplane Structural Analysis and Design;* John Wiley & Sons, Inc., New York, 1942.

[5] Crockett, H. B., *Predicting Stiffener and Stiffened Panel Crippling Stresses*, Journal of the Aeronautical Sciences, Vol. 9, No. 13, pp. 501–509, November, 1942.

[6] Schuette, E. H., *Observations of the Maximum Average Stress of Flat Plates Buckled in Edge Compression*, NACA TN No. 1625, February, 1949.

[7] Anon., *Crippling Strength of Magnesium Alloy Extrusions*, Tech. Memo. No. 15, The Dow Chemical Company, Magnesium Division, Midland, Mich.

[8] Heimerl, G. J., and Woods, W., *Effect of Brake Forming on the Strength of 24S-T Aluminum Alloy Sheet*, NACA TN No. 1072, May, 1946.

[9] Lundquist, E. E., Schuette, E. H., Heimerl, G. J., and Roy, J. A., *Column and Plate Compressive Strengths of Aircraft Structural Materials, 24S-T Aluminum Alloy Sheet*, NACA ARR L5F01, June, 1945.

[10] von Kármán, Th., Sechler, E. E., and Donnell, L. H., *The Strength of Thin Plates in Compression*, ASME Trans., APM-54-5, Vol. 54, No. 2, June 30, 1932.

[11] Marguerre, K., *The Apparent Width of the Plate in Compression*, NACA TM No. 833, July, 1937.

[12] Heimerl, G. J., and Pride, R. A., *Plastic Buckling of Simply Supported Compressed Plates*, NACA TN No. 1817, April, 1949.

[13] Bijlaard, P. P., and Fisher, G. P., *Interaction of Column and Local Buckling in Compression Members*, NACA TN No. 2640, March, 1952.

[14] Timoshenko, S., *Theory of Elastic Stability*, 1st Ed., p. 398; McGraw-Hill Book Company, Inc., New York, 1936.

[15] Anon., A.C.I.C. Information Circular No. 713, May, 1939.

[16] Gallaher, G. L., *Plate Compressive Strength of FS-1h Magnesium Alloy Sheet and a Maximum Strength Formula for Magnesium-Alloy and Aluminum-Alloy Formed Sections*, NACA TN No. 1714, October, 1948.

[17] Shanley, F. R., *Inelastic Column Theory*, Journal of the Aeronautical Sciences, Vol. 14, No. 5, p. 261, May, 1947.

[18] Heimerl G. J., and Roberts, W. M., *Determination of Plate Compressive Strengths at Elevated Temperatures*, NACA TN No. 1806, February, 1949.

Linearized Theory of the Oscillating Airfoil in Compressible Subsonic Flow*

R. TIMMAN†

Technological University, Delft, Holland

SUMMARY

Extending previous work, a series expression in Mathieu functions is given for the pressure distribution on an oscillating airfoil in two-dimensional subsonic flow. Using an identity between different solutions of the corresponding boundary value problem, it is shown that the resulting formula satisfies the reciprocity relations in nonstationary flow.

NOTATION

x	= coordinate in direction of main flow, fixed to the fluid
x'	= coordinate in direction of main flow, fixed to the airfoil
t	= time
X, Y, T	= coordinates obtained from x, y, t by a Lorentz transform
V	= flight velocity
c	= sound velocity
M	= V/c, Mach Number
β	= $(1 - M^2)^{1/2}$, Lorentz (Prandtl) factor
Φ	= velocity potential
φ	= acceleration potential
$\nu/2\pi$	= frequency of airfoil oscillations
$2l$	= airfoil chord
ω	= $\nu l/V$, nondimensional frequency parameter
Ω	= $\beta^2\omega$, compressible frequency parameter
$G(X, Y; X_1, Y_1)$	= Green's function of the second kind
$se_n(\eta)$	= odd Mathieu function of order n
$Ne_n^{(2)}(\xi)$	= associated Mathieu function of the third kind of order n
$w(x')$	= given normal velocity on the airfoil contour
p	= pressure
ρ	= density
Π	= pressure difference on the airfoil

(1) INTRODUCTION

IN HIS THESIS,[1] the author gave a solution to the problem of the determination of the pressure distribution on an oscillating airfoil in compressible subsonic flow. This solution was presented afterwards in corrected form by the author and van de Vooren,[2] together with an extension to the case of an oscillating airfoil with flap. The resulting formulas were evaluated numerically by the Computation Department of The Mathematical Centre at Amsterdam under the direction of Van Wijngaarden,[3] and the results were published in this JOURNAL.[4] The numerical values were not in good agreement with the values obtained by Dietze by a numerical method for the solution of Possio's integral equation.[5] A short time after publication in this JOURNAL, Fettis[6] raised severe objections to the values given in reference 4, because they did not satisfy the reciprocity relations for nonstationary flow, relations that at the time of publication were unknown to the authors.

Two possibilities were open: either an analytical error in the final formulas given in reference 4, or an error in the numerical evaluation by The Mathematical Centre.

In this paper it will be shown that the formula for the pressure distribution, as given in reference 4, satisfies identically the reciprocity relations in the form given by Flax.[7] This result was obtained by a re-examination of the theory inspired by the work of Hofsommer[8] in incompressible flow, which led to the establishment of a new identity which enabled the author to show that his pressure distribution satisfied the reciprocity relation. Moreover, using this identity, it was possible to simplify the expression for the pressure distribution considerably, thus getting a complete counterpart to the well-known results in incompressible flow. The author was informed by private communication that Kässner had already obtained similar results.

During the preparation of this paper the numerical error has also been detected, and the author has been informed, that the corrected numerical values in a particular case do check the reciprocity relations up to four decimal places. The author is indebted to Drs. van de Vooren and Van Spiegel of the N.L.L. for many interesting discussions on this subject.

(2) BASIC EQUATIONS

In a compressible medium the velocity potential $\Phi^0(x, y, t)$ and the acceleration potential $\varphi^0(x, y, t)$ of an unsteady two-dimensional disturbance satisfy the linearized wave equation

$$\varphi^0{}_{xx} + \varphi^0{}_{yy} - (1/c^2)\,\varphi^0{}_{tt} = 0 \qquad (1)$$

where x, y are cartesian coordinates fixed with respect to the fluid.

The relation between the two potentials is given by

$$\varphi^0(x, y, t) = \Phi^0{}_t(x, y, t) \qquad (2)$$

Received August 17, 1953.

* This research was sponsored by the N.I.V. (Netherlands Aircraft Development Board).

† Professor of Mathematics. Also, Consultant for Theoretical Aerodynamics, National Luchtvaart Laboratorium, Amsterdam.

We now consider a thin airfoil moving with subsonic velocity V, Mach Number M, in the direction of the negative x-axis. The equation for the potentials φ^0 and Φ^0 with respect to a set of coordinates fixed to the airfoil will be obtained from Eq. (1) by the transformation (Galilei Transformation)

$$x' = x + Vt, \quad y' = y, \quad t' = t \tag{3}$$

It is, however, well known that the wave equation, Eq. (1), is invariant for Lorentz transformations of the form

$$X = \beta(x + VT), \quad Y = y, \quad T = \beta[t + (M/c)x] \tag{4}$$

where

$$\beta = (1 - M^2)^{-1/2} \tag{5}$$

The relation between the Galilei coordinates, Eq. (3), and the Lorentz coordinates, Eq. (4), then reads

$$X = \beta x', \quad Y = y', \quad T = (t'/\beta) + (\beta M x'/c) \tag{6}$$

We now consider harmonic oscillations of the airfoil with frequency ν, and hence we may introduce Lorentz disturbance potentials $\Phi(X, Y)$ and $\varphi(X, Y)$ by

$$\Phi^0(x, y, t) = \Phi(X, Y)e^{i\nu\beta T} = \Phi(X, Y)e^{i\nu\beta MX/c} \cdot e^{i\nu t} \tag{7}$$

$$\varphi^0(x, y, t) = \varphi(X, Y)e^{i\nu\beta T} = \varphi(X, Y)e^{i\nu\beta MX/c} \cdot e^{i\nu t} \tag{8}$$

Then $\Phi(X, Y)$ and $\varphi(X, Y)$ satisfy the equation

$$\varphi_{XX} + \varphi_{YY} + k^2\varphi = 0 \tag{9}$$

where

$$k = \beta\nu/c$$

The relation (2) between the potentials transforms into

$$\varphi(X, Y) = i\nu\beta^2\Phi(X, Y) + \beta V\Phi_X(X, Y) \tag{10}$$

We assume the airfoil to extend over the segment $-l \leq x' \leq +l$ of the x'-axis, or in the Lorentz coordinates over the segment

$$-\beta l \leq X \leq +\beta l$$

The boundary conditions for the potentials are given by the oscillatory motion, which is assumed to be known. For an infinitely thin airfoil, the normal velocity is equal at opposite points on the upper and lower side, and we get the boundary condition for the velocity potential

$$\Phi_y^0(x', +0) = \Phi_y^0(x', -0) = w(x') \cdot e^{i\nu t}, \qquad -l \leq x' \leq +l \tag{11}$$

where $w(x')$ is the amplitude of the given velocity. This imposes on our problem the symmetry condition,

$$\Phi^0(x', y, t) = -\Phi^0(x', -y, t)$$

Similarly, we get a boundary condition for $\varphi(x', y, t)$ by considering the normal values of the acceleration

$$\partial_t w(x')e^{i\nu t} = \partial_t w(x + Vt)e^{i\nu t} = (i\nu w + Vw_{x'})e^{i\nu t}$$

which gives

$$\varphi_y(x', +0, t) = \varphi_y(x', -0, t) = (i\nu w + Vw_{x'})e^{i\nu t} \tag{12}$$

These boundary conditions are readily transformed into boundary conditions for the Lorentz potentials,

$$\Phi_Y(X, 0) = w(x')e^{-i\nu\beta MX/c} = W(X) \tag{13}$$

$$\varphi_Y(X, 0) = (i\nu w + Vw_{x'})e^{-i\nu\beta MX/c} = i\nu\beta^2 W(X) + \beta V W_X \tag{14}$$

By giving the boundary conditions on a closed contour, solutions of the wave equation are not uniquely determined in the outer region. Here Sommerfeld's condition must be added, which states that, at infinity, the solution must represent traveling waves, diverging from the airfoil. For a closed regular contour, the solution is uniquely determined by these conditions. The behavior of the solutions near the ends of the segment will be investigated separately.

(3) The Solution of the Boundary Value Problem

Considering the two sides of the airfoil together as forming a closed contour, the problem is a boundary value problem of the second kind for the wave equation, and its solution depends on Green's function of the second kind.

This function, denoted by $G(X, Y; X_1, Y_1)$ is defined as a solution of the equation

$$\Delta\varphi + k^2\varphi = 0 \tag{1}$$

satisfying the following conditions:

(i) At $-\beta l \leq X \leq +\beta l$,

$$G_Y(X, +0; X_1, Y_1) = G_Y(X, -0; X_1, Y_1) = 0$$

(ii) At $X = X_1$, $Y = Y_1$, the function must have a logarithmic singularity.

(iii) At infinity, the function must satisfy the Sommerfeld condition for outgoing waves.

In physical language the function represents the potential of a source in the point X_1, Y_1 with the segment $-\beta l \leq X \leq \beta l$ as a fixed wall.

Unfortunately it has never been possible to obtain an explicit expression for this function. For this reason we follow another procedure for the solution of the boundary value problem, which then will give us an expression for the function G.

We introduce elliptic coordinates

$$X = \beta l \cosh\xi \cos\eta, \quad \xi \geq 0$$
$$Y = \beta l \sinh\xi \sin\eta, \quad -\pi < \eta \leq +\pi$$

The derivatives then transform by

$$\beta l\partial_X = \frac{\sinh\xi\cos\eta\partial_\xi - \cosh\xi\sin\eta\partial_\eta}{\cosh^2\xi - \cos^2\eta}$$

$$\beta l\partial_Y = \frac{\cosh\xi\sin\eta\partial_\xi + \sinh\xi\cos\eta\partial_\eta}{\cosh^2\xi - \cos^2\eta}$$

and the wave equation then passes into

$$\varphi_{\xi\xi} + \varphi_{\eta\eta} + 2h^2(\cosh 2\xi - \cos 2\eta)\varphi = 0 \qquad (2)$$

where

$$h = \beta kl/2 = \beta^2 \nu l/c$$

Particular solutions of this equation having the proper symmetry can then be found by separation of variables, which gives solutions of the type[9]

$$Ne_n^{(2)}(\xi)se_n(\eta)$$

where $se_n(\eta)$ is the odd Mathieu function of order n and $Ne_n^{(2)}(\xi)$ is the corresponding associated Mathieu function such that the particular solution satisfies Sommerfeld's condition.

We now assume a series solution of the form

$$\sum_{n=1}^{\infty} \alpha_n Ne_n^{(2)}(\xi)se_n(\eta)$$

In order to determine the coefficients α_n we write down the boundary condition in elliptic coordinates at $\xi = 0$

$$\varphi_\xi = \sin\eta\cdot f(\eta) \qquad (3)$$

If $f(\eta)$ is assumed to be a continuously differentiable, even function of η, $f(\eta)\cdot\sin\eta$ can be expanded in a uniformly convergent series of odd Mathieu functions

$$\sin\eta\cdot f(\eta) = \sum_{n=1}^{\infty} Q_n se_n(\eta) \qquad (4)$$

where

$$Q_n = \frac{2}{\pi}\int_0^\pi f(\eta_1)\sin\eta_1 se_n(\eta_1)\,d\eta_1 \qquad (5)$$

Differentiating our series solution and putting $\xi = 0$, we obtain

$$\varphi_\xi(0,\eta) = \sum_{n=1}^{\infty} \alpha_n\cdot Ne_n^{(2)\prime}(0)\cdot se_n(\eta) \qquad (6)$$

and equating corresponding coefficients in Eqs. (4) and (6), we get the solution

$$\varphi(\xi,\eta) = \sum_{n=1}^{\infty} Q_n\cdot\frac{Ne_n^{(2)}(\xi)}{Ne_n^{(2)\prime}(0)}\cdot se_n(\eta) = \sum_{n=1}^{\infty}\frac{Ne_n^{(2)}(\xi)}{Ne_n^{(2)\prime}(0)}\cdot se_n(\eta)\cdot\frac{2}{\pi}\int_0^\pi f(\eta_1)\sin\eta_1\cdot se_n(\eta_1)\,d\eta_1 \qquad (7)$$

For large values of n it can be shown (see reference 2, Appendix 2) that the terms in this series are approximated by the corresponding terms of the ordinary Fourier expansion in the incompressible case and hence the convergence properties in the two cases are the same.

This latter expression is

$$\varphi^i(\xi,\eta) = \sum_{n=1}^{\infty}\frac{e^{-n\xi}}{n}\sin n\eta\cdot\frac{2}{\pi}\int_0^\pi f(\eta_1)\sin\eta_1\, n\eta_1\,d\eta_1 \qquad (8)$$

and it is well known that in this case summation and integration may be interchanged. This can also be done in our case, and we write down

$$\varphi(\xi,\eta) = \int_0^\pi f(\eta_1)\cdot\sin\eta_1\cdot G(\xi,\eta;\eta_1)\,d\eta_1 \qquad (9)$$

where

$$G(\xi,\eta;\eta_1) = \frac{2}{\pi}\sum_{n=1}^{\infty}\frac{Ne_n^{(2)}(\xi)}{Ne_n^{(2)\prime}(0)}se_n(\eta)se_n(\eta_1) \qquad (10)$$

This series vanishes at the end points of the interval—viz., at $\xi = 0$, $\eta = 0$ and $\xi = 0$, $\eta = \pi$.

In the incompressible case, the series can be summed

$$G^i(\xi,\eta;\eta_1) = \frac{2}{\pi}\sum_{n=1}^{\infty}\frac{e^{-n\xi}}{n}\sin n\eta\cdot\sin n\eta_1 = \frac{1}{2\pi}\ln\frac{\cosh\xi - \cos(\eta+\eta_1)}{\cosh\xi - \cos(\eta-\eta_1)} \qquad (11)$$

For the velocity potential the function $f(\eta)$ is equal to $\beta lW(\eta)$ and the corresponding solution is

$$\Phi(\xi,\eta) = \beta l\int_0^\pi W(\eta_1)\sin\eta_1\cdot G(\xi,\eta;\eta_1)\,d\eta_1 \qquad (12)$$

and for the acceleration potential

$$f(\eta) = \beta l[i\nu\beta^2 W - (V/l\sin\eta)\,W_\eta]$$

and, hence,

$$\varphi(\xi,\eta) = \beta V\int_0^\pi (i\Omega W\sin\eta_1 - W_{\eta_1})G(\xi,\eta;\eta_1)\,d\eta_1 \qquad (13)$$

where

$$\Omega = \beta^2\nu l/V$$

(4) The Fundamental Identity

The two solutions to the same problem obtained in the preceding section are not identical. This is apparent if we calculate the acceleration potential $\varphi^*(X, Y)$ corresponding to the velocity potential, Section (3), Eq. (12) by

means of

$$\varphi^*(X, Y) = (V/l)\,(i\Omega\Phi + \beta l\Phi_X) \tag{1}$$

which, on the airfoil, where $\xi = 0$ becomes

$$\varphi^*(0, \eta) = (V/l)\,[i\Omega\Phi(0, \eta) - (1/\sin\eta)\cdot\Phi_\eta(0, \eta)] \tag{2}$$

Apparently this expression is infinite at the end points $\eta = 0$ and $\eta = \pi$, but Section (3), Eq. (13) vanishes at these points.

The difference potential must have a zero normal derivative on the airfoil, it must be regular in all internal points and singular at the end points, and the kind of the singularity must be the same as that of $\varphi^*(\xi, \eta)$. Now the function $G(\xi, \eta; \eta_1)$ given by Section (3), Eq. (10) has these properties, except for the singular behavior. As the singularity corresponds to a differentiation, we differentiate with respect to η_1. Then $G_{\eta_1}(\xi, \eta; \eta_1)$ is still a solution of the wave equation in ξ and η, and we may put either $\eta_1 = 0$ or $\eta_1 = \pi$. We now show that

$$\varphi(\xi, \eta) = \varphi^*(\xi, \eta) + \beta V\lambda_1 G_{\eta_1}(\xi, \eta; 0) + \beta V\lambda_2 G_{\eta_1}(\xi, \eta; \pi) \tag{3}$$

with suitable coefficients λ_1 and λ_2. These coefficients are determined by the condition, that the right-hand side of Eq. (3) must remain finite at $\eta = 0$ and $\eta = \pi$, or that

$$\lim_{\eta\to 0}\,[-(V/l)\Phi_\eta(0, \eta) + \beta V\lambda_1 \sin\eta\cdot G_{\eta_1}(0, \eta; 0) + \beta V\lambda_2 \sin\eta\cdot G_{\eta_1}(0, \eta; \pi)] = 0 \tag{4}$$

$$\lim_{\eta\to \pi}\,[-(V/l)\Phi_\eta(0, \eta) + \beta V\lambda_1 \sin\eta\cdot G_{\eta_1}(0, \eta; 0) + \beta V\lambda_2 \sin\eta\cdot G_{\eta_1}(0, \eta; \pi)] = 0 \tag{5}$$

In order to evaluate these limits we remark that in the neighborhood of a singular point the solutions of the wave equation can be approximated by the corresponding solutions of the potential equation and hence, up to a function, vanishing in the limit

$$G_{\eta_1}(0, \eta; 0) \sim G_{\eta_1}{}^{i}(0, \eta; 0) = \sin\eta/\pi\,(1 - \cos\eta)$$

$$G_{\eta_1}(0, \eta; \pi) \sim G_{\eta_1}{}^{i}(0, \eta; \pi) = -\sin\eta/\pi\,(1 + \cos\eta)$$

Hence we find, calculating the limits in Eqs. (4) and (5),

$$\lambda_1 = \frac{\pi}{2}\int_0^\pi W(\eta_1)\sin\eta_1\cdot G_\eta(0, 0; \eta_1)\,d\eta_1 \tag{6}$$

$$\lambda_2 = -\frac{\pi}{2}\int_0^\pi W(\eta_1)\sin\eta_1\cdot G_\eta(0, \pi; \eta_1)\,d\eta_1 \tag{7}$$

The remaining difference function now is finite at the end points; its derivative vanishes on the airfoil and, hence, it is identically zero. Thus we have found the important identity,

$$\beta l\,\partial_X\int_0^\pi W(\eta_1)\sin\eta_1\cdot G(\xi, \eta; \eta_1)\,d\eta_1 + \int_0^\pi W_{\eta_1}(\eta_1)\cdot G(\xi, \eta; \eta_1)\,d\eta_1 + \lambda_1\cdot G_{\eta_1}(\xi, \eta; 0) + \lambda_2 G_{\eta_1}(\xi, \eta; \pi) = 0 \tag{8}$$

(5) The Kutta Condition

Neither of the two solutions given in the preceding section gives the solution to the actual problem of airfoil theory. The regular solution $\varphi(X, Y)$ for the acceleration potential was obtained from the boundary values of the normal acceleration, which were found by differentiating the given values of the normal velocity, and it cannot be expected that integration again yields back the proper velocity.

On the other hand, the velocity potential $\Phi(X, Y)$ adapted to the given values of the normal velocity gave a pressure distribution (acceleration potential) infinite both at the leading and trailing edge, which is contrary to the Kutta condition, applying in the actual problem, which requires that the pressure vanishes at the trailing edge. (Actually the Kutta condition only requires that the pressure remains finite at the trailing edge, but it can be shown that in this case the acceleration potential must vanish.)

As we already remarked, $\varphi(\xi, \eta)$ vanishes both at the leading and trailing edge and also $G_{\eta_1}(\xi, \eta; \pi)$ vanishes at the trailing edge $\xi = 0$, $\eta = 0$ and does not contribute to the normal acceleration. Hence, we assume for the acceleration potential,

$$\varphi(\xi, \eta) = \beta V\left[\int_0^\pi \{i\Omega W\sin\eta_1 - W_{\eta_1}\}\cdot G(\xi, \eta; \eta_1)\,d\eta_1 + a_0 G_{\eta_1}(\xi, \eta; \pi)\right] \tag{1}$$

where a_0 must be determined by the condition, that the normal velocity, obtained from Eq. (1), must coincide with the given normal velocity. As the normal accelerations do already coincide, it is sufficient to consider a single point of the airfoil and, following our previous choice, we take the leading edge.

The derivatives Φ_Y and φ_Y being related by the same formula as Φ and φ—viz.,

$$\varphi_Y(X,\ Y) = V/l\ (i\Omega\Phi_Y + \beta l\Phi_{XY}) \tag{2}$$

Φ_Y can be expressed into φ_Y by integrating this first-order differential equation,

$$\Phi_Y(X,\ Y) = \frac{1}{\beta V}\int_{-\infty}^{X} \exp\left[-\frac{i\Omega(X - X')}{\beta l}\right]\cdot\varphi_Y(X',\ Y)\,dX' \tag{3}$$

if we assume that $\Phi_Y = 0$ at $X = -\infty$.

Substituting, we get the following equation for the determination of a_0:

$$W(\pi) = \int_{-\infty}^{-\beta l} e^{i\Omega[1+(X'/\beta l)]}\,dX'\cdot\left[\partial_Y\int_0^{\pi}(i\Omega W\sin\eta_1 - W_{\eta_1})\cdot G(\xi',\ \eta';\ \eta_1)\,d\eta_1\right]_{Y=0} + a_0\int_{-\infty}^{-\beta l} e^{i\Omega[1+(X'/\beta l)]}\,[\partial_Y G_{\eta_1}(\xi',\ \eta';\ \pi)]_{Y=0}\,dX' \tag{4}$$

Here the integration extends along the X-axis from $-\infty$ to $-\beta l$ and, substituting $\eta = \pi$,

$$X' = -\beta l\cosh\xi', \qquad \partial_Y = (-1/\beta l\sinh\xi')\partial_\eta$$

we get

$$W(\pi) = -e^{i\Omega}\int_0^{\infty} e^{-i\Omega\cosh\xi'}\,d\xi'\cdot\int_0^{\pi}(i\Omega W\sin\eta_1 - W_{\eta_1})\,G_\eta\,(\xi',\ \pi;\ \eta_1)\,d\eta_1 - a_0e^{i\Omega}\int_0^{\infty} e^{-i\Omega\cosh\xi'}\,G_{\eta\eta_1}\,(\xi',\ \pi;\ \pi)\,d\xi' \tag{5}$$

which is the same as Eq. (7.25) of our previous paper.[2]

By means of the fundamental identity, the equation can be considerably simplified. Substituting

$$\int_0^{\pi} W_{\eta_1}\cdot G(\xi',\ \eta';\ \eta_1)\,d\eta_1 = -\beta l\partial_{X'}\int_0^{\pi} W\sin\eta_1\cdot G(\xi',\ \eta';\ \eta_1)\,d\eta_1 - \lambda_1 G_{\eta_1}(\xi',\ \eta';\ 0) - \lambda_2 G_{\eta_1}(\xi,\ \eta;\ \pi)$$

into Eq. (4), we get

$$W(\pi) = \beta l e^{i\Omega}\int_{-\infty}^{-\beta l} e^{i\Omega X'/\beta l}\,dX'\cdot\left[\partial_Y\partial_{X'}\int_0^{\pi} W\sin\eta_1\cdot G(\xi',\ \eta';\ \eta_1)\,d\eta_1\right]_{Y=0} + \lambda_1 e^{i\Omega}\int_{-\infty}^{-\beta l} e^{i\Omega X'/\beta l}\,[\partial_Y G_{\eta_1}\,(\xi',\ \eta';\ 0)\,]_{Y=0}\,dX' + (\lambda_2 + a_0)\cdot e^{i\Omega}\int_{-\infty}^{-\beta l} e^{i\Omega X'/\beta l}[\partial_Y G_{\eta_1}(\xi',\ \eta';\ \pi)\,]_{Y=0}\ dX' + i\Omega e^{i\Omega}\int_{-\infty}^{-\beta l} e^{i\Omega X'/\beta l}\left[\partial_Y\int_0^{\pi} W\sin\eta_1\cdot G(\xi',\ \eta';\ \eta_1)\right]_{Y=0} dX' \tag{6}$$

and by partial integration of the first term,

$$W(\pi) = \beta l\partial_Y\int_0^{\pi} W\sin\eta_1\cdot G(0,\ \pi;\ \eta_1)\,d\eta_1 - i\Omega e^{i\Omega}\int_{-\infty}^{-\beta l} e^{i\Omega X'/\beta l}\,dX'\left[\partial_Y\int_0^{\pi} W\sin\eta_1\cdot G(\xi',\ \eta';\ \eta_1)\,d\eta_1\right]_{Y=0} + \lambda_1 e^{i\Omega}\int_{-\infty}^{-\beta l} e^{i\Omega X'/\beta l}[\partial_Y G_{\eta_1}(\xi',\ \eta';\ 0)\,]_{Y=0}\,dX' + (\lambda_2 + a_0)e^{i\Omega}\int_{-\infty}^{-\beta l} e^{i\Omega X'/\beta l}\,[\partial_Y G_{\eta_1}(\xi',\ \eta';\ \pi)\,]_{Y=0}\,dX' \tag{7}$$

Regarding Section (3), Eq. (12), we see that the first term of the right-hand side is equal to $W(\pi)$. Introducing the integrals

$$\left.\begin{aligned} R_1 &= -\int_{-\infty}^{-\beta l} e^{i\Omega X'/\beta l}\,[\partial_Y G_{\eta_1}(\xi',\ \eta';\ 0)\,]_{Y=0}\,dX' = \int_0^{\infty} e^{-i\Omega\cosh\xi'}\,G_{\eta\eta_1}\,(\xi',\ \pi;\ 0)\,d\xi' \\ R_2 &= -\int_{-\infty}^{-\beta l} e^{i\Omega X'/\beta l}\,[\partial_Y G_{\eta_1}(\xi',\ \eta';\ \pi)\,]_{Y=0} dX' = \int_0^{\infty} e^{-i\Omega\cosh\xi'}\,G_{\eta\eta_1}(\xi',\ \pi;\ \pi)\,d\xi' \end{aligned}\right\} \tag{8}$$

We find

$$a_0 = -\lambda_2 - (\lambda_1 R_1/R_2) \tag{9}$$

Putting

$$T(\Omega) = R_1/R_2$$

we finally obtain, for the Lorentz acceleration potential, the expression

$$\varphi(\xi, \eta) = \beta V\left[\int_0^{\pi} (i\Omega W \sin \eta_1 - W_{\eta_1})\cdot G(\xi, \eta; \eta_1)\, d\eta_1 - (\lambda_2 + \lambda_1 T)\cdot G_{\eta_1}(\xi, \eta; \pi)\right] \tag{10}$$

It should be remarked here that R_1 and R_2 cannot be calculated directly by termwise integrating the series expression for $G_{\eta\eta_1}$ but must be calculated as described for R_1 in,[2] by splitting off the "incompressible" singular part of $G_{\eta\eta_1}$ and integrating termwise the remaining correcting series that is uniformly convergent. The value of the contribution of the singular part can be taken from the known result in the incompressible case. From the Lorentz acceleration potential, we now calculate the physical acceleration potential, related to the pressure difference by the formula

$$\Pi(x')\cdot e^{i\nu t} = p^+(x', 0, t) - p^-(x', 0, t) = 2\rho\varphi\ (x', 0, t) \tag{11}$$

This gives

$$\Pi(x') = 2\rho\cdot e^{i\nu\beta^2 Mx'/c}\cdot\varphi(0, \eta) = 2\rho\beta V\cdot e^{i\Omega M^2\cos\eta}\left[\int_0^{\pi} (i\Omega W \sin\eta_1 - W_{\eta_1})G(0, \eta; \eta_1)\, d\eta_1 - (\lambda_2 + \lambda_1 T)G_{\eta_1}(0, \eta; \pi)\right]$$

$$= 2\rho\beta V\cdot e^{i\Omega M^2\cos\eta}\left[\int_0^{\pi} e^{-i\Omega M^2\cos\eta_1}\,(i\omega w \sin\eta_1 - w_{\eta_1})G(0, \eta; \eta_1)\, d\eta_1 - (\lambda_2 + \lambda_1 T)G_{\eta_1}(0, \eta; \pi)\right]. \tag{12}$$

where $\omega = \nu l/V$.

(6) The Reciprocity Relation

We now prove the reciprocity relation in the form given by Flax[7] and show that the expression in Section (5), Eq. (10) satisfies this identity.

Consider two solutions of the wave equation φ and Φ, both antisymmetric in Y and vanishing in infinity. Green's theorem enables us to write

$$\int_{-\infty}^{+\infty} \varphi(X', 0)\cdot\bar{\Phi}_Y(X', 0)\, dX' = \int_{-\infty}^{+\infty} \bar{\Phi}(X', 0)\cdot\varphi_Y(X', 0)\, dX' \tag{1}$$

Considering now φ as the Lorentz acceleration potential corresponding to an airfoil moving in the direction of the negative x-axis, the corresponding Lorentz velocity potential satisfies

$$\varphi(X, Y) = i\nu\beta^2\Phi(X, Y) + \beta V\,\Phi_X(X, Y)$$

The second member of Eq. (1) now can be written as

$$i\nu\beta^2\int_{-\infty}^{+\infty}\bar{\Phi}\Phi_Y\, dX + \beta V\int_{-\infty}^{+\infty}\bar{\Phi}\Phi_{X'Y}\, dX'$$

By partial integration of the second term we get

$$\beta V\left[\bar{\Phi}\Phi_Y\right]_{-\infty}^{+\infty} - \beta V\int_{-\infty}^{+\infty}\Phi_Y\bar{\Phi}_{X'}\cdot dX'$$

If we consider $\bar{\Phi}$ as the Lorentz velocity potential of an airfoil moving with velocity V in the direction of the positive X-axis, the corresponding acceleration potential is

$$\bar{\varphi} = i\nu\beta^2\bar{\Phi} - \beta V\bar{\Phi}_X \tag{2}$$

Moreover, at $-\infty$, $\Phi_Y = 0$ and at $+\infty$, $\bar{\Phi} = 0$, and the integrated parts vanish. This gives the result

$$\int_{-\infty}^{+\infty}\varphi\cdot\bar{\Phi}_Y\, dX' = \int_{-\infty}^{+\infty}\bar{\varphi}\cdot\Phi_Y\, dX' \tag{3}$$

Considering further that in the regions of the x-axis before and behind the airfoil both φ and $\bar{\varphi}$ vanish, we may write

$$\int_{-\beta l}^{+\beta l}\varphi\cdot\bar{\Phi}_Y\, dX' = \int_{-\beta l}^{+\beta l}\bar{\varphi}\cdot\Phi_Y\, dX' \tag{4}$$

Returning to the actual pressure distributions and vertical velocities, we know that

$$\left.\begin{aligned} \Pi(x') &= 2\rho\cdot e^{i\nu\beta^2 Mx'/c}\cdot\varphi(X) \\ \overline{\Pi}(x') &= 2\rho\cdot e^{-i\nu\beta^2 Mx'/c}\cdot\bar{\varphi}(X) \\ w(x') &= e^{i\nu\beta^2 Mx'/c}\cdot\Phi_Y(X) \\ \overline{w(x')} &= e^{-i\nu\beta^2 Mx'/c}\cdot\bar{\Phi}_Y(X) \end{aligned}\right\} \tag{5}$$

and we get Flax's result.

$$\Pi(x')\cdot\overline{w(x')}\, dx' = \int_{-l}^{+l}\overline{\Pi(x')}\, w(x')\, dx' \tag{6}$$

We now show that $\varphi(X, 0)$ as given by Section (5), Eq. (12) satisfies the identity, Eq. (4).

Consider a reverse flow with vertical velocity $w(x')e^{i\nu t}$ on the airfoil. Then the normal acceleration is

$$(i\nu\bar{w} - V\bar{w}_{x'})e^{i\nu t}$$

and the boundary condition for the Lorentz potential is

$$\bar{\varphi}_Y(X, 0) = i\nu\beta^2\overline{W(X)} - \beta V\,\overline{W}_X$$

where

$$\overline{W(X)} = w(x')\cdot e^{i\nu\beta^2 Mx'/c}$$

Accordingly the regular part of the acceleration potential is

$$\overline{\varphi(\xi,\eta)} = \beta V \cdot \int_0^\pi (i\Omega\overline{w} \sin\eta_1 + \overline{W}_{\eta_1}) \cdot G(\xi,\eta;\eta_1)\, d\eta_1 \tag{7}$$

For the singular solution we now must take

$$\overline{a_0} \cdot G_{\eta_1}(\xi,\eta;0)$$

where $\overline{a_0}$ is determined by integration along the segment $-\infty < X < -\beta l$.

Putting

$$\left.\begin{aligned} \bar{\lambda}_1 &= \frac{\pi}{2}\int_0^\pi \overline{W(\eta_1)} \sin\eta_1 \cdot G_\eta(0,0;\eta_1)\, d\eta_1 \\ \bar{\lambda}_2 &= -\frac{\pi}{2}\int_0^\pi \overline{W(\eta_1)} \sin\eta_1 \cdot G_\eta(0,\pi;\eta_1)\, d\eta_1 \end{aligned}\right\} \tag{8}$$

we get

$$\overline{a_0} = -\bar{\lambda}_1 - \bar{\lambda}_2 \cdot T$$

Now substituting the complete expressions for φ and $\bar{\varphi}$, where

$$\bar{\varphi}(0,\eta) = \beta V \int_0^\pi (i\Omega\overline{W} \sin\eta_1 + \overline{W}_{\eta_1}) \cdot G(0,\eta;\eta_1)\, d\eta_1 - (\lambda_1 + \lambda_2 T) G_{\eta_1}(\xi,\eta;0) \tag{9}$$

into Eq. (4), we get

$$\int_0^\pi\int_0^\pi (i\Omega W \sin\eta_1 - W_{\eta_1}) G(0,\eta;\eta_1)\, d\eta_1 \cdot \overline{W(\eta)} \sin\eta\, d\eta - \int_0^\pi\int_0^\pi (i\Omega\overline{W} \sin\eta_1 + W_{\eta_1}) \times$$

$$G(0,\eta;\eta_1)\, d\eta_1 \cdot W(\eta) \sin\eta\, d\eta - (\lambda_2 + \lambda_1 T) \int_0^\pi G_{\eta_1}(0,\eta,\pi) \cdot \overline{W}(\eta) \sin\eta\, d\eta - (\bar{\lambda}_1 + \bar{\lambda}_2 T) \cdot \int_0^\pi G_{\eta_1}(0,\eta;0) \times$$

$$W(\eta) \sin\eta\, d\eta = -\int_0^\pi\int_0^\pi W_{\eta_1} \cdot G(0,\eta;\eta_1)\overline{W}(\eta) \sin\eta\, d\eta\, d\eta_1 - \int_0^\pi\int_0^\pi \overline{W_{\eta_1}} \cdot G(0,\eta;\eta_1) W(\eta) \sin\eta\, d\eta\, d\eta_1 +$$

$$\frac{2}{\pi}(\lambda_2 + \lambda_1 T) \cdot \bar{\lambda}_2 - \frac{2}{\pi}(\bar{\lambda}_1 + \bar{\lambda}_2 T) \cdot \lambda_1$$

Substituting the identity in the form

$$\int_0^\pi W_{\eta_1} \cdot G(0,\eta;\eta_1)\, d\eta_1 = \frac{1}{\sin\eta} \cdot \int_0^\pi W(\eta_1) \sin\eta_1 \cdot G_\eta(0,\eta;\eta_1)\, d\eta_1 - \lambda_1 G_{\eta_1}(0,\eta;0) - \lambda_2 G_{\eta_1}(0,\eta;\pi) \tag{10}$$

this passes into

$$-\int_0^\pi\int_0^\pi \overline{W}(\eta) \cdot W(\eta_1) \sin\eta_1 \cdot G_\eta(0,\eta;\eta_1)\, d\eta_1\, d\eta \cdot + \lambda_1 \int_0^\pi \overline{W}(\eta) \cdot G_{\eta_1}(0,\eta;0) \sin\eta\, d\eta -$$

$$\int_0^\pi\int_0^\pi \overline{W}_{\eta_1} \cdot G(0,\eta;\eta_1) W(\eta) \sin\eta\, d\eta\, d\eta_1 + \lambda_2 \int_0^\pi \overline{W}(\eta) \cdot G_{\eta_1}(0,\eta;\pi) \sin\eta\, d\eta + \frac{2}{\pi}(\lambda_2\bar{\lambda}_2 - \lambda_1\bar{\lambda}_1)$$

and by partial integration of the first term with respect to η, we get

$$\overline{W}(0) \cdot \int_0^\pi \overline{W}(\eta_1) \cdot \sin\eta_1 \cdot G(0,0;\eta_1)\, d\eta_1 - \overline{W}(\pi) \cdot \int_0^\pi W(\eta_1) \sin\eta_1 G(0,\pi,\eta_1)\, d\eta_1 +$$

$$\int_0^\pi\int_0^\pi \overline{W}_\eta \cdot W(\eta_1) \sin\eta_1 \cdot G(0,\eta;\eta_1)\, d\eta_1\, d\eta - \int_0^\pi\int_0^\pi \overline{W}_{\eta_1} \cdot W(\eta) \cdot G(0,\eta;\eta_1) \sin\eta\, d\eta\, d\eta_1 +$$

$$\frac{2}{\pi}(\lambda_1\bar{\lambda}_1 - \lambda_2\bar{\lambda}_2) + \frac{2}{\pi}(\lambda_2\bar{\lambda}_2 - \lambda_1\bar{\lambda}_1) = \overline{W}(0)\Phi_{\text{reg.}}(0) - \overline{W(\pi)}\ \Phi_{\text{reg.}}(\pi) = 0 \tag{11}$$

since the regular part of $\Phi(\xi,\eta)$ vanishes at the end points of the interval.

References

[1] Timman, R., *Beschouwingen over de luchtkrachten op trillende vliegtuigvleugels*, Thesis, Delft, 1946.

[2] Timman, R., and van de Vooren, A. I., *Theory of the Oscillating Wing with Aerodynamically Balanced Control Surface in a Two-Dimensional, Subsonic, Compressible Flow*, Report F. 54, National Aeronautical Research Institute, Amsterdam, 1949.

[3] Computation Department of the Mathematical Centre, Interim Reports 1–6 on the Oscillating Airfoil in Compressible Flow, 1950

[4] Timman, R., van de Vooren, A. I., and Greidanus, J. H., *Aerodynamic Coefficients of an Oscillating Airfoil in Two-Dimensional Subsonic Flow*, Journal of the Aeronautical Sciences, Vol. 18, No. 12, p. 797, December, 1951.

[5] Dietze, F., *Die Luftkrafte des harmonisch schwingenden Flugels im kompressiblen Medium bei Unterschallgeschwindigkeit*, ZWB, FB 1733 and 1733/2, 1943, 1944.

[6] Fettis, Henry E., *Comments on Aerodynamic Coefficients of an Oscillating Airfoil in Two-Dimensional Subsonic Flow*, Readers' Forum, Journal of Aeronautical Sciences, Vol. 19, No. 5, page

(*Continued on page 250*)

Calculation of Compressible Cascade Flow by the Method of Flux Analysis*

SHIGEO UCHIDA†

Institute of Science and Technology, University of Tokyo

ABSTRACT

A unified graphical method for analyzing the problems of compressible flow through a cascade of arbitrary airfoils is presented. The method is based on the conception that the partial differential equation expressed in terms of suitably chosen curvilinear coordinates may be replaced by an ordinary differential equation in a single variable, the remaining variables being regarded as parameters. The computation reaches, in many cases, a convergent solution after two or three iterations of a graphical procedure. It will be particularly useful for cascades of high solidity.

Comparisons with the exact solutions of incompressible flow past cascades of modified Joukowski airfoils and with the observed results in a cascade wind tunnel are satisfactory considering the accuracies of the graphical methods. Applications are also made to the study of turbine blade sections, in which effects of blade profile, solidity, and Mach Number are investigated.

NOMENCLATURE

x, y	=	cartesian coordinates
α, β	=	orthogonal curvilinear coordinates
s, n	=	arc length of α, β axes, respectively
h_α, h_β	=	parameters in curvilinear coordinates
$\vec{V}$	=	velocity vector
u, v	=	α, β components of $\vec{V}$, respectively
ρ	=	density
p	=	pressure
c	=	sound velocity
γ	=	ratio of specific heats
K	=	constant
ϕ, ψ	=	velocity potential and stream function, respectively
$F(\alpha)$	=	integration constant
N	=	value of n at $\beta = \beta_b$
l	=	chord length
t	=	pitch distance along cascade surface
ρ_1, ρ_2	=	densities of undisturbed flow, up- and downstream, respectively
p_1, p_2	=	pressures of undisturbed flow, up- and downstream, respectively
w_1, w_2	=	total velocities of undisturbed flow, up- and downstream, respectively
w_{a1}, w_{a2}	=	normal components of w_1 and w_2 to the cascade surface, respectively
w_{l1}, w_{l2}	=	tangential components of w_1 and w_2 to the cascade surface, respectively
β_1, β_2	=	angles of attack of w_1 and w_2, respectively
Γ	=	circulation around the unit height of an airfoil
L	=	lift force acting on the unit height of an airfoil
δT	=	summed-up partial torque acting on the blade element defined by r and $r + \delta r$
δC_T	=	partial torque coefficient
r	=	radius of the circumferentially arranged cascade
$\wp$	=	number of blades in the circumferentially arranged cascade
ξ, η	=	cartesian coordinates parallel and perpendicular to the chord line, respectively
a, b	=	half length of major and minor axes of ellipse
ϵ	=	b/a = ratio of radii of ellipse
n	=	order of general ellipse
f, k	=	percentage maximum camber and its distance from leading edge, respectively
e, m	=	percentage maximum thickness and its distance from leading edge, respectively
σ	=	angle of incidence of the airfoils
M_1	=	w_1/c_1 = Mach Number of the undisturbed inlet flow
h, g, c, d	=	parametric constants

Subscripts

0	=	quantities in the state at rest
a, b	=	boundary values
m	=	orders of the approximate solutions

(1) INTRODUCTION

ONE OF THE FUNDAMENTAL AERODYNAMIC PROBLEMS in turbomachinery is the flow of a compressible fluid past cascades. It will be expected, by predicting the flow characteristics through such cascades of airfoils, to obtain appropriate blade designs for a turbine or an axial-compressor of high efficiency. To date a number of methods have been proposed to solve the idealized flow about airfoils arranged in a cascade, involving analytical or semianalytical methods using conformal transformation, superposition of interference, and series expansion;[1-6] graphical or seminumerical procedures;[7-12] and mechanical or electrical techniques.[12-14]

In the present paper a unified graphical method for analyzing the problems of compressible flow past cascades of arbitrary airfoils is presented. As the principle of the method, which has been briefly stated in a previous paper,[11] is based on some general ideas, similar methods may be applied to differential equations of higher order, for example, to those of problems in elasticity or plasticity and others.

The partial differential equation expressed in terms of orthogonal curvilinear coordinates may be replaced by an ordinary differential equation by assuming one of the coordinate axes to be nearly coincident with the

Received June 5, 1953.

* The research on which this paper is based was done by the author as an Aerodynamicist at the Institute of Science and Technology, University of Tokyo. The author expresses his thanks to Prof. S. Kawada for giving valuable suggestions.

† Lecturer of Hydrodynamics, Faculty of Engineering; and Associate Research Scientist.

curves of solution. In the following method of "flux analysis," a stream line is chosen as one of the coordinate axes. Then approximate solutions are obtained by simple integrations, while the stream lines first assumed can be adjusted until they agree with the final solution resulting from the iterative processes. Close approximations may be obtained by the correction of the turning angle or the direction of outlet flow by the value of circulation calculated from the velocity distribution along the airfoil surface. Taking special care with the calculations in the neighborhood of the leading and trailing edges, fairly good results are obtained after two or three iterations. Comparisons both with the accurate cascade flow of modified Joukowski airfoils and with experiments on a cascade of turbine airfoils are shown to be in good agreement. Applications are also made to the basic investigations of turbine blades of high efficiencies. Introducing a series of turbine cascades having a mean camber line in the shape of a general ellipse, effects of the maximum camber and its location, the maximum thickness, the order of ellipse, the pitch chord ratio, and the Mach Number on the surface distribution of velocity and on the magnitude of the circulation are studied and presented, with several examples of flow patterns.

(2) Fundamental Equations Referred to the Orthogonal Curvilinear Coordinates

The steady two-dimensional isentropic flow of a nonviscous compressible fluid is governed by the equations of continuity, irrotationality, and the isentropic relation. Referring to the orthogonal curvilinear coordinates, the fundamental equations are expressed as follows:[15]

$$\text{div}\ (\rho\bar{V}) \equiv \frac{1}{h_\alpha h_\beta}\left[\frac{\partial(h_\beta \rho u)}{\partial \alpha} + \frac{\partial(h_\alpha \rho v)}{\partial \beta}\right] = 0 \qquad (1)$$

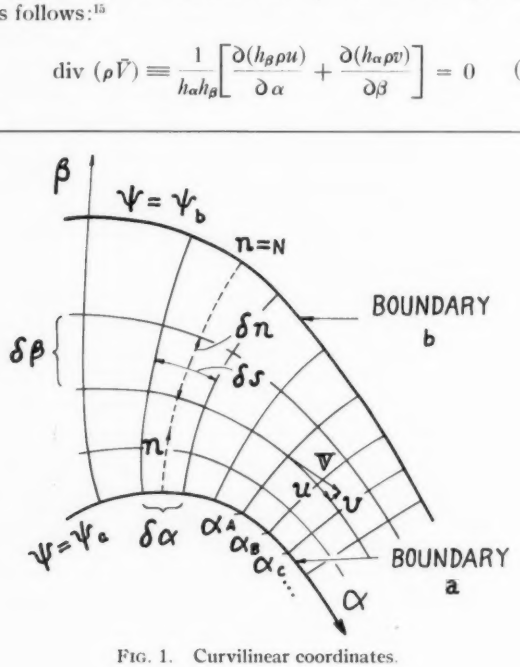

Fig. 1. Curvilinear coordinates.

$$\text{rot}\ \bar{V} \equiv \frac{1}{h_\alpha h_\beta}\left[\frac{\partial(h_\beta v)}{\partial \alpha} - \frac{\partial(h_\alpha u)}{\partial \beta}\right] = 0 \qquad (2)$$

$$p = K\rho^\gamma \qquad (3)$$

where h_α and h_β are the parameters of orthogonal curvilinear coordinates corresponding to the extension factors of the networks.

$$\left.\begin{aligned} h_\alpha &= \lim_{\delta\alpha\to 0}\frac{\delta s}{\delta\alpha} = \sqrt{\left(\frac{\partial x}{\partial \alpha}\right)^2 + \left(\frac{\partial y}{\partial \alpha}\right)^2} \\ h_\beta &= \lim_{\delta\beta\to 0}\frac{\delta n}{\delta\beta} = \sqrt{\left(\frac{\partial x}{\partial \beta}\right)^2 + \left(\frac{\partial y}{\partial \beta}\right)^2} \end{aligned}\right\} \qquad (4)$$

As a function that identically satisfies the condition of continuity, a stream function can be introduced, defined as follows:

$$u = \frac{1}{\rho}\frac{1}{h_\beta}\frac{\partial \psi}{\partial \beta}, \qquad v = -\frac{1}{\rho}\frac{1}{h_\alpha}\frac{\partial \psi}{\partial \alpha} \qquad (5)$$

Substituting Eq. (5) into Eq. (2), the differential equation of ψ referred to the orthogonal curvilinear coordinates is obtained.

$$\frac{\partial}{\partial \alpha}\left(\frac{1}{\rho}\frac{h_\beta}{h_\alpha}\frac{\partial \psi}{\partial \alpha}\right) + \frac{\partial}{\partial \beta}\left(\frac{1}{\rho}\frac{h_\alpha}{h_\beta}\frac{\partial \psi}{\partial \beta}\right) = 0 \qquad (6)$$

The variation of density can be most simply expressed by quantities at the stagnation point, which is given by the use of Bernoulli's equation combined with the isentropic relationship as follows:

$$\rho = \rho_0\left[1 - \frac{\gamma - 1}{2}\left\{\left(\frac{u}{c_0}\right)^2 + \left(\frac{v}{c_0}\right)^2\right\}\right]^{1/(\gamma-1)} \qquad (7)$$

There are many cases where the velocity potential is more convenient. The method to be described in the following can be applied to the velocity potential by a treatment similar to that used for the stream function. For this purpose the velocity potential is introduced, defining, from Eq. (2),

$$u = \frac{1}{h_\alpha}\frac{\partial \phi}{\partial \alpha}, \qquad v = \frac{1}{h_\beta}\frac{\partial \phi}{\partial \beta} \qquad (8)$$

Substituting Eq. (8) into Eq. (1), the differential equation for ϕ is obtained as follows:

$$\frac{\partial}{\partial \alpha}\left(\rho\frac{h_\beta}{h_\alpha}\frac{\partial \phi}{\partial \alpha}\right) + \frac{\partial}{\partial \beta}\left(\rho\frac{h_\alpha}{h_\beta}\frac{\partial \phi}{\partial \beta}\right) = 0 \qquad (9)$$

The variation of density is also given by Eq. (7).

(3) Principle of the Method

Considering an ideal flow of compressible fluid between two fixed boundaries, the principle and procedure of the calculation may be described as follows:

As an inviscid fluid in contact with rigid boundaries flows along the fixed surfaces and has no component of normal velocity, the value of the stream function along

the rigid surfaces is constant. Choosing a group of curved lines for one component of the orthogonal curvilinear coordinates represented, say, by β = constant, the curves $\beta = \beta_a$ and $\beta = \beta_b$ are coincident with the two rigid boundaries a and b as shown in Fig. 1 and accordingly with the stream lines along these surfaces. The boundary conditions are expressed, for example, as follows:

$$\psi = \psi_a \text{ at } \beta = \beta_a \tag{10a}$$

$$\psi = \psi_b \text{ at } \beta = \beta_b \tag{10b}$$

The remaining curves are assumed of similar form to the bounding stream lines. Then more exact shape is to be determined further on in the solution.

On such orthogonal curvilinear coordinates, therefore, $\partial\psi/\partial\alpha$ should be nearly zero along the curves of β = constant, while $\partial\psi/\partial\beta$ should be nearly constant along α = constant, and accordingly each of the two terms in Eq. (6) will become vanishingly small separately.

Under these conditions a good approximation may be obtained by putting

$$\frac{\partial}{\partial\beta}\left(\frac{1}{\rho}\frac{h_\alpha}{h_\beta}\frac{\partial\psi}{\partial\beta}\right) = 0 \tag{11}$$

where it must be noticed that Eq. (11) included only derivatives with respect to a single variable β. Based on iterative methods, the convergent solution will be approached by calculating the correction terms dropped in Eq. (11) or by adjusting the coordinate curves that were first assumed.

Rigorously speaking, the basic conception of this theory is expressed as follows:

Referring to suitably chosen orthogonal curvilinear coordinates, it will be assumed that a partial differential equation can be reduced to an ordinary differential equation in a single variable, the remaining variables being regarded as parameters. Convergent solutions are to be obtained by correcting the parametric variables or by correcting the coordinate axes successively.

For the computational procedures, thus, two sorts of methods have been proposed.

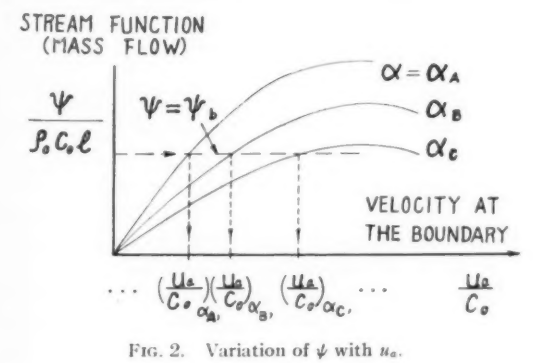

FIG. 2. Variation of ψ with u_a.

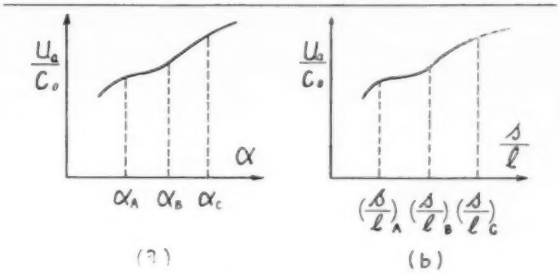

FIG. 3. Velocity distribution.

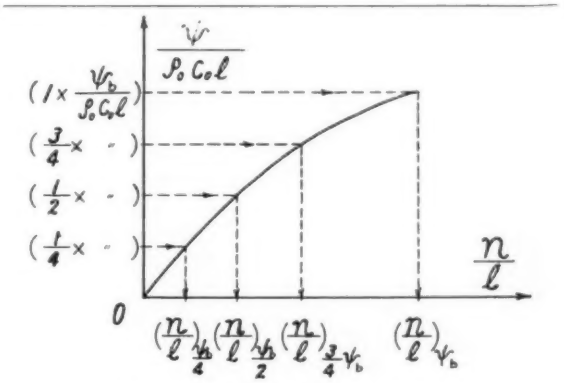

FIG. 4. Distribution of mass flow.

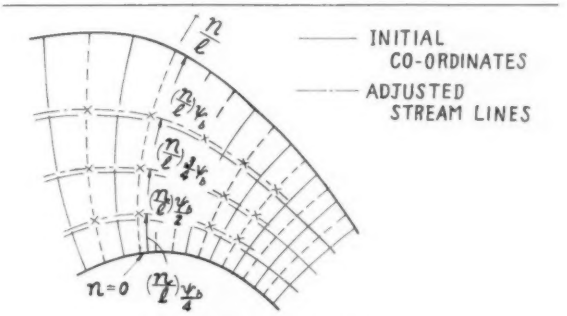

FIG. 5. Stream-line adjustment.

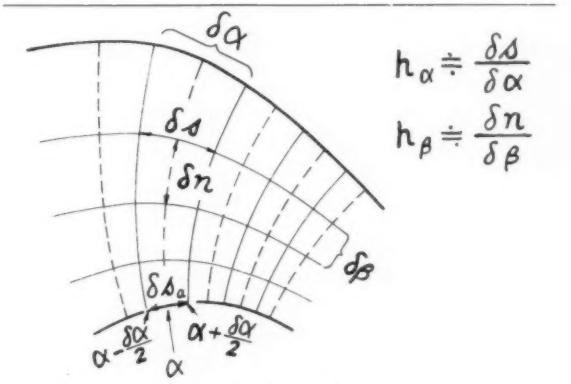

FIG. 6. h_α and h_β.

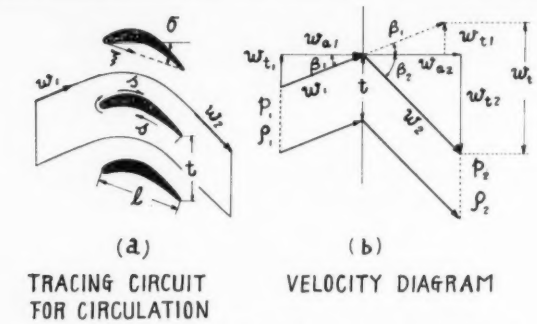

FIG. 7. Nomenclature relating to the undisturbed flows.

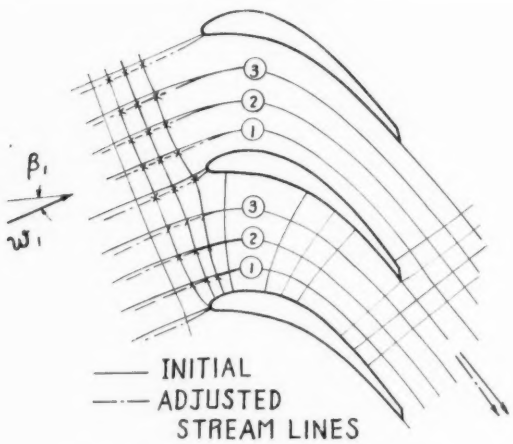

FIG. 8. Adjustment of the inlet stream lines.

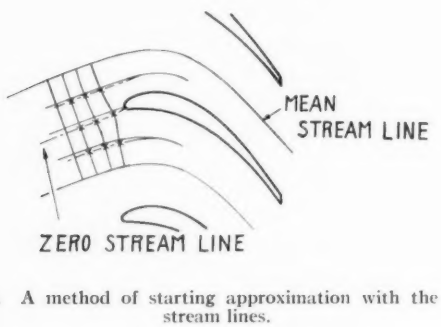

FIG. 9. A method of starting approximation with the mean stream lines.

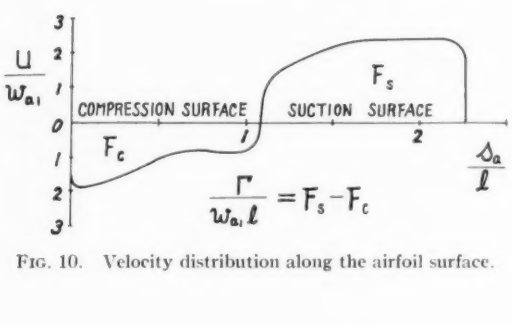

FIG. 10. Velocity distribution along the airfoil surface.

(a) *Method of Fixed Coordinates*

In this method the coordinate axes are left fixed as they are first chosen. Separating the terms in the parametric variable, Eq. (6) will be converted into an ordinary differential equation.

The equation of mth order approximation, ψ_m, is

$$\frac{\partial}{\partial\beta}\left(\frac{1}{\rho_m}\frac{h_\alpha}{h_\beta}\frac{\partial\psi_m}{\partial\beta}\right) = -\frac{\partial}{\partial\alpha}\left(\frac{1}{\rho_{m-1}}\frac{h_\beta}{h_\alpha}\frac{\partial\psi_{m-1}}{\partial\alpha}\right) \tag{12}$$

where the right-hand side represents the correction term that is calculated from quantities of the former approximation. By putting $\partial\psi_0/\partial\alpha = 0$, we have the same expression as Eq. (11) for the first approximation.

The convergent final solution will be obtained by successive substitutions of ψ_m through the integrations of Eq. (12), a brief description of which has been given in the previous paper[11] with some general expressions. The calculations, however, are more or less complicated, since they contain a differential procedure in the course of correcting solutions. For practical purposes, the second method will be more convenient.

(b) *Method of Adjusting Coordinates (Method of Flux Analysis)*

There has been presented an idea that the stream lines calculated from Eq. (11) may be chosen as the more appropriate coordinates for approaching to the convergent solution.[11] Thus, another means of correcting solutions is by successive adjustment of the curvilinear coordinates. In this case it must be noticed that the values of h_α and h_β must also be adjusted at every stage of approximation.

The differential equation for the mth order approximation is expressed as follows:

$$\frac{\partial}{\partial\beta_{m-1}}\left(\frac{1}{\rho_m}\frac{h_{\alpha\cdot m-1}}{h_{\beta\cdot m-1}}\frac{\partial\psi_m}{\partial\beta_{m-1}}\right) = 0 \tag{13}$$

Neglecting the subscripts for the sake of simplicity, integration of Eq. (13) is easily obtained.

$$(1/\rho)(h_\alpha/h_\beta)(\partial\psi/\partial\beta) = F(\alpha) \tag{14}$$

which is rewritten in the form

$$h_\alpha u = F(\alpha) = h_{\alpha\cdot a}u_a \tag{15}$$

or

$$u/u_a = h_{\alpha\cdot a}/h\alpha \tag{15'}$$

where the quantities with subscript a represent the appropriate boundary values (cf. Fig. 1).

Approximate distribution of velocity ratio along the curvilinear coordinate α = constant is given by Eq. (15') as the reciprocal ratio of the extension factor h_α. The constant of integration, $F(\alpha)$ or u_a, is not determined in this stage, but it is obtained from boundary conditions applied to the further integration of Eq. (14) as shown in the following:

Integrating Eq. (14), ψ is given by

$$\psi - \psi_a = \int_{\beta_a} \rho u h_\beta \partial\beta = \int_0 \rho u \delta n \qquad (16)$$

the constant of integration being determined by the boundary condition (10a) as ψ_a, which may be set equal to zero without fear of losing any generality.

In many cases, it will be more convenient to express Eq. (16) in the nondimensional form

$$\frac{\psi}{\rho_0 c_0 l} = \int_0 \frac{\rho}{\rho_0} \frac{u}{c_0} \delta \left(\frac{n}{l}\right) \qquad (16')$$

where the density is given by

$$\frac{\rho}{\rho_0} = \left[1 - \frac{\gamma - 1}{2}\left(\frac{u}{c_0}\right)^2\right]^{1/(\gamma-1)} \qquad (17)$$

Substituting Eq. (15′) into Eq. (16′) with the assumed value of u_a/c_0, ψ can be calculated as a function of u_a/c_0. For the computation it will be convenient to use the numerical table of $\rho u/\rho_0 c_0$ versus u/c_0.

The value of u_a or $F(\alpha)$ is determined from the boundary condition (10b) connected with the integration of Eq. (16′) from the boundary a to b, which is given by

$$\frac{\psi_b}{\rho_0 c_0 l} = \int_0^{N/l} \frac{\rho}{\rho_0} \frac{u}{c_0} \delta \left(\frac{n}{l}\right) \qquad (18)$$

Generally, u_a or $F(\alpha)$ cannot be solved in analytical form except for the case of incompressible flow, in which case u_a is calculated in the form

$$\frac{u_a}{U} = \frac{\psi_b}{\rho_0 U l} \Big/ \int_0^{N/l} \frac{h_{\alpha \cdot a}}{h_\alpha} \delta \left(\frac{n}{l}\right) \qquad (19)$$

where U represents a standard velocity.

In the case of a compressible fluid, calculation of ψ_b for several values of assumed u_a enable us to determine the boundary value u_a by numerical or graphical interpolation. These procedures are schematically shown in Fig. 2.

Expression of the values of u_a versus α or s gives the velocity distributions along the boundary a as shown in Fig. 3.

The velocity distribution and, accordingly, the distribution of stream function or mass flow along the coordinate of α = constant is also calculated from Eq. (15′) and Eq. (16′), respectively, by substituting the value of u_a. As the latter represents the quantity of ψ or mass flow through the divided section lying between the rigid boundary and the point concerned, the positions where the stream lines should be passed can be determined, and therefore, the stream lines can be drawn as described in the following procedure:

Dividing the total mass flow into several equal parts—for example, four parts—the values of n/l corresponding to the stream lines of $^1/_4$, $^1/_2$, and $^3/_4$, respectively, will be given as illustrated in Fig. 4. Marking these points along the coordinates of α = constant and connecting the adjacent positions belonging to the same ψ from point to point, stream lines will be drawn as shown in Fig. 5.

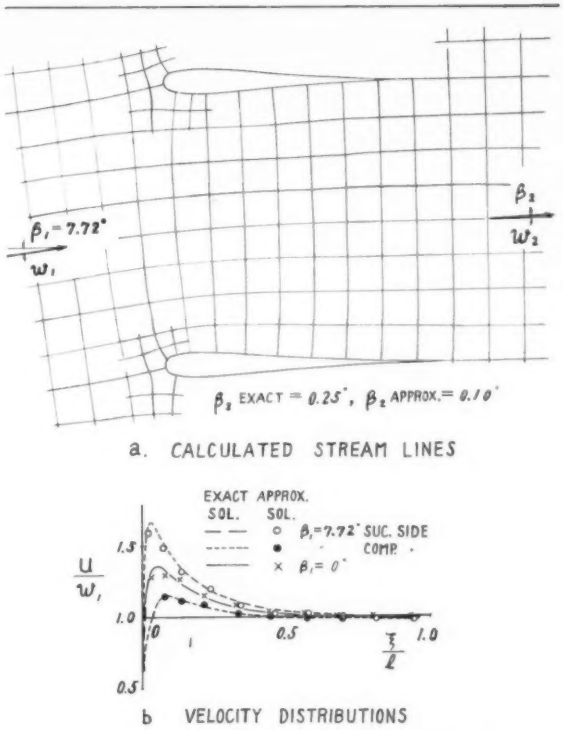

FIG. 11. Flow through cascade of modified Joukowski Airfoils (incompressible).

The stream lines thus obtained will generally deviate from the coordinate curves of β = constant, which were first assumed to be nearly coincident with the stream lines.

The second stage of continuing the computation is started by taking the calculated stream lines as a component of the orthogonal curvilinear coordinates—i.e., β = constant. Another component of α = constant will be determined as groups of curves which orthogonally cross the curves of β = constant at every intersection, which may be conveniently drawn in graphically.

The differential equation for the second approximation referred to the new curvilinear coordinates is also expressed by Eq. (13) and is integrated in the form of Eq. (14) or Eq. (15′), the latter giving the distribution of velocity ratio by the reciprocal ratio of the adjusted h_α.

It must be noted that in the limit process, as contained in Eq. (4) in the expressions for h_α and h_β, the accuracy of calculation will be diminished with the reduction of the small division, $\delta\alpha$ or $\delta\beta$. For practical purposes, therefore, finite differences will replace the derivatives of h_α or h_β,

$$h_\alpha = \delta s/\delta\alpha, \qquad h_\beta = \delta n/\delta\beta \qquad (4')$$

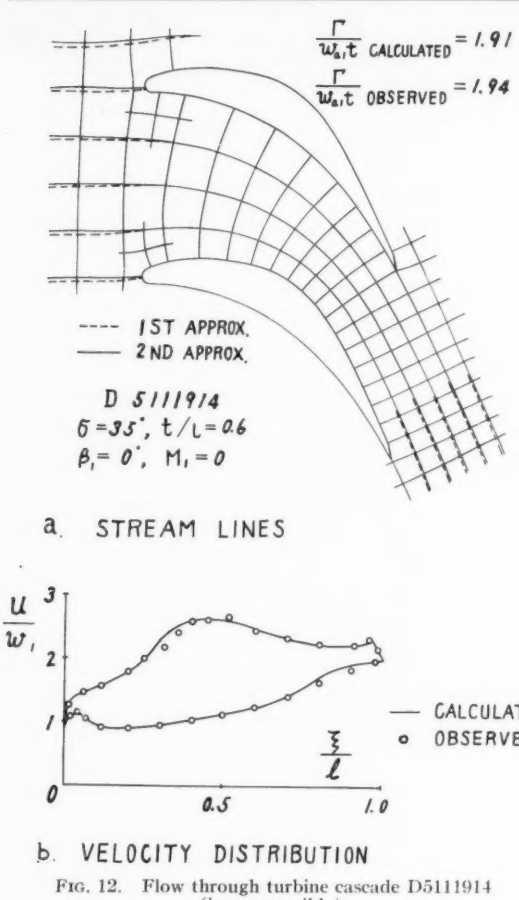

FIG. 12. Flow through turbine cascade D5111914 (incompressible).

If, taking an appropriate difference $\delta\alpha$, the coordinate lines of $\alpha - (\delta\alpha/2)$ and $\alpha + (\delta\alpha/2)$ constant, respectively, are drawn, the coordinate differences between these two curves at any value of β will be equal to $\delta\alpha$. (Fig. 6.) The velocity ratio expressed by Eq. (15′) therefore will be replaced by the reciprocal ratio of the arc lengths divided by these two coordinate lines as follows:

$$u/u_a = \delta s_a/\delta s \tag{15″}$$

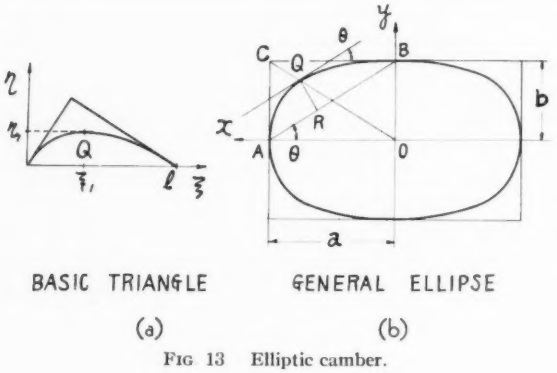

FIG 13 Elliptic camber.

The boundary values u_a are determined by the procedure described previously, and thus the successive calculations are continued and repeated until the convergent solution is reached.

Dividing the stream lines with the same difference of $\delta\phi = u\delta s$, equipotential lines can be drawn as the orthogonal curves to the stream lines, and thus flow patterns will be completed.

(4) Computational Procedure on the Flow Through a Rectilinear Cascade

(a) *Factors Characterizing the Cascade Flow*

In order to get reasonable approximations in the flow through cascades, it will be necessary to insert corrections to the flow angles of the outlet stream. For this reason, some relationships between characteristic parameters in the cascade flow are introduced.

A diagrammatic representation of the undisturbed velocities at points at infinite distances is presented in Fig. 7.

The flow is governed by the continuity, momentum, and energy equations with isentropic change, respectively,

$$\rho_1 w_{a1} = \rho_2 w_{a2} = (\rho\Gamma) \tag{20}$$

$$L = (\rho\Gamma)t(w_{t1} + w_{t2}) \tag{21}$$

$$\frac{w_1^2}{2} + \frac{\gamma}{\gamma - 1}\frac{p_1}{\rho_1} = \frac{w_2^2}{2} + \frac{\gamma}{\gamma - 1}\frac{p_2}{\rho_2} \tag{22}$$

$$p_2/p_1 = (\rho_2/\rho_1)^\gamma = (c_2/c_1)^{\gamma/(\gamma-1)} \tag{23}$$

where L represents the force component in the direction of the cascade surface acting on the unit height of an airfoil. Denoting the circulation around an airfoil by Γ, the next relationship will be obtained by tracing the circuit in Fig. 7.

$$\Gamma = t(w_{t1} + w_{t2}) \tag{24}$$

where the circulation is also defined by the contour integral along the surface of an airfoil as follows:

$$\Gamma = \oint u_a\, ds \tag{25}$$

Substitution of Eq. (24) into Eq. (21) gives

$$L = (\rho V)\Gamma \tag{26}$$

It is obvious that this relationship similar to the Kutta-Joukowski theorem holds in the compressible cascade flow only in the particular direction tangential to the cascade surface. If a circumferentially arranged cascade can be approximately replaced by the rectilinear cascade, the coefficient of total torque acting on the blade height of δr at the radius of r may be introduced, defining

$$\delta C_T = \delta T/(1/2)\rho_1 w_{a1}{}^2 \cdot r \cdot 2\pi r\delta r \tag{27}$$

where δT is given by

$$\delta T = \wp L r \delta r = \wp(\rho\Gamma)\Gamma r \delta r \tag{28}$$

Hence,

$$\delta C_T = \frac{\wp}{\pi}\frac{\Gamma}{w_{a1} r} = 2\frac{\Gamma}{w_{a1} t}$$

$$= 2\,[\tan\beta_1 + (w_{a2}/w_{a1})\tan\beta_2] \tag{29}$$

The corrections of the outlet flow angle are made by using the relationship between flow angles and circulation.

Transforming Eq. (22) with Eqs. (23) and (20), the following expression is obtained:

$$\left[\left(\frac{w_{a2}}{w_{a1}}\right)^2\left(\frac{\cos\beta_1}{\cos\beta_2}\right)^2 - 1\right]\frac{\gamma-1}{2}\left(\frac{w_1}{c_1}\right)^2 = 1 - \left(\frac{w_{a1}}{w_{a2}}\right)^{\gamma-1} \tag{30}$$

or

$$\tan\beta_2 = \left\{\left[\frac{1 - \left(\frac{w_{a1}}{w_{a2}}\right)^{\gamma-1}}{\frac{\gamma-1}{2}\left(\frac{w_1}{c_1}\right)^2} + 1\right]\left(\frac{w_{a1}}{w_{a2}}\right)^2 \frac{1}{\cos^2\beta_1} - 1\right\}^{1/2} \tag{31}$$

where w_{a1}/w_{a2} is given by Eq. (29) as a function of $\tan\beta_2$,

$$\frac{w_{a1}}{w_{a2}} = \tan\beta_2 \Big/ \left(\frac{\Gamma}{w_{a1} t} - \tan\beta_1\right) \tag{32}$$

Under the given values of the angle and Mach Number of the inlet uniform flow, the relationship between β_2 and Γ—i.e., outlet flow angle and circulation—will be calculated from Eqs. (31) and (32).

For the case of an incompressible fluid, expressions are simplified by putting $w_{a1} = w_{a2}$,

$$\tan\beta_2 = (\Gamma/w_{a1} t) - \tan\beta_1 \tag{33}$$

(b) *Calculation of the Inlet Stream Lines*

Stream lines bounded by two fixed surfaces of the adjacent airfoils are easily obtained by the successive approximation described in the previous sections. The

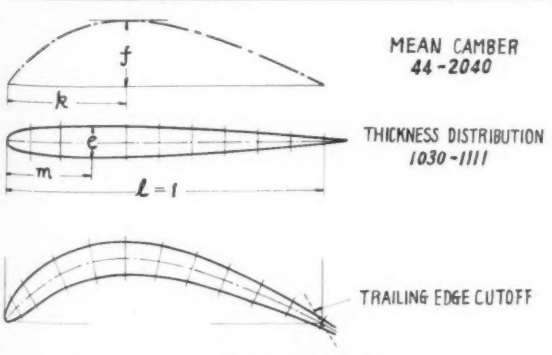

FIG. 14. Construction of the airfoil section.

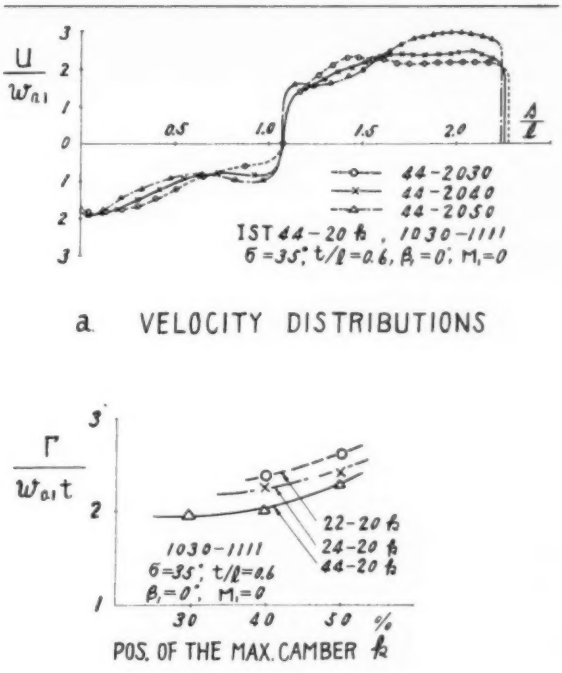

FIG. 15. Effect of the maximum camber location.

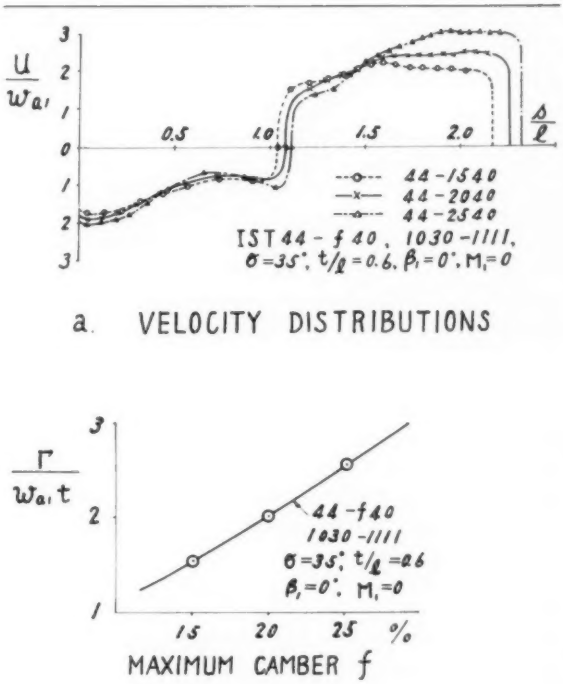

FIG. 16. Effect of the maximum camber.

method, however, must be slightly changed on the stream lines at the inlet or outlet portions, where the coordinate axes of α = constant will be extended to an infinite distance.

In the graphical analyses, as well as the numerical ones, it will be impossible to deal directly with the problems in the infinite field. It is usual, therefore, to introduce some practical assumptions that the flow reaches a uniform state corresponding to the point at infinity at some definite distance adequately taken from the cascade surfaces.

An example of the inlet stream lines of β = constant are shown in Fig. 8, with the perpendicular coordinates of α = constant extended to the assumed uniform state. Since the magnitude and direction of the uniform flow is given and the distributions of the velocity ratio are computable from Eq. (15′) or (15″), it is evident that the velocity distributions along the coordinate α = constant can be calculated in this case. In other words, the integral constant u_a is determined at this stage of the approximation. Proceeding with succeeding calculations, therefore, the corrections of the stream lines or coordinate axes can be performed with no difficulty. In these processes the zero stream line to the forward stagnation point is also determined, though its accuracy cannot be expected to be excellent.

In many cases it is convenient to assume the form of mean stream line first for determining the zero stream line to start the calculations (cf. Fig. 9).

It must be noticed, in any case, that the corresponding stream lines on the adjacent airfoils should have the same forms. This property will simplify the calculations to a great extent.

(c) *Calculations of the Outlet Stream Line*

In the case of the outlet stream line, the principal parts of the calculations are the same as those of the inlet flows, but the procedures are more laborious, since neither the magnitude nor the directions of the outlet uniform flows are known beforehand. In order to determine these values, corrections are necessary as mentioned previously.

Assuming the directions of the uniform flows, in the first step, outlet stream lines can be calculated and determined in a similar way as the inlet stream lines. If the airfoil has a sharp trailing edge, leaving stream lines should be separated at this point corresponding to Joukowski's assumption for the isolated airfoils.

The calculations are then carried out through the whole field. When it reaches a convergent state, the solution of cascade flow under the assumed direction of the outlet stream will be obtained. Using the velocity distributions along the surface of the airfoil, the circulation around the airfoil is also calculated from Eq. (25) (cf. Fig. 10).

Substituting the value of Γ into Eq. (32), the correction of the outlet flow angle will be obtained from Eq. (31) by numerical calculation.

The next approximation will be started by adjusting the outlet flow direction, and the whole procedure previously described is repeated until a convergent solution is practically reached, where the correction to the outlet flow direction is regarded as negligibly small.

As the correction is small in many cases, two or three iterations will be sufficient for practical purposes.

(5) Illustrative Examples

For the purpose of inspecting the accuracy of the method and of forming an estimate of its validity, comparison is made with some analytical solutions.

For an example of an exact solution, let us introduce the complete solution of the incompressible cascade flow,[16, 17] which was obtained by transforming the isolated Joukowski airfoils into cascade arrangements. A Joukowski transformation connected with the mapping function of the cascade of flat plate gives airfoil contours with no stagger, as shown, for example, in Fig. 11a. Applying the method of "flux analysis" to these cascades of modified Joukowski airfoils, two cases of inlet flow angle—i.e., $\beta_1 = 0°$ and $7.72°$—are calculated, the velocity distributions and stream lines of which are given in Fig. 11.

In spite of the low accuracy of the method for the flow through a cascade of such a low solidity, the values are in fairly good agreement with the analytical solutions. The angle of the outlet uniform flow is also determined with sufficient accuracy for practical purposes (cf. Fig. 11a).

Another examination is then made by comparing with the experimental results on the cascade of a turbine airfoil.[18] The experiments were made in a cascade wind tunnel having adjustable walls in the downstream section. The outlet flow angle was determined by adjusting the movable walls so that the lift coefficient calculated from the momentum change between undisturbed flows coincided with that obtained by the integration of the measured pressure distributions.

Calculating the stream lines and pressure distributions of the flow through this cascade, fairly good agreement is also shown between the analysis and observation as presented in Fig. 12, where the values of both circulations are nearly coincident.

From the considerations on computational accuracies, it is expected that the presented method of analysis will be suited to practical calculations of the flow through cascade of arbitrary arrangement.

(6) Turbine Cascade of IST-Series

In order to get the basic profiles suitable for starting the calculation of predicting velocity distributions, a study has been made by the "flux analysis" of the char-

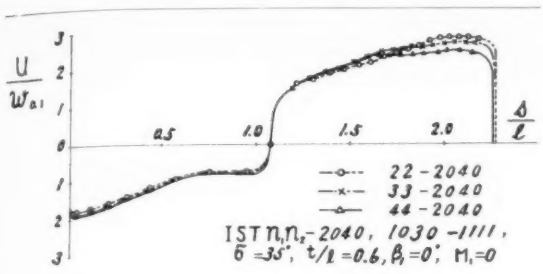

a. VELOCITY DISTRIBUTIONS

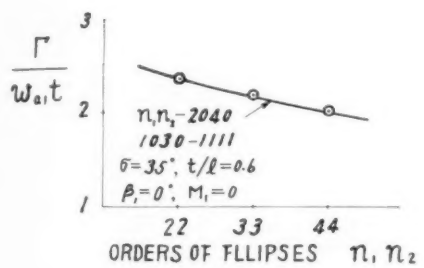

b. CIRCULATION

FIG. 17. Effect of the orders of elliptic camber (1).

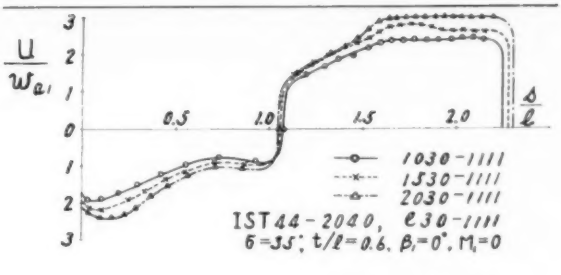

a VELOCITY DISTRIBUTIONS

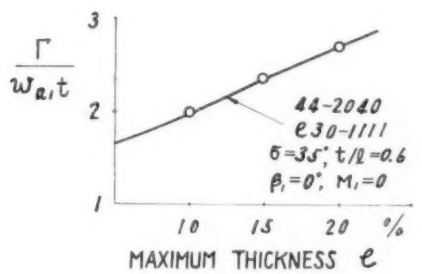

b. CIRCULATION

FIG. 19. Effect of the maximum thickness.

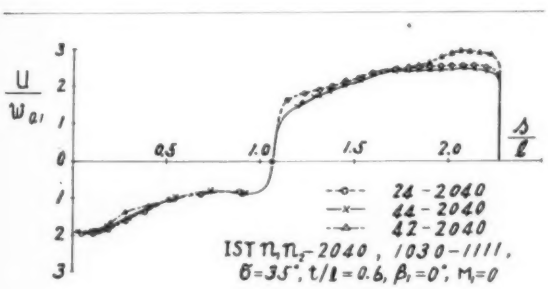

a. VELOCITY DISTRIBUTIONS

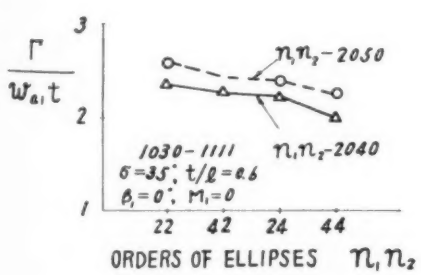

b. CIRCULATION

Fig. 18. Effect of the orders of elliptic camber (2).

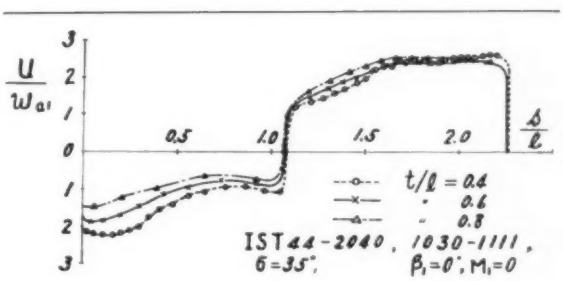

a. VELOCITY DISTRIBUTIONS

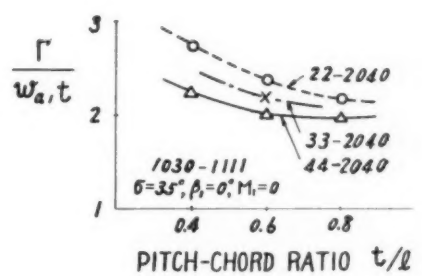

b. CIRCULATION

FIG. 20. Effect of the pitch-chord ratio.

acteristics of flow through a systematic series cascades designed at the Institute of Science and Technology.

(*a*) *Mean Camber Line*

The chord line and the two tangents to the camber line at the leading and trailing edges form a triangle called the "basic triangle" of cascade airfoils, the vertical angle of which might be supposed to have some relations with the turning angle of cascade flows. For the camber line, therefore, a smooth curve that is inscribed in the basic triangle with appropriate vertical angle, as shown in Fig. 13a, may be desirable.

For this purpose a series of general elliptic cambers is introduced, the basic form of which is reduced from the ellipse of nth order (cf. Fig. 13b).

$$(x/a)^n + (y/b)^n = 1 \tag{34}$$

a quarter part of which is used for the camber line. The coordinates relating to the chord line and its normal are calculated by the following formulas:

$$\left.\begin{aligned} \xi/l &= [a(a - x) + by]/(a^2 + b^2) \\ \eta/l &= \{ay - b(a - x)\}/(a^2 + b^2) \end{aligned}\right\} \tag{35}$$

Denoting the coordinates for the point of the maximum camber Q, by x_1, y_1 or ξ_1, η_1, the following relationship is easily verified:

$$x_1/a = y_1/b = 2^{-1/n} \tag{36}$$

Substituting Eq. (36) into Eq. (35), the position and magnitude of the maximum camber are, respectively, given by

$$\left.\begin{aligned} k &= \frac{\xi_1}{l} = \left\{1 - (1 - \epsilon)\left(\frac{1}{2}\right)^{1/n}\right\}\frac{1}{1 + \epsilon^2} \\ f &= \frac{\eta_1}{l} = \left\{2\left(\frac{1}{2}\right)^{1/n} - 1\right\}\frac{\epsilon}{1 + \epsilon^2} \end{aligned}\right\} \tag{37}$$

where $\epsilon = b/a$. It is convenient for practical computations to calculate ϵ and η for the designated value of n and k. The formula is given as follows:

$$\epsilon = \sqrt{(k + 2^{-1/n} - 1)/(2^{-1/n} - k)} \tag{38}$$

If it is necessary, formulas giving n and ϵ for the designated k and f are also introduced after brief computations.

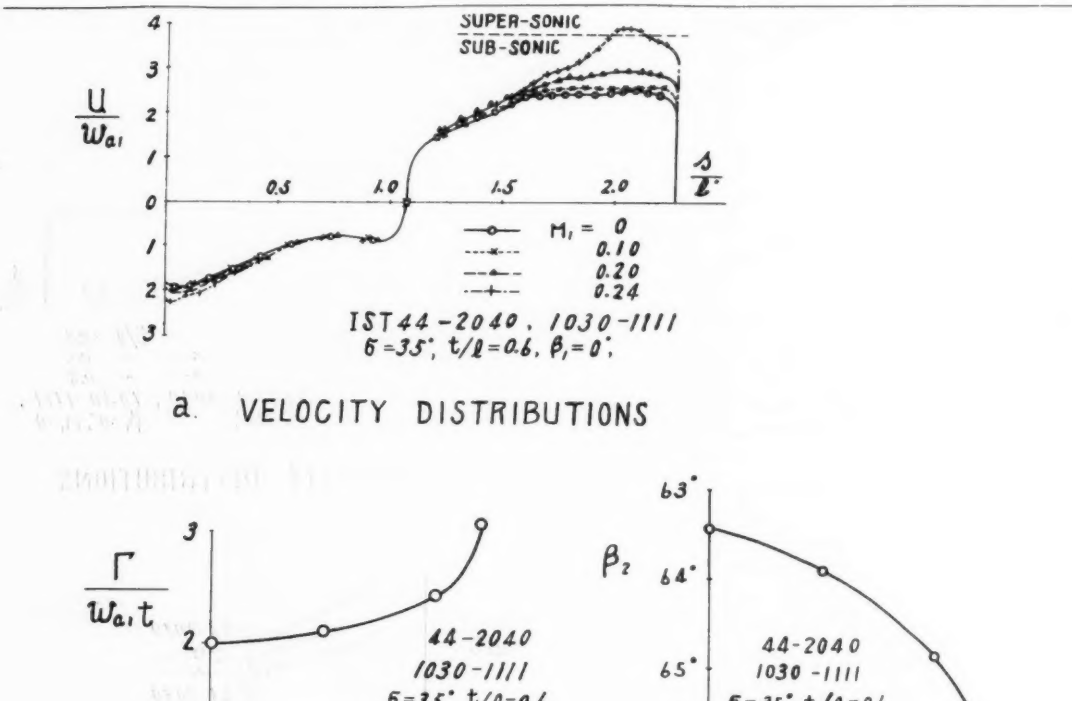

FIG. 21 Effect of the inlet Mach Number

The basic cambers thus obtained are then deformed by elongating the figures along the normal direction to the chord line so that the vertical angle or the maximum camber reaches the desired value.

In some cases combinations of ellipses of different order divided at the point of the maximum camber are employed to get the effects of form factor in the front and rear parts separately.

(b) *Thickness Distributions*

Separating the thickness distribution into two parts, polynomial expressions introduced in the study of isolated laminar airfoils[19, 20] are used. They are given by the following expressions ahead of and behind the maximum thickness, respectively:

$$\frac{h}{l} = \frac{e}{l}\left\{\left(2g\,\frac{\xi}{l}\right)^{1/2} + g_1\frac{\xi}{l} + g_2\left(\frac{\xi}{l}\right)^2\right\} \tag{39}$$

for $0 \leqq \xi/l \leqq m$,

$$\frac{h}{l} = \frac{e}{l}\left\{c + d_1\left(1 - \frac{\xi}{l}\right) + d_2\left(1 - \frac{\xi}{l}\right)^2 + d_3\left(1 - \frac{\xi}{l}\right)^3\right\} \tag{40}$$

for $m \leqq \xi/l \leqq 1$

Coefficients are determined so that the radius of the leading edge circle is equal to $g(e/l)^2 l$; that, $h = e/2$ and $dh/d\xi = 0$ at $\xi/l = m$; and that, $h = ce$ and $dh/d\xi = -d_1(e/l)$ at $\xi/l = 1$.

In the following examples constants are chosen as:

$$m = 0.30, \qquad g = 1.1, \qquad d_1 = 1.1 \tag{41}$$

(c) *Blade Profiles and Their Arrangements*

Examples of camber line and thickness distribution are given in Fig. 14.

The superposition is made by taking the thickness height perpendicularly to the mean camber line at the corresponding percentage locations along the chord line.

The cascade arrangements of the airfoils are determined by giving the setting angle—for example, the angle σ between chord line and turbine axis—and pitch chord ratio, t/l (cf. Fig. 7a).

IST-cascade series are described by three groups of numbering—for example, in

$$\begin{array}{l} \text{IST 24-2040} \\ 1030 \quad \text{-}1111 \\ \sigma \quad = 35°, \quad t/l = 0.6 \\ \beta_1 \quad = \ 0°, \quad M_1 = 0.2 \end{array} \tag{42}$$

the first line represents the form of camber line; the second, the thickness distribution; and the third, the arrangement. Adding the flow conditions in the last line, the flows will be completely determined.

In the numbering of the camber line the first two numbers represent the orders of the ellipses ahead of, and behind, the point of the maximum camber. re-

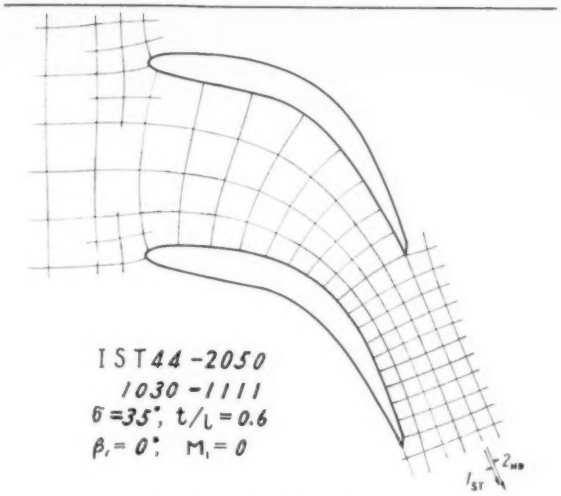

FIG 22. Flow pattern (1)

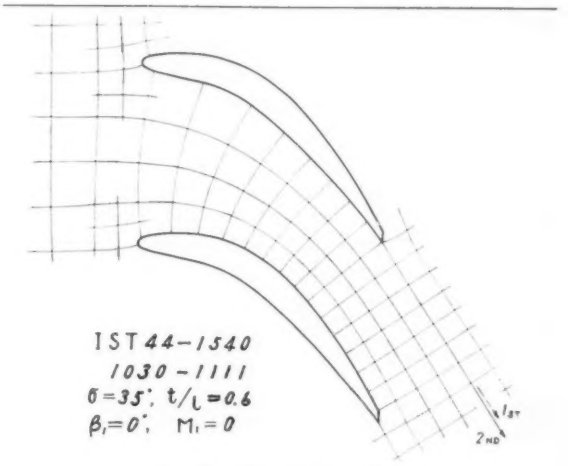

FIG. 23. Flow pattern (2).

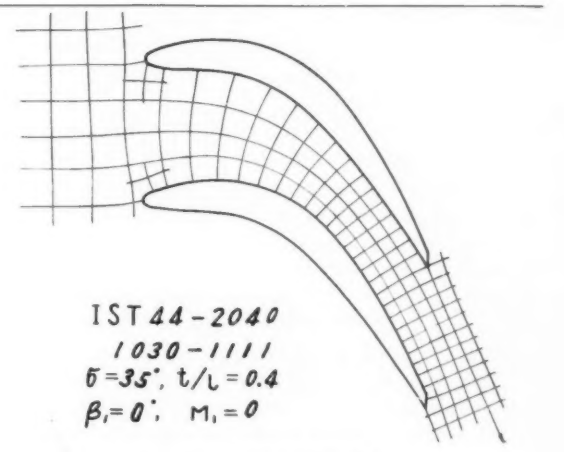

FIG. 24 Flow pattern (3).

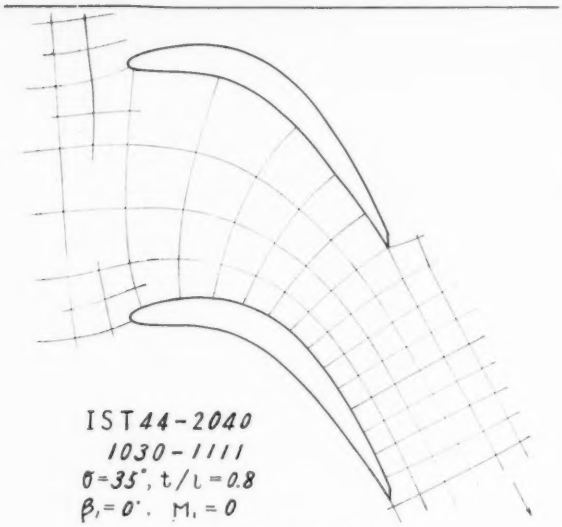

FIG. 25. Flow pattern (4).

spectively, so the different numbers indicate a combined camber line. The two numbers immediately behind the hyphen represent the amount of the maximum camber and the last two the location of the maximum camber both as percentages of the chord length.

The numbering of the thickness distribution consists of four groups of two numbers, each representing, in order, the maximum thickness e/l; its position m, both as percentages of the chord length; value of $10g$ related to the leading edge radius; and value of $10d_1$, defining the trailing-edge inclination. The coefficient of trailing-edge thickness is chosen as $c = 0.08$ from practical considerations.

(7) Flow Through Turbine Cascades of IST-Series

In the graphical, as well as numerical, calculations, summary figures will be given for systematic variations of parameters. Examples will be presented of the effect of various factors on the cascade flow. Results are given in the form of velocity distributions along the airfoil surface, variations of the circulation referring to each parameter, and some examples of flow patterns. The velocity distribution is evidently the most significant expression of the airfoil characteristics, since it gives not only the intensity of circulation but also the basic data for the resistance calculations in the boundary layers. The conditions that must be satisfied by the profile of high efficiency are that the maximum velocity be far from the leading edge for the purpose of delaying the transition in the boundary layer and that the region of high velocity should be restricted as much as possible in order to reduce the frictional resistance. These conditions might be accomplished to a considerable extent by a profile of uniform velocity distribution. As it is difficult to attain these conditions on both surfaces of cascade airfoils, more attention is usually paid to the suction surface, where the higher velocity causes more resistance than that on the compression surface. Any increase of surface velocity along the suction side causes an increase of circulation and surface resistance at the same time; therefore, the most effective correction may be to approach a uniform velocity distribution. On the compression side, low velocities are obviously desirable, but the flows are accelerated in the neighborhood of trailing edge by the interference in cascade arrangements.

(*a*) *Effect of the Location of the Maximum Camber*

The location of the maximum camber controls mainly the position of the peak velocity, as shown in Fig. 15. In these examples, a profile of $k = 30$ per cent gives a peak point too far forward, and conversely the profile of $k = 50$ per cent gives maximum velocity toward the rear.

(*b*) *Effect of the Magnitude of the Maximum Camber*

The magnitude of the maximum camber seems to have an influence on the value of the surface velocity, especially over the rear part of the profile (cf. Fig. 16).

The maximum camber has an influence on the value of circulation as presented in Fig. 16b, where Γ is shown in a quasilinear relationship with the magnitude of the maximum camber.

(*c*) *Order of the Elliptic Camber*

The ellipses of higher order give a camber line of greater curvature in the vicinity of the maximum camber point, while those of lower order distribute the curvature over the airfoil. Effects on the velocity distributions are more or less systematic but are not so great as for the other parameters. The case of equal order for front and rear parts of the airfoil is shown in Fig. 17 and that of different orders in Fig. 18.

(*d*) *Effect of the Maximum Thickness*

Three cases of $e = 10$, 15, and 20 per cent are compared in Fig. 19, where the effect of increasing thickness is evident in the increase of velocities along both surfaces. Since the higher velocities cause increased frictional losses in real fluids, thick profiles will not be desirable for cascades of high efficiency, even if they have possibilities of increasing the circulation. Such high velocities in the flow passages will reduce the performance, especially for compressible fluids.

(*e*) *Influence of the Pitch-Chord Ratio*

The solidity influences the velocity distribution along the compression surface in the special form, as shown in Fig. 20, where increasing solidity results in increased velocities. So the surface friction will be greater in the cascade with narrower passages, and therefore the total losses obtained by multiplying the number of blades

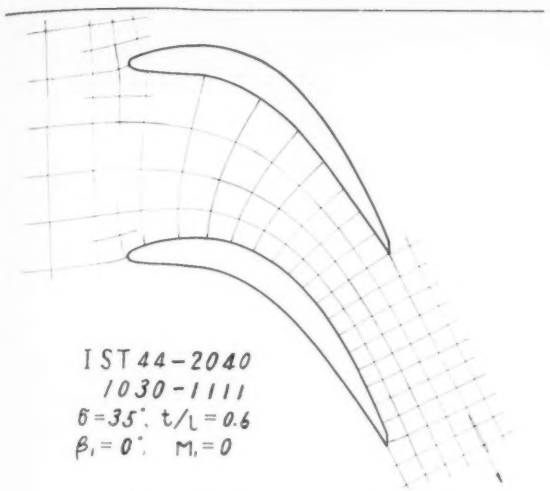

FIG. 26. Flow pattern (5).

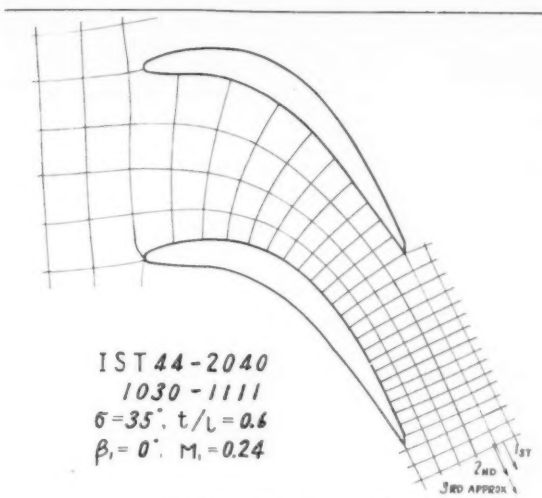

FIG. 27. Flow pattern (6).

will be increased. In approaching arrangements of higher solidity, the torque coefficient is also increased but perhaps to a somewhat lower degree than the case of total losses. It is supposed, therefore, that there may be an appropriate solidity for a high-efficiency cascade, which gives a considerable amount of torque with comparatively small losses. High efficiencies will be expected in the vicinity of $t/l = 0.6 \sim 0.7$.

(f) *Influence of the Mach Number*

Influence of the Mach Number is studied on the standard airfoil. The calculated variation of the velocity ratio along the profile surface is shown in Fig. 21. As is well known, the effect of compressibility appears in the region of high velocity to the greatest extent. The distributions of velocity ratio are not greatly different in the low velocity regions of the front part. Remarkable variations are presented in the high-velocity region near the narrowest part of the flow path, where, according to the increase of the inlet Mach Number, the maximum velocity becomes extraordinarily high and, finally, it exceeds the sonic velocity.

An example of the compressibility effects on the circulation and turning angles is also presented in Figs. 21b and 21c, respectively.

APPENDIX

Several examples of flow patterns are presented in Figs. 22–27.

REFERENCES

[1] Traupel, W., *Calculation of Potential Flow Through Blade Grids*, Sulzer Tech. Rev., No. 1, pp. 25–42, 1945.

[2] Goldstein, Arthur W., and Jerison, M., *Isolated and Cascade Airfoils with Prescribed Velocity Distribution*, NACA TR No. 869, pp. 201–215, 1947.

[3] Vazsonyi, A., *On the Aerodynamic Design of Axial-Flow Compressors and Turbines*, Jour. of Appl. Mech., Vol. 15, No. 1, pp. 53–64, March, 1948.

[4] Lin, C. C., *On the Subsonic Flow Through Circular and Straight Lattices of Airfoils*, Jour. of Math. & Phys., Vol. 38, No. 2, pp. 117–130, July, 1949.

[5] Costello, George R., *Methods of Designing Cascade Blades with Prescribed Velocity Distributions in Compressible Potential Flows*, NACA TR No. 978, pp. 559–569, 1950.

[6] Wu, Chung-Hua, and Brown, Curtis A., *A Theory of the Direct and Inverse Problems of Compressible Flow Past Cascade of Arbitrary Airfoils*, Journal of the Aeronautical Sciences, Vol. 19, No. 3, pp. 183–196, March, 1952.

[7] Flügel, G., *Ein neues Verfahren der graphischen Integration, angewandt auf Strömungen idealer Flüssigkeit in Kreiselräder*, Zeitschr. f. das gesamte Turbinenwesen, Vol. 12, pp. 73–77, 89–91, 100–103, 1915.

[8] Flügel, G., *Mehrdimensionale Strömung von Gasen*, Zeitschr. f. das gesamte Turbinenwesen, Vol. 16, pp. 161–165 and 178–180, 1919.

[9] Bryan, G. H., *The Effect of Compressibility on High Speed Stream Line Motions*, T. R. of Adv. Comm. Aer., Rep. No. 555, pp. 130–150, December, 1918, and Rep. No. 640, pp. 79–109, April, 1919.

[10] Stodola, A., and Lowenstein, L. C., *Steam and Gas Turbines*, Sect. 170, p. 992; McGraw-Hill Book Company, Inc., New York, 1927.

[11] Uchida, S., *A New Approximate Solution in Boundary Value Problems by the Use of Orthogonal Curvilinear Coordinates*, Rep. of Inst. Sci. Tech., Univ. of Tokyo, Vol. 1, No. 7-8, pp. 101–105, July-August, 1947 (in Japanese); Jour. of Phys. Soc. Japan, Vol. 3, No. 1, pp. 33–40, January-February, 1948.

[12] Poritsky, H., Sells, B. E., and Danforth, C. E., *Graphical, Mechanical, and Electrical Aids for Compressible Fluid Flow*, Jour. of Appl. Mech., Vol. 17, No. 1, pp. 37–46, March, 1950.

[13] Taylor, G. I., and Sharman, C. F., *A Mechanical Method for Solving Problems of Flow in Compressible Fluids*, Proc. of Roy. Soc. London, Ser. A., Vol. 121, No. A 787, pp. 194–217, November, 1928.

[14] Otsuka, S., *Latticed Wing Solution with the Aid of Electricity*, Rep. of Inst. Sci. Tech., Univ. of Tokyo, Vol. 4, No. 1-2, pp. 49–55, January-February, 1950 (in Japanese with English abstract).

[15] Milne-Thomson, L. M., *Theoretical Hydrodynamics*, 1st Ed., p. 55; The Macmillan Company, London, 1938.

[16] Weinig, F., *Die Strömung um die Schaufeln von Turbomaschinen*, p. 55; Johann Ambrosius Barth, Leipzig, 1935.

[17] Kawasaki, T., *Calculation on the cascade of symmetrical Joukowski airfoils*, T. M. of Gas Turbine Res. in Railway Tech. Lab., No. 9, pp. 1–8, August-October, 1948 (in Japanese).

[18] Numachi, F., and Kurokawa, T., *Model Air Test on Guide Vane Blades of Gas Turbine*, Trans. of Japan Soc. Mech. Engrs., Vol. 15, No. 51, pp. 46–52, 1950.

[19] Tani, I., and Noda, T., *Design of symmetrical aerofoils with the lowest pressure well back*, Jour. of Aero. Res. Inst., No. 190, pp. 207–215, June, 1940 (in Japanese).

[20] Tani, I., and Mituisi, S., *Contributions to the Design of Aerofoils Suitable for High Speeds*, Rep. of Aero. Res. Inst., Tokyo Imp. Univ., Vol. 15, No. 198, pp. 399–415, September, 1940.

Linearized Theory of the Oscillating Airfoil in Compressible Subsonic Flow

(*Continued from page 236*)

353, May, 1952. See also Timman, R., van de Vooren, A. I., and Greidanus, J. H., *Reply to Fettis' Comments on Aerodynamic Coefficients Of an Oscillating Airfoil in Two-Dimensional Subsonic Flow*, Readers' Forum, Journal of the Aeronautical Sciences, Vol. 19, No. 11, p. 790, November 1952. See also Fettis, Henry E., *Regarding the Computation of Unsteady Air Forces by Means of Mathieu Functions*, Readers' Forum, Journal of the Aeronautical Sciences, Vol. 20, No. 6, p. 437, June, 1953. See also Jordan, P. F., *Further Comments on Aerodynamic Coefficients of an Oscillating Airfoil in Two-Dimensional Subsonic Flow*, Readers' Forum, Journal of the Aeronautical Sciences, Vol. 20, No. 5, page 363, May 1953.

[7] Flax, A. H., *Reverse-Flow and Variational Theorems for Lifting Surfaces in Nonstationary Compressible Flow*, Journal of the Aeronautical Sciences, Vol. 20, No. 2, pp. 120–126, February, 1953.

[8] Hofsommer, D. J., Report F61, National Aeronautical Research Institute, Amsterdam, 1951.

[9] McLachlan, N. W., *Theory and Application of Mathieu Functions:* Oxford University Press, Amen House, London, 1947.

An Authorized Binding for Journal of the Aeronautical Sciences

Arrangements have been made by the Institute of the Aeronautical Sciences for members and subscribers to have their Journals bound into distinctively designed books.

Twelve issues, January through December, bound in best grade blue washable buckram, imprinted with your name on cover, cost but $3.45 per volume.

Ship Journals parcel post insured. Within 30 days after receipt, bound volumes will be shipped prepaid in the U.S.A. Full remittance must accompany order.

Publishers' Authorized Bindery Service
(*Binders of all Journals*)

308 West Randolph St. Chicago 6, Ill.

A Vector Method Approach to the Analysis of the Dynamic Lateral Stability of Aircraft

L. STERNFIELD*

Langley Aeronautical Laboratory, NACA

SUMMARY

A description of a vector method approach to the analysis of dynamic stability problems is presented. In addition to supplying information on the damping of the dutch-roll oscillation, the phase relation between roll to yaw, and the amplitude ratio of roll to yaw, the method makes possible an excellent physical visualization of the contribution of the various stability derivatives and mass characteristics to the overall motion of the airplane. The application of the vector method to several problems is briefly discussed.

DISCUSSION

IN THE SPRING OF 1951, two British scientists visited the Langley Laboratory of the NACA, and in the course of reporting on several phases of research related to dynamic stability of aircraft, they mentioned that Dr. K. H. Doetsch, a German scientist now working in Britain, had developed a vector method analysis of dynamic stability problems. Unfortunately, the British representatives were not familiar enough with the method to describe it in detail. Our curiosity about a so-called "vector method" stimulated thought on the problem, which resulted in the development of a method and the design of an analog computer, to be described in this paper. Recently, W. O. Breuhaus, of Cornell Aeronautical Laboratory, visited with Dr. Doetsch and published a paper[1] describing his method. It appears that, in principle, the vector method developed at Langley is similar to Dr. Doetsch's method.

The fundamental principle involved in the method is well known from the solution of linear differential equations with constant coefficients and will be illustrated by considering first a simple spring-mass system and then introducing a dashpot into the system. In Fig. 1 we have a sketch of the spring-mass system and the differential equation describing the system, $m\ddot{x} + kx = 0$, where the two dots signify the second derivative of x with respect to time. One complimentary solution of the differential equation is $x = c_1 \sin \omega t$, where ω is the natural frequency of the system and c_1 is an arbitrary constant. Thus, each term of the differential equation could be plotted as a vector, with the vector moment or force due to displacement along the positive x axis of magnitude k and the vector moment or force due to acceleration 180° out of phase with the displacement of magnitude $m\omega^2$. As indicated in the equation, the sum of the two terms is zero, or the resultant of the two vectors is zero. As shown on the plot, the velocity is 90° out of phase with the displacement.

Fig. 2 shows the case of a dashpot added to the system. The differential equation becomes $m\ddot{x} + d\dot{x} + kx = 0$. One complimentary solution is $x = c_1 e^{at} \sin \omega t$, a damped sinusoidal oscillation, and the expressions for the velocity and acceleration are given on Fig. 2. It should be noted in the analytical expression for the velocity that a phase angle is introduced which is a function of the damping and frequency of the system, $\epsilon = \tan^{-1}(a/\omega)$, and the sine of the angle is directly related to the damping of the system. This phase angle multiplied by a factor of two is also present in the expression for the acceleration. Representing each term of the differential equation as a vector, we have once again the displacement plotted as a vector along the positive x axis of magnitude k, the velocity is $90° + \epsilon$ out of phase with the displacement of magnitude $d\omega_0$, and the acceleration is $180° + 2\epsilon$ out of phase with the displacement of magnitude $m\omega_0^2$. As the equation indicates, the resultant of the three vectors is zero, shown by the dashed vectors on the figure. Thus, the important property of the vector representation of a damped oscillatory system is that the velocity is out of phase with the displacement by 90° plus an angle that is directly proportional to the damping of the system and that the acceleration is out of phase with the displacement by 180° plus twice the same angle.

Now the method is extended to two degrees of freedom. Continuing with our example of mass-spring-dashpot systems, Fig. 3 shows the differential equations of the sketched coupled system with two degrees of freedom in x and y. The solutions for x and y are also given. Of interest in the two degree of freedom case is not only the period and damping of the oscillation but also the phase relation between x and y denoted by the phase angle θ in the solution for y and the amplitude ratio of y to x, the ratio c_2/c_1, where c_1 and c_2 are the coefficients of the solutions in x and y, respectively. The vector plot shown on Fig. 3 indicates how the phase relation between x and y and the amplitude ratio of y to x can be determined from the first equation if the damping, a, and the fre-

Presented at the Aerodynamics Session, Annual Summer Meeting, IAS, Los Angeles, July 15–17, 1953.

* Head, Stability Analysis Section.

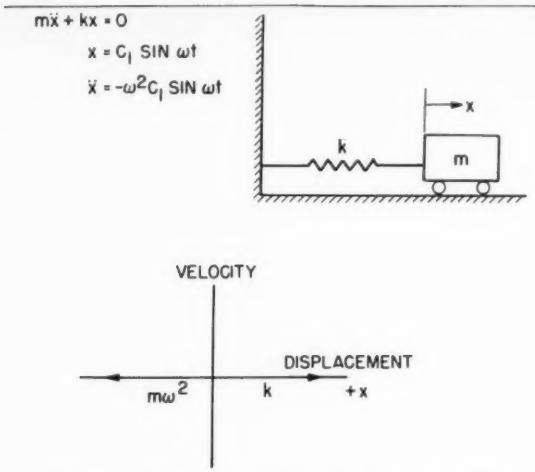

FIG. 1. Vector representation of mass-spring system.

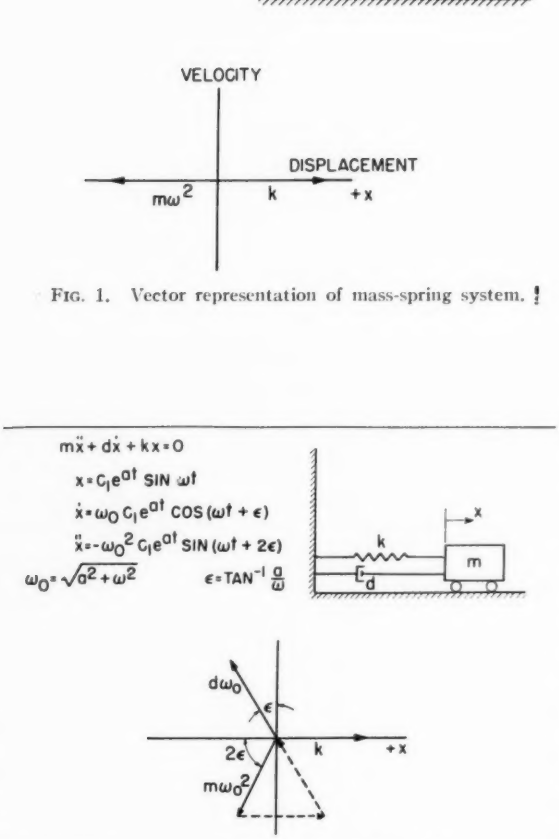

FIG. 2. Vector representation of mass-spring-dashpot system.

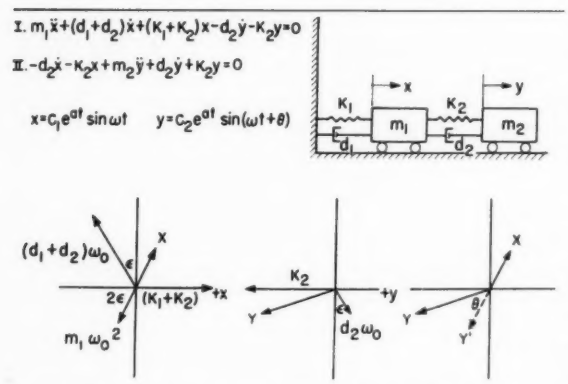

FIG. 3. Determination of the amplitude ratio and phase angle in a two degree of freedom system.

quency, ω, are known. On the left-hand plot, the terms in x are represented. Note $k_1 + k_2$, the displacement vector; $(d_1 + d_2)\omega_0$, the velocity vector that is 90° + the angle ϵ out of phase with the displacement vector; and $m_1\omega_0^2$, the acceleration vector located 180° + 2ϵ out of phase with the displacement. Adding these vectors, we have the resultant vector X. Similarly, on the right-hand plot, the terms in y are plotted on the assumption that the phase angle, θ, is zero—that is, y like x is considered to be positive along the horizontal axis to the right. Also, the amplitude ratio c_2/c_1 is assumed to be unity—that is, the vectors have the magnitude of the constants in the equation, k_2 and d_2, and are not multiplied by the ratio c_2/c_1. Since the right-hand side of the equation is zero, the sum of the two resultant vectors shown on the plot as X and Y must be zero. It is obvious that the condition required for the sum to be zero is that the vectors be diametrically opposite each other and of the same magnitude—that is, Y should assume the position of Y' and be of the same length as Y'. Therefore, the phase angle that was initially assumed to be zero is actually the angle through which Y is rotated to assume the position of Y', and the amplitude ratio, initially assumed to be unity, is the ratio of the resultant vectors Y'/Y.

If only the frequency is known, the damping of the system, as well as the phase relation and amplitude ratio of x to y, can be determined, working with both equations simultaneously. Fig. 4 illustrates the procedure. The equations of motion of the coupled system are shown once again. Initially, we assume that the phase angle between x and y is zero, that the amplitude ratio of y to x is unity, and that the damping angle, ϵ, is zero—that is, the system is assumed to have zero damping. The upper plot on Fig. 4 contains the resultant vectors of X and Y for Eq. (I) and Eq. (II) when $\epsilon = 0$. In both equations, (I) and (II), the sum of the resultants must be zero and the phase and amplitude ratio of Y to X must be the same. Considering only the phase relation between X and Y, it is apparent from the figure that, in order for Y and X to be diametrically opposite each other, Y would have to be rotated in the counterclockwise direction in Eq. (I), whereas in Eq. (II), Y must be rotated in the clockwise direction. Thus one may conclude that the assumption of $\epsilon = 0$, zero damping for the system, is not correct. For the damping angle equal to 2°, $\epsilon = 2°$, the resultant vectors for Eqs. (I) and (II) are plotted on the middle portion of the figure. As in the upper plot, here too, the phase angle required to make the sum of the resultant vectors zero in Eq. (I) is different from the phase angle required to make the sum of the resultant vectors zero in Eq. (II). Thus, $\epsilon = 2°$ does not correspond to the correct damping in the system. For $\epsilon = 4°$, the resultant vectors of Eqs. (I) and (II) are plotted in the lower region of the figure. In this case, rotating Y to Y' about 10° counterclockwise in both equations and also multiplying Y by the same constant, about 0.85,

in both equations would satisfy the condition that the sum of the resultants is zero in each equation. The damping of the system is therefore determined directly from the damping angle, $\epsilon = 4°$, the phase angle between Y and X is about 10°, and the amplitude ratio of Y to X is about 0.85.

In Fig. 4, three discrete values of ϵ were selected to show the variation in magnitude and direction of the resultant vectors as ϵ varies. It appeared possible to design an analog computer or "vector machine" to enable one to introduce a continuous variation of ϵ into the system and note visually the corresponding changes in the magnitude and direction of the resultant vectors. A "vector machine" was designed and built at Langley,* based on the vector method, and was used for the problem of analyzing the lateral stability of an airplane. For the sake of simplicity, the problem involved two degrees of freedom of airplane motion, roll, and yaw, with the assumption that ψ, the angle of yaw, is equal to minus β, the sideslip angle. Fig. 5 shows the nondimensional linearized equations of motion used in the analysis. For several airplanes investigated, the results obtained from the two degree of freedom analysis on the damping of the dutch-roll oscillation, the phase angle between roll and yaw, and the amplitude ratio of roll to yaw were in very good agreement with the results obtained from a three degree of freedom analysis if, when using only two equations of motion, the values of C_{n_p} and C_{n_r} inserted in the yaw equation are determined from the expressions shown on the figure. The undamped natural frequency of the system is well approximated by the expression given on the figure, where $(C_{n_p})_A$ and $(C_{n_r})_A$ are the airplane's values. A detailed description of the machine is given in the Appendix.

* Particular thanks are due F. S. Malvestuto, Jr., who assisted in the design of the machine, and P. R. Thomas and I. B. Bloxom, of the 7- by 10-ft. Tunnels Shop, for the excellent job they did in constructing the machine.

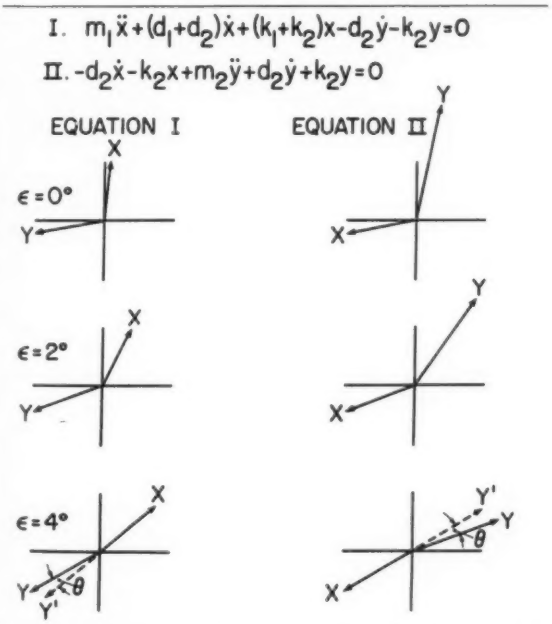

FIG. 4. Determination of the damping, amplitude ratio, and phase angle in a two degree of freedom system.

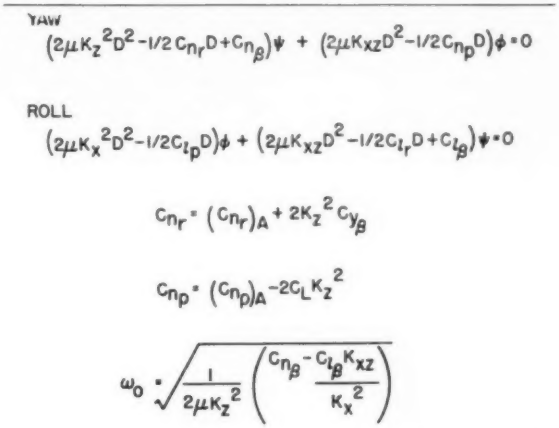

FIG. 5. An approximate form of the nondimensionalized lateral equations of motion assuming $\psi = -\beta$.

Application of the Vector Method to Several Other Problems.—As noted in the Appendix, the vector method makes possible the physical visualization of the contribution of the stability derivatives to the damping of the dutch-roll oscillation. If, therefore, an airplane requires additional damping, which may be introduced through artificial damping devices, this property of the method enables the selection of the most effective type of auxiliary damper where a perfect damper is assumed—that is, a damper without any lag.

The vector method may also be applied to the problem of determining the stability derivatives of an air-

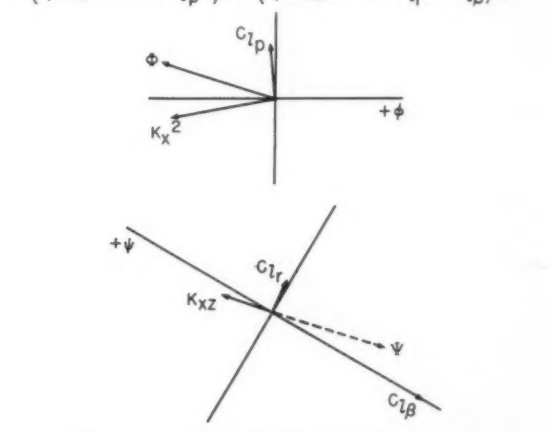

FIG. 6. Determination of the derivatives C_{l_r} and C_{l_β} from flight tests.

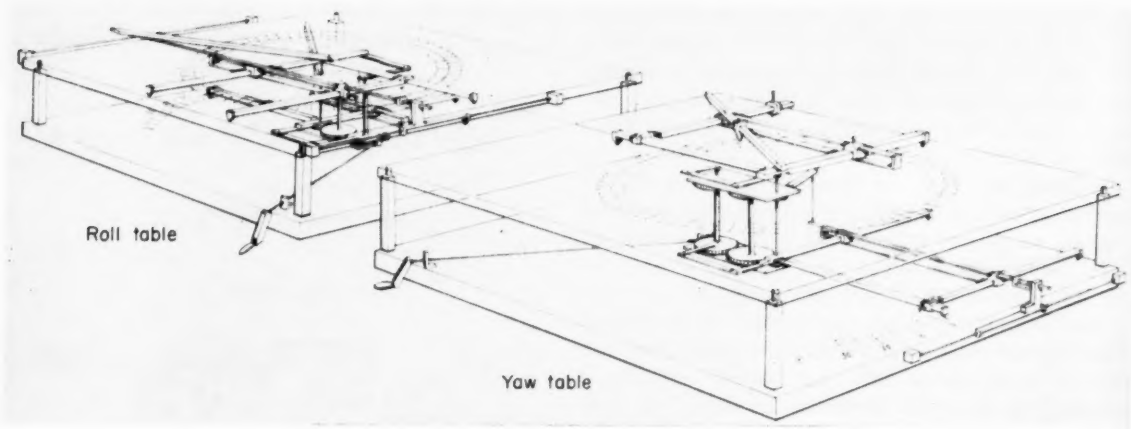

FIG. 7. A schematic sketch of the "vector machine."

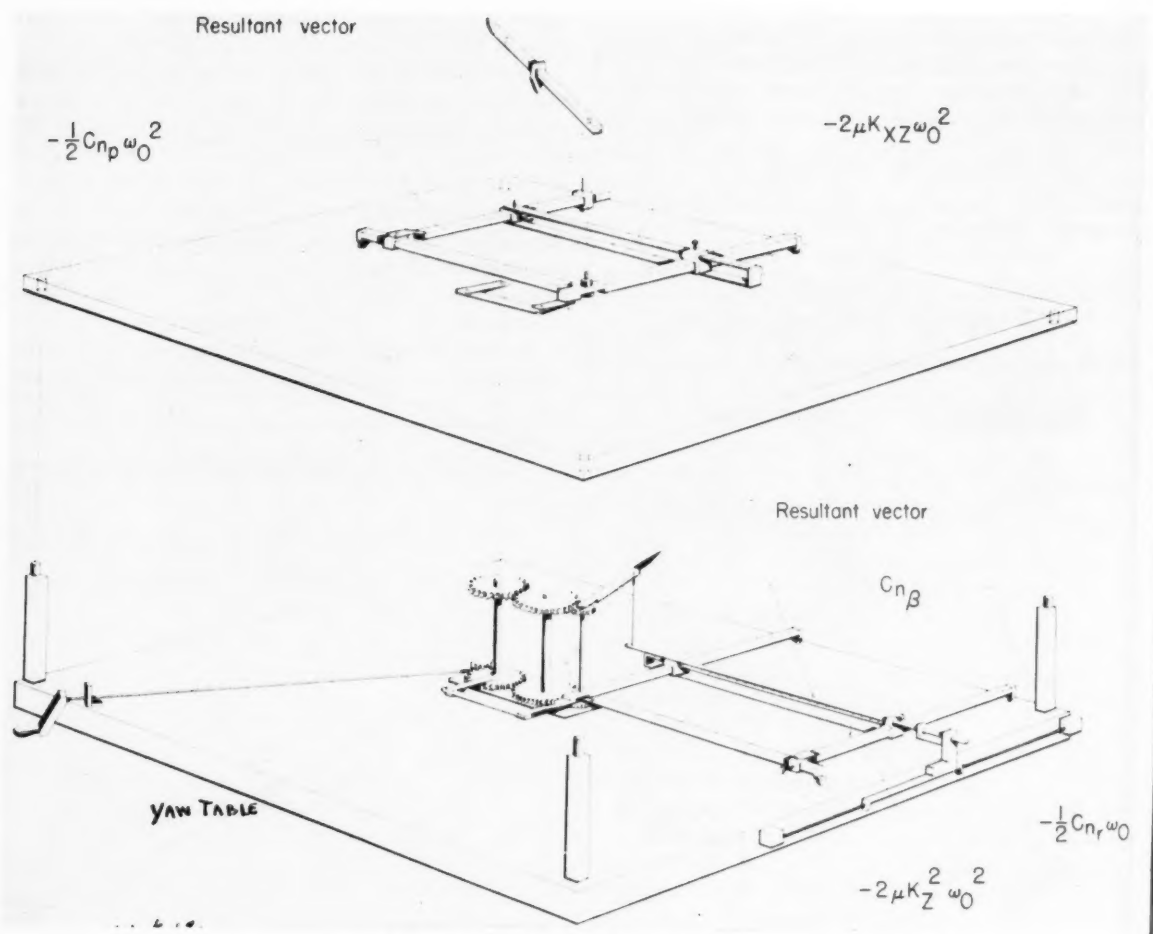

FIG. 8. An exploded view of the yaw table.

plane if the mass characteristics, as well as the period, damping, phase relation, and amplitude ratio, are available from flight tests of the airplane. Fig. 6 illustrates the approach to this problem. The roll equation is selected as an example. Since the three stability derivatives, C_{l_p}, C_{l_r}, and C_{l_β} are not known and only two conditions are known—namely, the phase between roll and yaw and the amplitude ratio of roll to yaw—it is impossible to uniquely determine the three derivatives. However, if one of the derivatives is estimated, the other two are uniquely determined. Assuming that C_{l_p} is estimated, the vectors corresponding to C_{l_p} and K_z^2 are easily plotted. Since ψ is out of phase with ϕ by a known angle, the coordinate system for representation of the ψ terms is rotated through this phase angle as indicated on the figure. The K_{xz} vector multiplied by the amplitude ratio ψ/ϕ and the resultant ψ vector required to satisfy the equation are plotted on the rotated coordinate system. The direction of the C_{l_r} and C_{l_β} vectors is known, and therefore the magnitudes are uniquely determined so that the sum of the three vectors, K_{xz}, C_{l_r}, and C_{l_β}, multiplied by the amplitude ratio ψ/ϕ, gives the dashed resultant vector. The problem as to which one of the derivatives should be estimated in order to obtain the most accurate determination of the other two derivatives requires additional research.

Another application of the vector method arises in automatic stabilization problems, where it is generally necessary to know the frequency response of the system. Through use of the vector machine, data required to calculate frequency responses may be obtained with ease and rapidity. A change in frequency is introduced by simply changing the lengths of the vectors. The phase angles and amplitude ratios for each degree of freedom, read directly from the vector machine, are the data needed to compute the frequency response of the system.

Appendix

A schematic sketch of the mechanical analog machine designed and constructed at Langley is shown in Fig. 7. The analog machine consists of two tables with two decks on each one of the tables. On the yaw table, the lower deck represents the yawing moment due to angular displacement, velocity, and acceleration in yaw, and the upper deck represents the yawing moment due

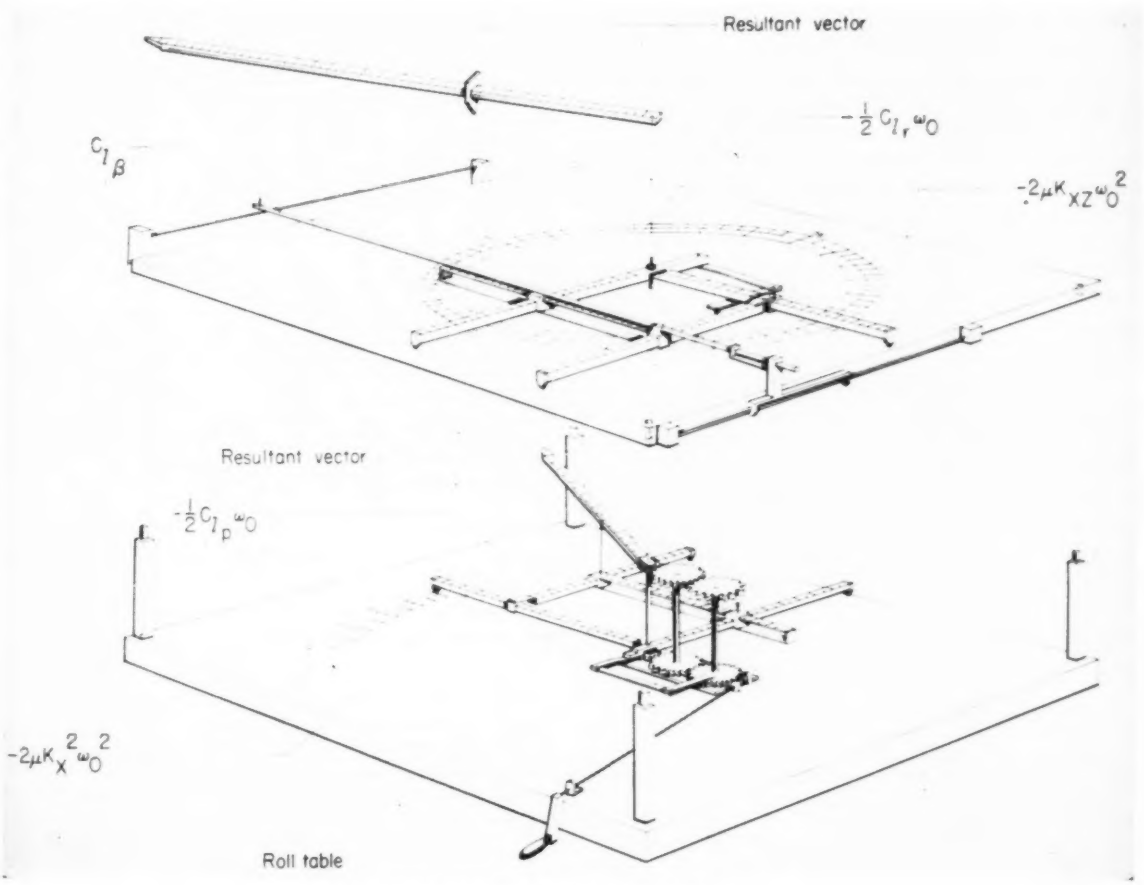

Fig. 9. An exploded view of the roll table.

to rolling velocity and rolling acceleration. On the roll table, the lower deck represents the rolling moment due to rolling velocity and rolling acceleration, and the upper deck represents the rolling moment due to angular displacement, velocity, and acceleration in yaw.

The exploded view of the yaw table is shown in Fig. 8 and corresponds to the case of zero damping of the dutch-roll oscillation—that is, the vector moments due to velocity and acceleration are 90° and 180°, respectively, out of phase with the vector moment due to displacement. The vector moments corresponding to the stability derivatives and mass characteristics are represented by metal rods. On the lower deck, one horizontal rod corresponds to the directional stability derivative, C_{n_β}, whereas the other horizontal rod corresponds to the moment of inertia in yaw, $-2\mu K_z{}^2\omega_0{}^2$. The rod normal to C_{n_β} and $-2\mu K_z{}^2\omega_0{}^2$ is the damping-in yaw derivative, $-(1/2)C_{n_r}\omega_0$. The vector attached to the C_{n_β} arm through the vertical pin is the resultant of the three vectors. This pin moves in a groove cut into the resultant vector. Each one of these arms is scaled in tenths of inches so that values of the derivatives and inertia characteristics may be set accurately through thumbscrews. The magnitude of the resultant vector is the value shown on its scale at the point of intersection of the vertical pin with the resultant vector.

The vectors $-(1/2)C_{n_r}\omega_0$ and $-2\mu K_z{}^2\omega_0{}^2$ are geared in a manner to cause the acceleration vector $-2\mu K_z{}^2\omega_0{}^2$ to rotate through twice the angle through which the vertical vector $-(1/2)C_{n_r}\omega_0$ rotates. Rotation of the vectors is performed by rotating the shaft. The angular rotation of the shaft causes the vectors to assume a particular position relative to each other corresponding to a system with a specific amount of damping of the dutch-roll oscillation. The displacement vector C_{n_β} is not affected by the shaft rotation but always lies in a horizontal position.

The upper deck of the yaw table is made of lucite. On this deck, the vertical arm corresponds to the cross-coupling derivative $-(1/2)C_{n_p}\omega_0$, and the horizontal arm is the product of inertia term $-2\mu K_{xz}\omega_0{}^2$. The resultant of these two vectors is easily placed into position and rests on the small protruding pin that fits into the hollowed groove of the resultant vector and moves within the groove as the arms rotate. The angular motion of the vectors is geared in a two to one ratio—the acceleration vector $-2\mu K_{xz}\omega_0{}^2$ rotating through twice the angle of the velocity vector $-(1/2)C_{n_p}\omega_0$. One set of gears controls the rotation of the vectors on the table. As the vectors rotate, the magnitude and direction of the resultant vector changes and the angular rotation of the resultant is read on a fine angular scale engraved on the lucite.

Since the derivative C_{n_p} and the product of inertia factor K_{xz} may, for presently designed aircraft, have either positive or negative signs, this deck was so designed that the two arms can be located in any one of the four quadrants. As they are presently set, they correspond to negative values of C_{n_p} and K_{xz}. If K_{xz} were positive, the horizontal arm would be shifted 180° to its present position. Similarly, if C_{n_p} were positive, the vertical arm would be shifted 180°.

The roll table was designed and constructed similar to the yaw table just described. An exploded view of the roll table is shown in Fig. 9. On this table, the lower deck contains the metal rods corresponding to the damping-in-roll derivative $-(1/2)C_{l_p}\omega_0$ and the moment of inertia in roll $-2\mu K_x{}^2\omega_0{}^2$ and their resultant vector. The metal rods on the upper deck correspond to the effective dihedral derivative C_{l_β}, the cross-coupling derivative $-(1/2)C_{l_r}\omega_0$, the product of inertia term $-2\mu K_{xz}\omega_0{}^2$, and their resultant vector. Here again, one set of gears controls the rotation of all the vectors on the table.

The solution of a problem for a specific airplane requires working with both equations simultaneously The undamped natural frequency of the system ω_0 is approximated by the expression presented in Fig. 5. The solution obtained is the damping of the dutch-roll oscillation, the phase angle between roll and yaw, and the amplitude ratio of roll to yaw. The damping is determined from the angle through which either the velocity vector must be rotated or half the angle through which the acceleration vector must be rotated in order that the phase angle between the resultant vector on the yaw table is the same as the phase angle between the resultant vectors on the roll table. Also, the amplitude ratio of the resultant vectors on one table must be the same as the amplitude ratio of the resultant vectors on the other table.

Reference

[1] Breuhaus, W. O., *Résumé of the Time Vector Method as a Means for Analyzing Aircraft Stability Problems*, WADC Tech. Rep. 52-299, November, 1952.

Results of Some Base Pressure Experiments at Intermediate Reynolds Numbers with $M = 2.84$*

L. L. KAVANAU†

University of California at Berkeley

ABSTRACT

Base pressure data are presented for a cone-cylinder model at Mach Number 2.84 and Reynolds Numbers from 45,000 to 400,000. These data verify the maximum in base pressure coefficient (p_b/p) predicted by Crocco and Lees which occurs between the completely laminar and turbulent flow régimes. Sting length requirements for this model are summarized reflecting the growth of the critical wake region with decreasing Reynolds Number. Results from varying the base pressure orifice location and sting diameter are also given.

INTRODUCTION

THE COMPLEX FLOW MECHANISM in the wake which determines the base pressure has been the subject of analysis by Crocco and Lees[1] for the case of a two-dimensional airfoil with a blunt trailing edge. Their analysis qualitatively describes the various effects of Reynolds Number (based on total length and noted as Re_L) on the base pressure coefficient (ratio of measured base pressure to free-stream static pressure and noted as p_b/p). The analysis predicts a maximum of the base pressure coefficient at a Reynolds Number intermediate to a completely laminar and completely turbulent flow. This maximum results from transition occurring in the wake region immediately behind the base. Assuming that the base pressure for a blunt-based axisymmetric model responds to changes in Reynolds Number in the same qualitative manner as the two-dimensional airfoil considered by Crocco and Lees, the maximum base pressure coefficient should provide the approximate upper bound in Reynolds Number for the completely laminar flow range.

No experimental data are available which give direct verification of the predicted maximum in base pressure coefficient. Bogdonoff[2] has reported the effect of Reynolds Numbers between 0.7×10^6 and 17.6×10^6 on the base pressure of a representative body of revolution at Mach Number 2.95. His data at the lowest Reynolds Number show the base pressure coefficient increasing sharply with decreasing Reynolds Number. Preliminary experiments at Berkeley with similar models and Mach Number at Reynolds Numbers near 1,000 have shown decreasing coefficients with decreasing Reynolds Number.

In order to obtain experimental data through this transition region, a series of tests at intermediate Reynolds Numbers was performed utilizing the supersonic wind tunnel at the University of California at Los Angeles (U.C.L.A.). It is the purpose of this paper to report the results of these tests.

TEST OBJECTIVES

The major experimental objectives of these tests were to determine the effect of Reynolds Number over

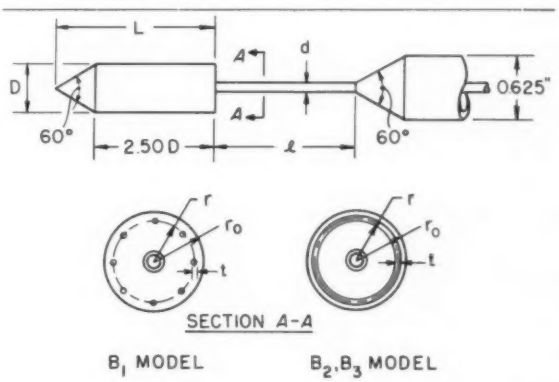

MODEL	L (INCHES)	d/D	t/D	r/r_o
B_1	2.020	0.233	0.050	0.90, 0.70, 0.50, 0.30
		0.177	0.225	0.90, 0.70, 0.50, 0.30
B_2	1.010	0.233	0.050	0.90, 0.70, 0.50, 0.28
		0.177	0.050	0.90, 0.70, 0.50, 0.22
B_3	0.578	0.233	0.058	0.75, 0.51

FIG. 1. Base pressure models—dimensional information.

Received November 6, 1953.

* This investigation was carried out by the Department of Engineering at the University of California, Berkeley, under joint sponsorship of the Office of Naval Research (USN) and the Office of Scientific Research (USAF). The author would like to express his appreciation to Dean L. M. K. Boelter of the College of Engineering, University of California at Los Angeles, for the use of the facilities and to W. F. MacInnes for his assistance in preparing and performing these experiments.

† Research Engineer, Department of Engineering.

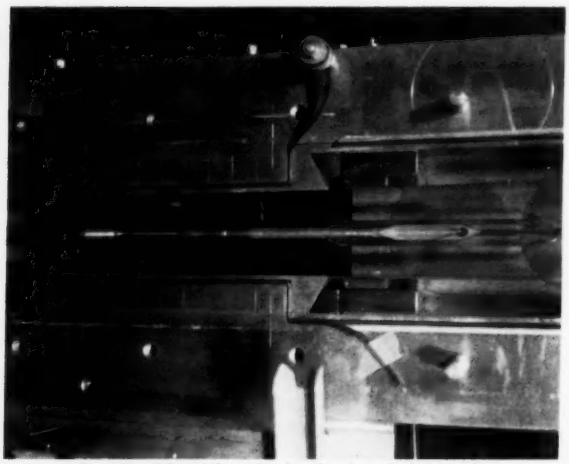

FIG. 2. Model installation in the wind tunnel.

the range 45,000 to 400,000 on the base pressure of a particular aerodynamic configuration.

It was, of course, necessary that final results be void of all aerodynamic interferences. For most supersonic wind-tunnel experiments upon a fore-body of revolution without boat-tail, interferences are eliminated by preventing the model bow wave reflection off the tunnel boundaries from interacting with the model and by supporting the model from the rear by a sting. Experiments concerned with the base region of the model require that further attention be given to the influence of the supporting sting on the flow in this region. Studies of some such influences have been reported by Perkins[3] and Chapman[4] for Reynolds Numbers greater than about 0.4×10^6. Significant changes in the wake flow were anticipated for the intermediate Reynolds Number range of these tests. Therefore, it was desirable to include a limited study of the influence of sting length and sting diameter on the base pressure.

A further test objective was to study the uniformity of the base pressure distribution. Preliminary data obtained at Berkeley for models in completely laminar flow indicate large radial variations of pressure. Experiments appearing in the literature for models with turbulent wakes or boundary layers have not included investigations of this problem, and the base pressure has been taken to be uniform.[1, 2, 3, 4] It was possible that appreciable nonuniformities might occur in the base pressure distribution for the intermediate Reynolds Number range of this experiment.

WIND TUNNEL

The U.C.L.A. 3- by 3-in. supersonic wind tunnel[5] is the open-circuit type and operates continuously with atmospheric stagnation pressure. It is powered by two 60-hp. reciprocating Chicago Pneumatic vacuum pumps in parallel evacuating a reservoir downstream of the diffuser section. By introducing a stagnation regulating valve, the free-stream Reynolds Number was made variable from 78,000 to 205,000 per in. with a nominal Mach Number of 2.84.

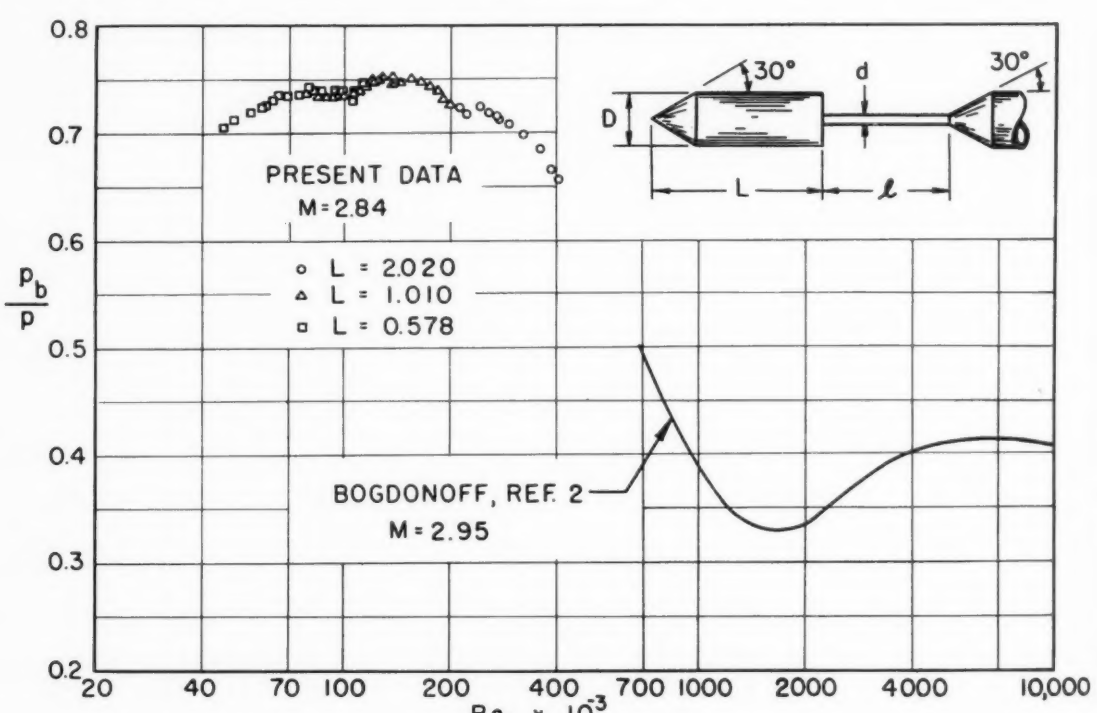

FIG. 3. The variation of base pressure coefficient with Reynolds Number.

The nozzle performance over this extended range of operation was studied through impact tube surveys. These surveys succeeded in identifying a usable test rhombus with a maximum Mach Number variation of ±0.02. For the purposes of this paper, the nozzle was assumed isentropic, and the Mach Numbers and static pressures were determined by impact and stagnation pressures. It is worth noting here that this assumption may not be too inaccurate in view of the comparison of present data with Bogdonoff's results for similar models as shown in Fig. 3. The ordinate is extremely sensitive to free-stream static pressure p by definition and to free-stream Mach Number M through its influence on the base pressure p_b.[1, 4] The nozzle calibration for atmospheric stagnation pressure is given in reference 6.

Models

The models tested were geometrically similar to models used by Bogdonoff—i.e., 60° apex angle right circular cones with cylindrical afterbodies 2.50 cal. long. All models were fabricated from combinations of aluminum and brass and were slightly polished to approximately a 25-microin. finish. Three basic model sizes were used with various radial locations of the base pressure sampling orifices and sting diameters.

A control was provided for adjusting the effective sting length. This control was accomplished by moving a coaxial 60° apex angle cone-cylinder along the sting to the desired location. When placed at the base of the model, this disturbance cone provided mechanical support for the model during starting and stopping of the tunnel.

Fig. 1 is a schematic drawing of the model configuration and a listing of pertinent dimensions for the three models tested. Fig. 2 is a photograph of a typical model and support installation in the tunnel.

Special Instrumentation

Model base pressures were measured by means of a precision oil manometer,[7] and the wind-tunnel stagnation pressure was measured by means of a mercury micromanometer. Both manometers were referenced to a partial vacuum of approximately 9 microns (0.009 mm. Hg). A coincident beam schlieren system was used for flow visualization.

Experimental Results

Base pressure coefficients for a cone-cylinder model at $M = 2.84$ were obtained for Reynolds Numbers from 45,000 to 400,000. The final results for dry air are shown in Fig. 3. A curve indicating some of Bogdonoff's results at higher Reynolds Numbers is incorporated for comparison.

The effect on the base pressure of varying the sting length at constant Mach and Reynolds Numbers for a typical run is reproduced in Fig. 4. The accumulation of all such data is presented in Fig. 5 as the critical sting length in calibers plotted versus Reynolds Number. The critical sting length is defined as the minimum sting length possible for obtaining a base pressure within 0.5 per cent of that obtained with an "infinite" length sting.

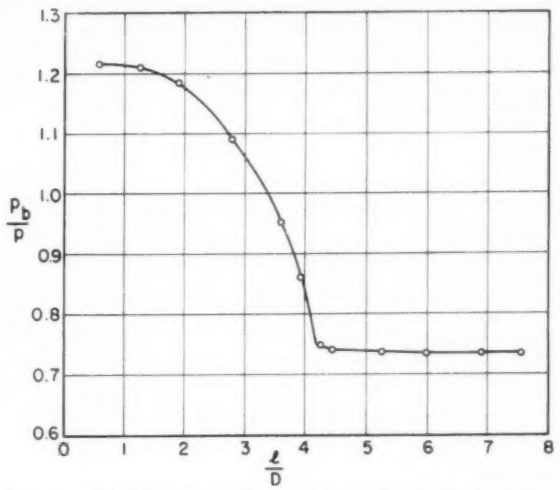

Fig. 4. Typical effect of variable sting length on the base pressure coefficient at constant Reynolds Number.

Results from tests of the two sting diameters and various orifice locations indicated no significant influence of these variables on the base pressure coefficient over the Reynolds Number range tested. All data were within ±0.7 per cent of the reported values.

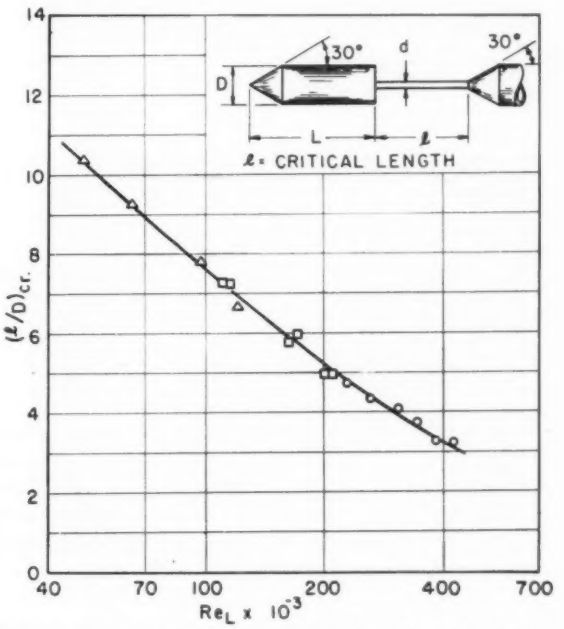

Fig. 5. Effect of Reynolds Number on the critical sting length.

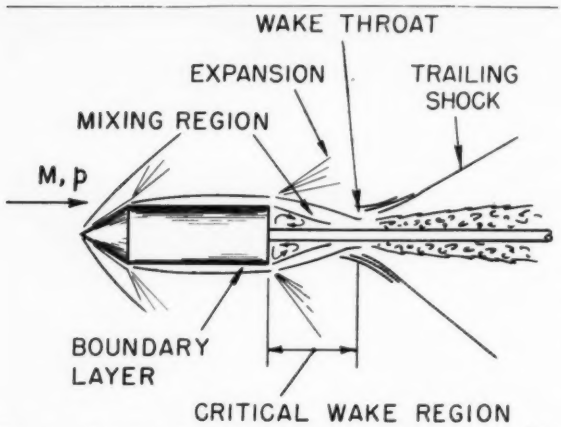

FIG. 6. Exaggerated sketch of flow over axisymmetric model.

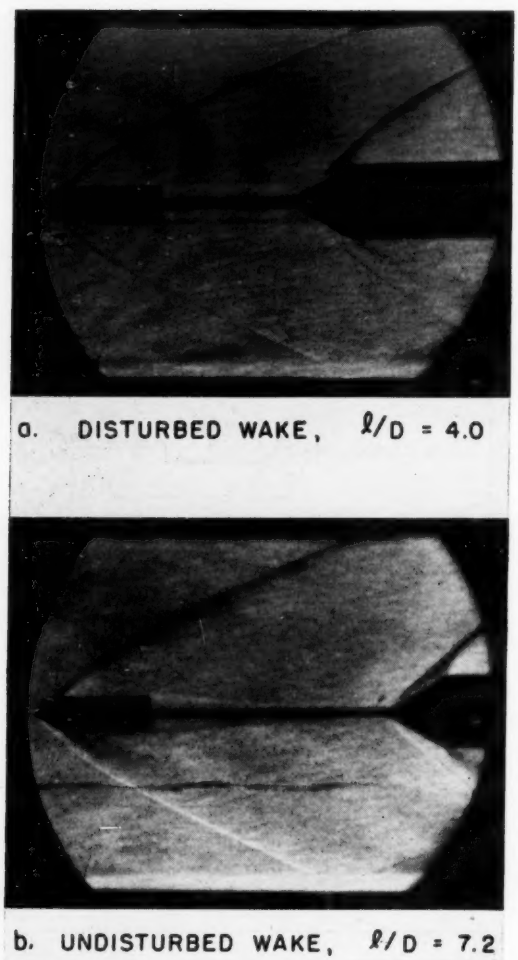

FIG. 7 Schlieren photographs illustrating the effect of sting length on the critical wake region at Re_L = 112,000.

DISCUSSION

The existence of a maximum in the base pressure coefficient as predicted by Crocco and Lees was verified as seen in Fig. 3. Their analysis attributes this maximum mainly to the variation with Reynolds Number of the mixing rate between the outside nearly isentropic stream and the critical wake region (see Fig. 6) immediately aft of the base. This change in the mixing rate is due to the transition moving into the critical wake region from downstream of the wake throat as the Reynolds Number increases from the completely laminar flow range.

Crocco and Lees describe the action of the wake throat or "critical point" in isolating the critical wake region from influences farther downstream. This wake throat was present with the sting-supported models of these tests,* and its changing position with Reynolds Numbers significantly influenced the sting length requirements as shown in Fig. 5. It is seen that the critical sting length increases with decreasing Reynolds Numbers.

Fig. 7 presents two schlieren photographs of one model illustrating the critical wake region in a disturbed and undisturbed state.

Consideration has been given to testing two-dimensional models in this intermediate range of Reynolds Numbers where the critical wake region is so extensive. These models would almost certainly have to incorporate unique devices such as fences extending from the model leading edge downstream past the wake throat or some system of tunnel boundary-layer control in order to keep the turbulent fluctuations in the tunnel-wall boundary layer from disturbing the critical wake region. Unless such precautions are taken, the critical wake region, under conditions of decreasing Reynolds Number, will not become free of turbulence as it would in the free-flight sense described by Crocco and Lees. This would result in excessively high base pressures and would prevent the drop in base pressure coefficient which is characteristic only of the completely laminar model at these Reynolds Numbers.[1]

CONCLUSIONS

(1) Base pressure data have been obtained for a cone-cylinder model at Mach Number 2.84 and Reynolds Numbers from 45,000 to 400,000. A maximum base pressure coefficient (p_b/p) of 0.75 occurs at a Reynolds Number (Re_L) of 140,000. The occurrence of such a maximum is in accord with the qualitative theory presented by Crocco and Lees.[1]

(2) Variation in size of the critical wake region results in significant increases of the critical sting length

* It should be noted that this phenomenon has been previously observed by experimenters at higher Reynolds Numbers than those of these tests, as well as in the preliminary experiments at Berkeley in the laminar flow region.

(*Continued on page 274*)

The Flow over a Flat Plate with a Small Angle of Attack at Mach Number 1

GOTTFRIED GUDERLEY*

WADC, Wright-Patterson Air Force Base

Abstract

The pressure distribution over a flat plate at Mach Number 1 is determined with the usual transonic approximations. At the suction side of the plate, a cavitation region will arise close to the leading edge; the influence of this region on the flow field can be disregarded if the angle of attack is small enough. The pressure distribution on the pressure side is obtained as a relatively simple closed expression; on the suction side the pressure distribution is found by the method of characteristics, but it can be approximated by a similarly simple analytical expression.

Introduction

The present paper determines the pressure distribution over a flat plate in two-dimensional flow with a free-stream Mach Number 1. The only other unsymmetric flow field that has been determined up to the present is the flow over a wedge with an angle of attack that is small in comparison with the wedge angle.[2] The present problem can be considered as the extreme in which the angle of attack is large in comparison with the opening angle of the wedge. The flow around the nose of the profile causes, in either example, a supersonic region to arise at the suction side of the profile. In the case of the wedge with a small angle of attack, the effect of this local region on the lift can, however, be neglected; in the present case of a flat plate, the supersonic region extends over the whole profile. In this regard the present problem shows a phenomenon that did not occur in previous examples of transonic flow patterns.

The method by which the solution will be found is not quite systematic. Certain properties of the solution can be seen from the particular solutions discussed in reference 1. The expression for the stream function is then found by an attempt to construct a simple expression that has these properties. However, these properties are not sufficient to determine such an expression uniquely, so this solution must be verified. The advantage of this procedure is the simplicity of the result. Previously, the author has carried out a more direct approach, which was successful; however, the computations were very cumbersome, were less accurate, and did not reveal the simple properties of the solution.

Received October 5, 1953.

* Aeronautical Research Laboratory.

(1) The Boundary Value Problem

Fig. 1 shows the flow over an inclined plate at Mach 1. From the leading and the trailing edges, sonic lines extend to infinity. At either edge one has a Meyer expansion. The Meyer expansion at the trailing edge occurs because a supersonic pressure prevails at the upper side of the plate. Close to the leading edge one finds a stagnation point. Stream lines that lie above the stagnation stream line "spill over" the leading edge. The flow over the sharp leading edge that thus arises, is accomplished by a Meyer expansion.

Among the waves of the Meyer expansion there is one in each case, the so-called limiting Mach wave, which separates the Mach waves that reach the sonic line from those that do not reach it. For the subsonic part of the flow field, only those portions of the supersonic region which lie upstream of the limiting Mach wave are of importance.

By the Meyer expansion at the leading edge, an extremely low pressure (neglecting the boundary layer, even a vacuum) is reached; the stream lines separate from the surface, even if no boundary layer is admitted. Behind this low pressure region one has a rapid recompression and a flow reattachment.

It is practically impossible to prescribe here a realistic boundary condition. Fortunately, this boundary condition is unessential for small angles of attack. Details will be found later.

The hodograph formulation of the problem is shown in Fig. 2. Corresponding points in Figs. 1 and 2 have the same notation. All stream lines start at point 0, which corresponds to the free-stream velocity. The lower side of the plate maps into the straight line DCB. Point D corresponds to the leading edge; point C, to the stagnation point; point B, to the trailing edge. The figure shows also a few stream lines, in particular the one that runs to the stagnation point Stream lines that lie in the vicinity of the stagnation stream line will, in their further course, run along the side of the plate. Those that lie below the stagnation stream line will follow the portion CB; those above the stagnation stream line will run along CD. Thus they will have practically a reversed flow direction, and only later will they turn back into the original direction. The limiting Mach waves are represented by the characteristics E0 and A0.

In this boundary value problem, simplifications that arise for small angles of attack may be carried out For the important part of the flow field, this process introduces the so-called transonic simplifications of the hodograph equation.

Let w and θ be polar coordinates in the hodograph plane, and let w^* denote the sonic velocity. γ may be the ratio of the specific heats. We introduce a new independent variable η defined by

$$\eta = [(w - w^*)/w^*] (\gamma + 1)^{1/2} \tag{1}$$

Usually the transonic simplifications are obtained, by introducing

$$\bar{\eta} = \eta/t \tag{2a}$$

$$\bar{\theta} = \theta/t^{3/2} \tag{2b}$$

where t is a parameter. The hodograph equation is then simplified by retaining only the lowest powers in t. Thus Eq. (4) (see next section) will result. In the present example the quantity t has a geometrical significance—viz., one can set

$$t = \theta_0^{2/3} \tag{3}$$

where θ_0 is the angle of attack. Small values of t will then correspond to small angles of attack. The slope of the plate will then be given by $\bar{\theta} = -1$. As θ_0 tends to zero, the portion DE of the boundary will move to infinity in the $\bar{\eta}$, $\bar{\theta}$-plane. The characteristics are then semicubic parabola.

This hodograph filed is shown in Fig. 3. The origin of the $\bar{\eta}$, $\bar{\theta}$-system is shifted to point B. Then the free-stream velocity will lie at $\bar{\theta} = 1$. Along ABC one has

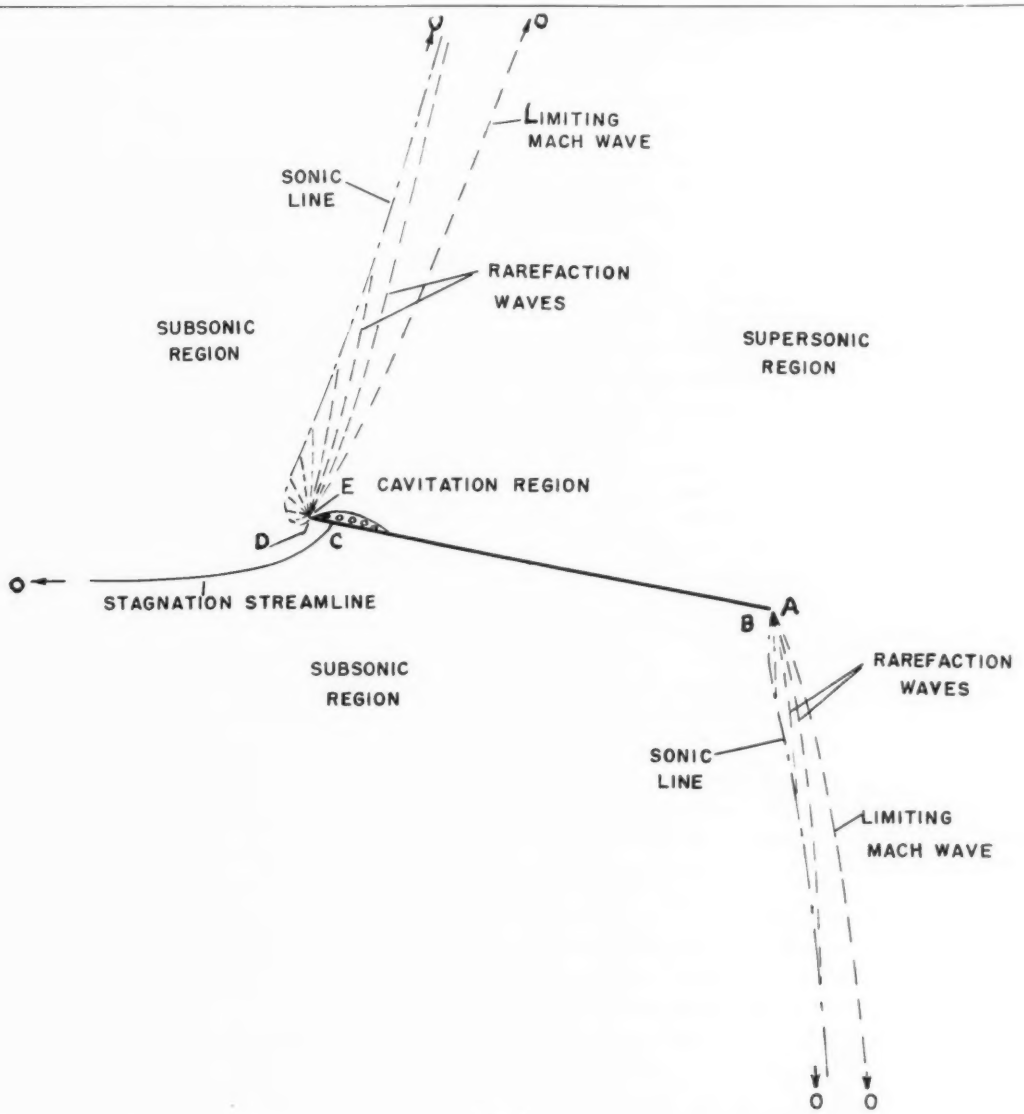

FIG. 1.

the boundary condition $\psi = 0$. At infinity, a condition must be derived from the original requirement that $\psi = 0$ along CDE. The reader will suspect that, because of the limiting process that this line moves to infinity, the exact shape of this line—i.e., the exact boundary condition prescribed in the cavitation region—will be unimportant. This is a significant simplification brought about by the assumption that the angle of attack is small. The requirement that at zero velocity there must be a branch point of the stream lines is, however, essential, and it is not automatically fulfilled. How this condition expresses itself in the limiting case of small values of the angle of attack θ_0 will be shown after suitable particular solutions have been introduced.

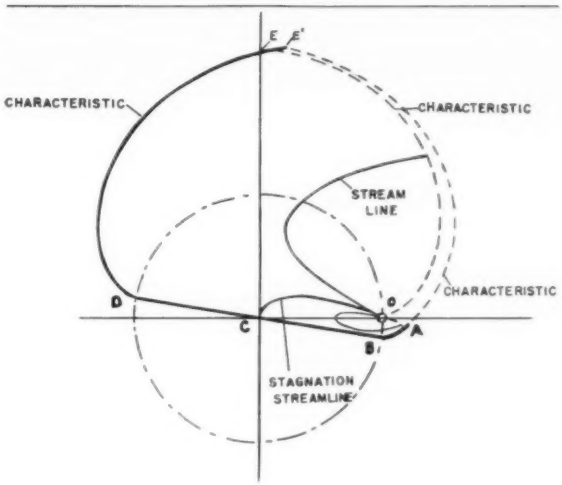

FIG. 2.

(2) PARTICULAR SOLUTIONS FOR ψ

The limiting process that θ_0 tends to zero leads to the following simplified hodograph equation

$$\psi_{\bar\eta\bar\eta} - \bar\eta\psi_{\bar\theta\bar\theta} = 0 \tag{4}$$

Here ψ is the stream function. For the following we need certain the particular solutions that have been studied in detail in reference 1. Introducing in Eq. (4) new variables,

$$\rho = -\bar\eta^3 + (9/4)\bar\theta^2 \tag{5a}$$

$$\xi = \bar\eta/[(3/2)\bar\theta]^{2/3} \tag{5b}$$

(see Fig. 4), one is led to the differential equation

$$\frac{(1-\xi^3)^2}{\xi}\psi_{\xi\xi} - \frac{5}{2}\xi(1-\xi^3)\psi_\xi = 9\rho^2\psi_{\rho\rho} + \frac{21}{2}\rho\psi_\rho \tag{6}$$

Particular solutions of this differential equation are found by the hypothesis

$$\psi = \rho^{-(1/12)+(1/3)\sqrt{\lambda}}G(\xi) \tag{7}$$

where λ is an arbitrary parameter. The function G can be expressed by hypergeometric series (see reference 1). Naturally G depends also upon λ; therefore the notation $G(\xi, \lambda)$ will be used occasionally. Furthermore one has for each value of λ two linearly independent solutions G. They may be denoted by G^a and G^s, the superscripts a and s indicating that the corresponding solutions are antisymmetric or symmetric with respect to the line $\bar\theta = 0$ ($\xi = -\infty$). Formulas for the G^a and G^s are found in Eqs. (18) and (19) of reference 1.

We now proceed to determine the particular solutions (7) which will be utilized for the representation of the solutions ψ in different regions of the $\bar\eta, \bar\theta$-plane. In Fig. 3, the line $\rho = 9/4$—that is, the line $\rho =$ const. which runs through point 0—has been drawn. The regions for which $\rho < 9/4$ and $\rho > 9/4$ will be denoted as inner or outer region, respectively.

In the vicinity of point B, the solution is subject to the boundary condition $\psi = 0$ along AB and along BC. Because of the condition along BC, the solution is antisymmetric with respect to $\xi = -\infty$. In the vicinity of the line AB (that is, $\xi = 1$), the arising expression is then represented by

$$\psi = \rho^{-(1/12)+(\sqrt{\lambda}/3)}\cdot\Gamma\left(\frac{1}{2}\right)\left\{\frac{\Gamma\left(\frac{2}{3}\sqrt{\lambda}\right)\cdot\sin\pi\left(\frac{1}{3}\sqrt{\lambda}+\frac{1}{4}\right)}{\Gamma\left(\frac{\sqrt{\lambda}}{3}+\frac{11}{12}\right)\cdot\Gamma\left(\frac{\sqrt{\lambda}}{3}+\frac{7}{12}\right)}(1-\xi^3)^{-(\sqrt{\lambda}/3)+(1/12)} + \frac{\Gamma\left(-\frac{2}{3}\sqrt{\lambda}\right)\cdot\sin\pi\left(-\frac{1}{3}\sqrt{\lambda}+\frac{1}{4}\right)}{\Gamma\left(-\frac{\sqrt{\lambda}}{3}+\frac{11}{12}\right)\cdot\Gamma\left(-\frac{\sqrt{\lambda}}{3}+\frac{7}{12}\right)}(1-\xi^3)^{(\sqrt{\lambda}/3)+(1/12)}\right\}$$

[see Eq. (18d) of reference 1; for $1-\xi \ll 1$ the hypergeometric functions occurring in this equation can be replaced by 1]. A form more suitable for discussion is obtained if we insert here the definition for ρ [Eq. (5a)],

$$\psi = \left(\frac{\eta}{\xi}\right)^{-(1/4)+\sqrt{\lambda}} \cdot \Gamma\left(\frac{1}{2}\right) \left[\frac{\Gamma\left(\frac{2}{3}\sqrt{\lambda}\right) \sin \pi \left(\frac{1}{3}\sqrt{\lambda} + \frac{1}{4}\right)}{\Gamma\left(\frac{\sqrt{\lambda}}{3} + \frac{11}{12}\right) \cdot \Gamma\left(\frac{\sqrt{\lambda}}{3} + \frac{7}{12}\right)} + \right.$$

$$\left. \frac{\Gamma\left(-\frac{2}{3}\sqrt{\lambda}\right) \cdot \sin \pi \left(-\frac{\sqrt{\lambda}}{3} + \frac{1}{4}\right)}{\Gamma\left(-\frac{\sqrt{\lambda}}{3} + \frac{11}{12}\right) \cdot \Gamma\left(-\frac{\sqrt{\lambda}}{3} + \frac{7}{12}\right)} (1 - \xi^3)^{(2/3)\sqrt{\lambda}} \right] \quad (8)$$

Here $\sqrt{\lambda}$ can assume either sign. The condition $\psi = 0$ along AB requires that the first term of the bracket be zero. Besides, the exponent of the term η/ξ in front must be positive, otherwise point A (the trailing edge) would not map into the finite part of the physical plane.

Thus one finds as possible values of $\sqrt{\lambda}$ in the vicinity of point B

$$\sqrt{\lambda} = [(9/4) + 3h] \qquad (h = 0,1,2 \ldots) \qquad (9)$$

i.e., the desired function will be represented by a superposition of the particular solutions

$$\psi = \rho^{(2/3)+h} \cdot G^a\{\xi, [(9/4) + 3h]^2\} \qquad (10)$$

As can be seen from Eq. (18) in reference 1, in the vicinity of the line $\xi = -\infty$ these solutions are represented by

$$\psi = \rho^{(2/3)+h} (-\xi)^{-3/2} \qquad (11a)$$

and in the vicinity of the sonic line ($\xi = 0$) one obtains

$$\psi = \rho^{(2/3)+h} \left\{ \frac{\frac{3}{2} \cdot \Gamma\left(\frac{4}{3}\right) \cdot \Gamma\left(\frac{1}{2}\right)}{\Gamma\left(\frac{5}{3} + h\right) \cdot \Gamma\left(\frac{1}{6} - h\right)} + \right.$$

$$\left. \xi \frac{\frac{3}{2}\Gamma\left(\frac{2}{3}\right) \cdot \Gamma\left(\frac{1}{2}\right)}{\Gamma\left(\frac{4}{3} + h\right) \cdot \Gamma\left(-\frac{1}{6} - h\right)} \right\} \qquad (11b)$$

The last expression can be written in the form

$$\psi = \rho^{(2/3)+h} \left\{ \frac{3}{8} 2^{1/3} (-)^h \frac{\Gamma[(5/6) + h]}{\Gamma(5/6)} \frac{\Gamma(5/3)}{\Gamma[(5/3) + h]} - \right.$$

$$\left. (-)^h \xi \cdot \frac{3}{8} \cdot 2^{2/3} \frac{\Gamma[(7/6) + h]}{\Gamma(7/6)} \frac{\Gamma(4/3)}{\Gamma[(4/3) + h]} \right\} \qquad (11c)$$

If one studies the behavior of the functions G for high real values of $\sqrt{\lambda}$ (using, e.g., the method of Langer[3]) one finds, that everywhere in the range $-\infty < \xi < 0$ the function G is of the order of magnitude of its value at the sonic line We mention this for the following reason: Later ψ will be represented along the sonic line by a development in powers of ρ. This development will converge along the sonic line ($\xi = 0$) in the region from point B to point 0. We shall then obtain from this development a representation of ψ for values of $\xi \neq 0$ by inserting for each power of ρ, which occurs in the development of ψ along the sonic line, the corresponding particular solution for ψ. Because of the property of G just mentioned, this representation will then converge (even absolutely) for all values of ρ smaller than the value that ρ assumes at point 0—i.e., for $\rho < 9/4$. Also, the derivatives will converge absolutely; therefore within the region $\rho < 9/4$ (within the inner region), the differential equation, Eq. (4), for ψ is fulfilled.

The particular solutions for the outer region can be found by the following reasoning: The part of the hodograph field in which we are interested extends to the limiting characteristic E0 of Fig. 2. But one can extend the solution beyond this line by prescribing the boundary condition $\psi = 0$ along the continuation of the characteristic DE beyond point E. Such a continuation occurs physically if one constructs the flow field downstream of the limiting characteristic. We consider now the hodograph field up to the characteristic E'A, which corresponds to the line $\xi = 1$ in the

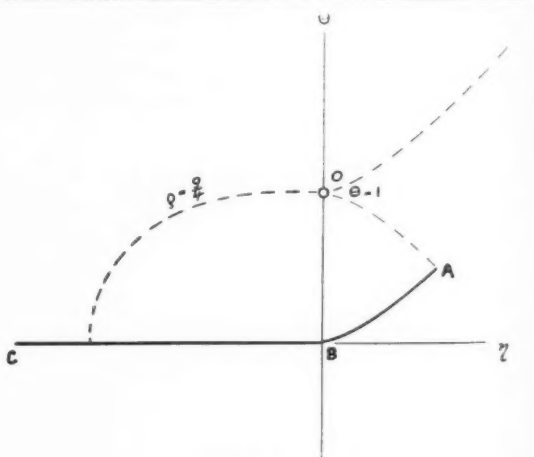

FIG. 3

$\bar{\eta}$, $\bar{\theta}$-plane. Because of the boundary condition $\psi = 0$ along DEE′, no singularity will propagate along E′A. Therefore the second term in Eq. (8) must vanish. Furthermore, the solution must vanish as ρ tends to infinity because of the condition along DE in the $\bar{\eta}$, $\bar{\theta}$-plane. Therefore $\sqrt{\lambda}$ must be smaller than $^1/_4$ [cf. Eq. (8)]. These conditions yield the same values of λ as in the inner region. A derivation of the same result by another point of view is found in references 1 and 8. Clearly, the exact shape of the boundary DEE′ does not matter after the transition to small values of θ_0 has been made.

As a result of these considerations, one finds that for 9/4 the solution can be represented by a superposition of the expressions

$$\psi = \rho^{-[(5/6)+h]} \cdot G^a\{\xi, [(9/4) + 3h]^2\} \qquad (12)$$

We must still consider the condition that the stagnation point is a branch point of the stream lines. In the $\bar{\eta}$, $\bar{\theta}$-system the stagnation point will correspond to $\bar{\eta} = -\infty$. Inspecting the functions G occurring in Eq. (12), one finds that only for $h = 0$ is the function G different from zero everywhere throughout the subsonic region (except naturally along the line $\xi = -\infty$), all other solutions have lines $\xi =$ const. along which G and therefore also ψ vanish. For these other solutions infinity represents a branch point of the stream lines. At infinity, the terms of the expressions (12) with the lowest value of h will prevail over the others and thus determine the character of the branch point. Thus the stagnation point will be a branch point of the stream lines only if the outer representation does not contain the term

$$\rho^{-5/6} \cdot G^a[\xi, (9/4)^2]$$

Thus the outer representation will be given as a superposition of the terms

$$\psi = \rho^{-[(11/6)+h]} \cdot G^a\{\xi[(21/4) + 3h]^2\} \qquad (h = 0,1,2 \ldots) \qquad (13a)$$

Along $\xi = -\infty$ they are represented by

$$\psi = (-\xi)^{-3/2} \cdot \rho^{-[(11/6)+h]} \qquad (13b)$$

in the vicinity of the sonic line, one then has

$$\psi = \rho^{-[(11/6)+h]} \left\{ \frac{3}{16} \cdot 2^{1/3} (-)^h \frac{\Gamma[(11/6) + h]}{\Gamma(11/6)} \frac{\Gamma(8/3)}{\Gamma[(8/3) + h]} - (-)^h \cdot \xi \cdot \frac{21}{64} \cdot 2^{2/3} \frac{\Gamma[(13/6) + h]}{\Gamma(13/6)} \frac{\Gamma(7/3)}{\Gamma[(7/3) + h]} \right\} \qquad (13c)$$

In the outer region ($\rho > 9/4$), the expression ψ for $\xi \neq 0$ will be constructed from the expression for ψ along the sonic line ($\xi = 0$) in a manner similar to that used in the inner region.

Let us now study the behavior of the solutions in the vicinity of point 0. One remarks that the differential equation (4) is invariant against a shift of the coordinates in the $\bar{\theta}$-direction. We assume momentarily that the origin of the $\bar{\eta}$,$\bar{\theta}$-system lies at point 0 and that the quantities ρ and ξ are defined within this system by Eqs. (5). They will then be denoted by $\bar{\rho}$ and $\bar{\xi}$. We try to find particular solutions (7), by which the solution of the present boundary value problem can be represented in the vicinity of point 0. The conditions imposed here are that, along the limiting characteristics AO and EO, no singularities propagate and that the limiting characteristics lie in the finite part of the physical plane. The condition that no singularities must propagate along these characteristics originates from the fact that at point A and E there is no singularity in the boundary conditions. In the vicinity of point 0, symmetric, as well as antisymmetric, solutions may occur.

To discuss these conditions, we write the particular solutions for ψ in the vicinity of the lines A0 or E0 ($\xi = 1$) in the form of Eq. (8). (This form corresponds to antisymmetric solutions; the treatment of symmetric solutions is similar.) If the second term in Eq. (8) is different from zero, then for positive values of the exponent a singularity will propagate along the characteristics; for negative values of the exponent, the line will map to infinity. Therefore one obtains, as general requirement, that the second term in Eq. (8) vanishes. One finds the following values of $\sqrt{\lambda}$:

for antisymmetric solutions $(11/4) + 3h$, $(7/4) + 3h$, $(3/4) \pm 3h$

for symmetric solutions $(1/4) + 3h$, $(5/4) + 3h$, $-(3/4) \pm 3h$ $(h = 0,1,2 \ldots)$

As discussed in reference 1 on page 50 (although with a somewhat different notation), not all of the negative values of $\sqrt{\lambda}$ listed above but only $\sqrt{\lambda} = -3/4$ and $\sqrt{\lambda} = -9/4$, will occur, since otherwise the vicinity of point 0 would map into several sheets of the physical plane. The particular solution with $\sqrt{\lambda} = -3/4$ has no physical significance if it occurs as the only singularity at point 0, but superimposed to the particular solution with $\sqrt{\lambda} = -9/4$ it shows at a far distance from the body the influence of its unsymmetry.

Which terms will occur in a development that represents ψ along the sonic line? In the original $\bar{\eta}$, $\bar{\theta}$-system with the origin at point B, point 0 corresponds to $\bar{\theta} = 1$. Then one finds from Eqs. (7) and (5) that the development around point 0 has the form

$$\psi \sim (\bar{\theta} - 1)^{-(1/6)+(2/3)\cdot\sqrt{\lambda}}$$

In the same arrangement as in the previous table one finds, as possible exponents of $(\bar{\theta} - 1)$,

$$(5/3) + 2h,\ 1 + 2h,\ -(5/3) + 2h$$
$$2h,\ (2/3) + 2h,\ -(2/3) + 2h$$

Among the corresponding particular solutions for ψ, those with the exponents $(2/3) + 2h$ and $(5/3) + 2h$ happen to give $\psi = 0$ along the sonic line; but ψ_η is different from zero. For particular solutions with the exponents $2h$ and $1 + 2h$, one has $\psi \neq 0$, $\psi_{\bar\eta} = 0$.

The particular solutions valid in the vicinity of point 0 represent ψ along the sonic line for $\bar\theta < 1$, as well as for $\bar\theta > 1$. The connection between the expressions in these regions is given by the fact that in the $\bar\eta$, $\bar\theta$-plane the particular solutions under consideration are either symmetric or antisymmetric with respect to the line $\bar\theta = 1$. Following this idea, one finds that the expression ψ for $\bar\theta > 1$ is found from expression ψ for $\bar\theta < 1$ by taking in any case the real root of the fractional power of $(\bar\theta - 1)$. (One should be aware of the fact that this rule does not hold for more general values of $\sqrt{\lambda}$.)

Summarizing this, one can say that, along the sonic line in the vicinity of point 0, ψ can be represented in the form

$$\psi = (\bar\theta - 1)^{-5/3} P_1(\bar\theta - 1) + P_2(\bar\theta - 1) \qquad (14)$$

where P_1 and P_2 (and later P_3, P_4, or simply P) denote suitable power series.

From the point of view of Tricomi's uniqueness and existence theorem, two different singularities—namely,

$$\psi = \bar\rho^{-5/6} G^a[\bar\xi,\ (9/4)^2]$$

$$\psi = \bar\rho^{-1/3} \cdot G^s[\bar\xi,\ (3/4)^2]$$

are admitted at point 0. The boundary condition is $\psi = 0$ along the entire boundary. The coefficients of these singular particular solutions are unknown. One of the arbitrary parameters that thus appear in the solution is unessential, since a factor, with which the hodograph solution is multiplied, changes only the scale of the physical plane. The other parameter is determined by the condition that the stagnation point is a branch point of the stream lines. The proper value of this parameter will appear in the future computations quite automatically.

We shall furthermore utilize the particular solutions (7) for imaginary values of $\sqrt{\lambda}$. Our main interest will lie in the question of convergence of a Fourier integral formed with these particular solutions. From this point of view their asymptotic behavior for high values of $|\sqrt{\lambda}|$ is of special interest. Asymptotic representations can be derived from the differential equation for G with a standard method (for instance reference 5). One finds

$$G^a(\xi, \lambda) \sim \frac{3}{2\sqrt{|\lambda|}} (-\xi)^{-1/4} (1 - \xi^3)^{1/12} \sinh\left(\frac{\sqrt{|\lambda|}}{3} \nu(\xi)\right) \qquad (\lambda < 0,\ |\lambda| \gg 1) \qquad (15a)$$

where

$$\nu(\xi) = 2 \cdot tg^{-1}(-\xi)^{-3/2} \qquad (15b)$$

The presentation is valid for $\xi < 0$—i.e., for the subsonic region with the exception of the sonic line. The following expressions for ψ will occur:

$$\psi = \rho^{-1/12} \cos\left[(\sqrt{|\lambda|}/3) \log \rho\right] \cdot G^a(\xi,\lambda) \qquad (16a)$$

$$\psi = \rho^{-1/12} \sin\left[(\sqrt{|\lambda|}/3) \log \rho\right] \cdot G^a(\xi,\lambda) \qquad (16b)$$

Near the line $\xi = -\infty$, according to the definition of $G^a(\xi,\lambda)$, they are represented by

$$\psi = (-\xi)^{-3/2} \cdot \rho^{-1/12} \cdot \cos\left[(\sqrt{|\lambda|}/3) \log \rho\right] \qquad (17a)$$

$$\psi = (-\xi)^{-3/2} \rho^{-1/12} \sin\left[(\sqrt{|\lambda|}/3) \log \rho\right] \qquad (17b)$$

The asymptotic expressions for ψ are found by inserting into Eqs. (16) the above representations for G:

$$\psi \sim \frac{3}{2\sqrt{|\lambda|}} \cdot \rho^{-1/12} \xi^{-1/4} (1 - \xi^3)^{1/12} \cdot \cos\left(\frac{\sqrt{|\lambda|}}{3} \log \rho\right) \cdot \sinh\left[\frac{\sqrt{|\lambda|}}{3} \nu\ (\xi)\right] \qquad (18a)$$

$$\psi \sim \frac{3}{2\sqrt{|\lambda|}} \cdot \rho^{-1/12} \xi^{-1/4} (1 - \xi^3)^{1/12} \cdot \sin\left(\frac{\sqrt{|\lambda|}}{3} \log \rho\right) \cdot \sinh\left[\frac{\sqrt{|\lambda|}}{3} \nu(\xi)\right] \qquad (18b)$$

Introducing a complex variable ζ by

$$\zeta = \log \rho + i\nu \qquad (19)$$

one can write the last expressions as

$$\psi \sim \frac{3}{2\sqrt{|\lambda|}} \cdot \rho^{-1/12} \xi^{-1/4} (1 - \xi^3)^{1/12} \cdot Im \sin\left(\frac{\sqrt{|\lambda|}}{3} \cdot \zeta\right) \qquad (20a)$$

$$\psi \sim \frac{3}{2\sqrt{|\lambda|}} \cdot \rho^{-1/12}\, \xi^{-1/4}\, (1 - \xi^3)^{1/12} \cdot Im \cos\left(\frac{\sqrt{|\lambda|}}{3} \cdot \zeta\right) \tag{20b}$$

(3) The Construction of the Solution of the Boundary Value Problem

The derivation of the solution given in the following will contain certain tentative elements and therefore cannot claim to be applicable in general. However it may be useful in similar cases. The solution will subsequently be verified.

We try to find a representation of the function along the sonic line. In the previous paragraph we found the following properties: (a) In the vicinity of point B, ψ is represented by a power series that proceeds in powers $\rho^{(2/3)+k}$. Because of relation (5) and since along the sonic line $\tilde{\eta} = 0$, one has

$$\psi = \tilde{\theta}^{4/3}\, P_3(\tilde{\theta}^2)$$

(b) For values of $\tilde{\theta} > 1$ one finds similarly

$$\psi = \tilde{\theta}^{-11/3}\, P_4(\tilde{\theta}^{-2})$$

(c) The development at $\tilde{\theta} = 1$ is given in Eq. (14) as

$$\psi = (\tilde{\theta} - 1)^{5/3} \cdot P_1(\tilde{\theta} - 1) + P_2(\tilde{\theta} - 1)$$

Since the inner and outer representations proceed in terms of $\tilde{\theta}^2$, we introduce

$$\tilde{\theta}^2 = z \tag{21}$$

and then can write the above conditions as

$$\psi = z^{2/3}\, P_3(z) \qquad (\text{for } z < 1) \tag{22}$$

$$\psi = z^{-11/6} \cdot P_4(z^{-1}) \qquad (\text{for } z > 1) \tag{23}$$

$$\psi = (z - 1)^{5/3} \cdot P_1(z - 1) + P_2(z - 1) \qquad (\text{in the vicinity of } z = 1) \tag{24}$$

In the last expression one must always use the real roots of the fractional powers. From the requirements of convergence in the $\tilde{\eta}, \tilde{\theta}$-plane, one can conclude that Eq. (22) converges for $z < 1$, Eq. (23) converges for $z > 1$, and Eq. (24) converges for $|(z - 1)| < 1$.

These statements are certainly not sufficient to determine the function along the sonic line or to characterize it as a hypergeometric function. So it is only tentative if we assume that at the origin the function ψ is represented by

$$\psi = z^{2/3} F(a,b,c,z) \tag{25}$$

In the vicinity of the point $z = 1$, the solution will then be represented by two other hypergeometric series that proceed in powers of $(z - 1)$. Because of the conditions that one obtains for the transition through point 1, one finds that the outer solution must be represented by a superposition of the same hypergeometric functions. Thus it follows that the hypergeometric differential equation fulfilled by the function in the outer region is the same as that fulfilled by the inner representation, for a second-order differential equation is fully determined by two linearly independent solutions. Now, if for $z = 0$ one solution has the form of Eq. (25), then because of the relation

$$\frac{\Gamma(a) \cdot \Gamma(b)}{\Gamma(c)} \cdot F(a,b,c,z) = \frac{\Gamma(a) \cdot \Gamma(b - a)}{\Gamma(c - a)}\, (-z)^{-a} \cdot F(a,\, 1 + a - c,\, 1 + a - b,\, z^{-1}) + \frac{\Gamma(b) \cdot \Gamma(a - b)}{\Gamma(c - b)}\, (-z)^{-b} \cdot F(b,\, 1 + b - c,\, 1 + b - a,\, z^{-1}) \tag{26}$$

(cf. reference 6, page 257), the linearly independent solutions at infinity have the forms

$$z^{-2/3} \cdot z^{-a} \cdot P(z^{-1})$$
$$z^{-2/3}\, z^{-b} \cdot P(z^{-1})$$

One finds from the first expression, by a comparison with Eq. (23),

$$a = 5/2 \tag{27}$$

The other linearly independent solution of the hypergeometric equation will not be needed. To investigate the behavior at point $z = 1$, we use the formula

$$F(a,b,c,z) = \frac{\Gamma(c)\cdot\Gamma(c-a-b)}{\Gamma(c-a)\cdot\Gamma(c-b)}\cdot F(a,\ b,\ 1+a+b-c,\ 1-z) + \frac{\Gamma(c)\cdot\Gamma(a+b-c)}{\Gamma(a)\cdot\Gamma(b)}(1-z)^{c-a-b}\cdot F(c-a,\ c-b,\ 1+c-a-b,\ 1-z) \quad (28)$$

(reference 6, page 252). This equation shows that assumption (25) yields, at $z = 1$, an expression of the desired form if the exponent of the second hypergeometric function has the right value—i.e., if

$$c - a - b = -5/3$$

Thus, with the value of a found previously [Eq. (27)],

$$c - b = 5/6 \quad (29)$$

It is not necessary to make the same consideration for the outer representation since the outer solution fulfills the same differential equation and therefore has, at point $z = 1$, the same linearly independent solutions.

Up to now we obtained as a likely expression for the inner region

$$\psi = z^{2/3}F[5/2,\ b,\ b + (5/6),\ z]$$

Then the particular solution, with the exponent a at $z = \infty$, will, according to Eq. (26), be given by

$$\psi = Cz^{-11/6}F[5/2,\ (8/3) - b,\ (7/2) - b,\ z^{-1}] \quad (30a)$$

Here C is a constant that will be determined subsequently.

Possible values of b are obtained if one examines how the inner and outer solutions can be joined at point $z = 1$. By applying Eq. (28) one obtains, for the inner representation,

$$\psi = z^{2/3}\left\{\frac{\Gamma[b + (5/6)]\Gamma(-5/3)}{\Gamma[b - (5/6)]\cdot\Gamma(5/6)}\cdot F(5/2),\ b,\ 8/3,\ 1-z) + \frac{\Gamma[b + (5/6)]\cdot\Gamma(5/3)}{\Gamma(5/2)\cdot\Gamma(b)} \times (1-z)^{-5/3}\cdot F[b - (5/3),\ 5/6,\ -2/3,\ 1-z]\right\} \quad (31a)$$

and, for the outer representation,

$$\psi = C\cdot z^{-11/6}\left\{\frac{\Gamma[(7/2) - b]\Gamma(-5/3)}{\Gamma(1-b)\cdot\Gamma(5/6)}\cdot F[5/2,\ (8/3) - b,\ 8/3,\ 1 - z^{-1}] + \frac{\Gamma[(7/2) - b]\cdot\Gamma(5/3)}{\Gamma(5/2)\cdot\Gamma[(8/3) - b]}(1 - z^{-1})^{-5/3}\cdot F(1-b,\ 5/6,\ -2/3,\ 1 - z^{-1})\right\} \quad (31b)$$

Here the second term may be written in a slightly different form,

$$\psi = C\cdot z^{-11/6}\left\{\frac{\Gamma[(7/2) - b]\cdot\Gamma(-5/3)}{\Gamma(1-b)\cdot\Gamma(5/6)}\cdot F[5/2,\ (8/3) - b,\ 8/3,\ 1 - z^{-1}] - \frac{\Gamma[(7/2) - b]\cdot\Gamma(5/3)}{\Gamma(5/2)\cdot\Gamma[(8/3) - b]}\cdot z^{5/3}(1-z)^{-5/3}\cdot F(1-b,\ 5/6,\ -2/3,\ 1 - z^{-1})\right\} \quad (31c)$$

Since all hypergeometric functions (with the powers of z and $z - 1$ in front included), fulfill the same differential equation, it is self-evident that the power series with the exponents 0 and $-5/3$ in Eqs. (31a) and (31c) agree, although this is not obvious from the form indicated. Therefore one needs only to equate the first coefficients

$$\frac{\Gamma[b + (5/6)]\cdot\Gamma(-5/3)}{\Gamma[b - (5/3)]\ \Gamma(5/6)} = C\frac{\Gamma[(7/2) - b]\ \Gamma(-5/3)}{\Gamma(1-b)\ \Gamma(5/6)} \quad (32a)$$

$$\frac{\Gamma[b + (5/6)]\cdot\Gamma(5/3)}{\Gamma(5/2)\cdot\Gamma(b)} = -C\frac{\Gamma[(7/2) - b]\cdot\Gamma(5/3)}{\Gamma(5/2)\cdot\Gamma[(8/3) - b]}. \quad (32b)$$

By a division, C is eliminated

$$\Gamma(b)/\Gamma[b - (5/3)] = -\Gamma[(8/3) - b]/\Gamma(1-b)$$

and one finds, because of the relation

$$\Gamma(z)\Gamma(1-z) = \pi/\sin\pi z$$

that

$$\sin b\pi = -\sin [b - (5/3)]\pi$$

Hence, $b = (5/6) + k$, where k is an integral number. Actually, only $b = 5/6$ will be used in the solution (this is a further assumption). C is then found from one of the Eqs. (32) as $C = -1/2$. Thus one has, as likely representation for ψ along the sonic line,

$$\psi = z^{2/3} F(5/2, 5/6, 5/3, z) \tag{33a}$$

for $z < 1$ and

$$\psi = -(1/2) \cdot z^{-11/6} F(5/2, 11/6, 8/3, z^{-1}) \tag{33b}$$

for $z > 1$. This solution will be verified in the next section.

(4) Verification of the Solution

From the expression for ψ along the sonic line given in Eqs. (33), one obtains solutions in the $\tilde{\eta}$, $\tilde{\theta}$-plane simply by replacing the various powers of z (or of $\tilde{\theta}$) which occur in these series representations by the corresponding particular solution (11) and (13) for $\tilde{\theta} < 1$ and $\tilde{\theta} > 1$, respectively.

As mentioned before, these series representations will converge automatically inside and outside of the line $\rho = 9/4$. Thus it follows immediately that discontinuities can occur only along the line $\rho = 9/4$.

It will be the object of this section to show that no discontinuities are present along this line except at point 0. This is done by deriving from Eqs. (33) another representation of ψ whose region of convergence includes the line $\rho = 9/4$ and thus shows that along this line no singularities are encountered.

From Eq. (33a) one obtains for the general term of the inner solution along the sonic line

$$\tilde{\theta}^{4/3} \cdot \frac{\Gamma[(5/2) + h]}{\Gamma(5/2)} \cdot \frac{\Gamma[(5/6) + h]}{\Gamma(5/6)} \cdot \frac{\tilde{\theta}^{2h}}{\Gamma[(5/3) + h]} \cdot \Gamma(h + 1)$$

Then one obtains by means of Eq. (11) for the general term in the development of ψ

$$\left(\frac{4}{9}\rho\right)^{(2/3)+h} \cdot \frac{8}{3} \cdot 2^{-1/3} (-)^h \times G^a\left[\xi, \left(\frac{9}{4} + 3h\right)^2\right] \cdot \frac{\Gamma[(5/2) + h]}{\Gamma(5/2)} \cdot \frac{1}{\Gamma(h + 1)}$$

Thus, because of Eq. (11a), ψ is represented in the vi-

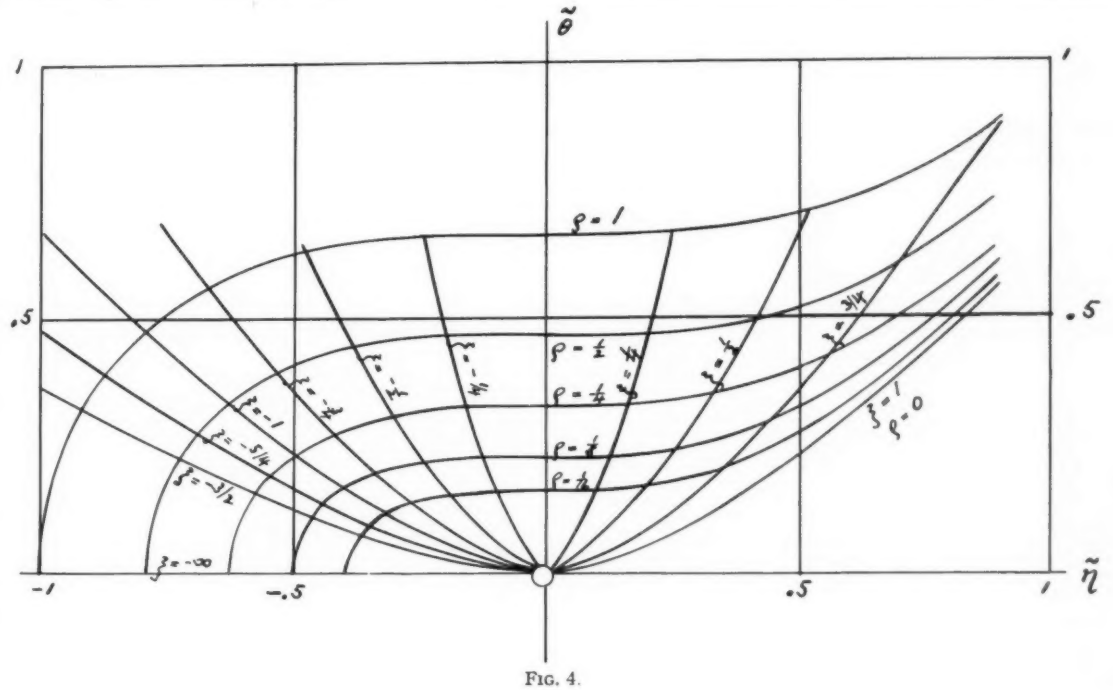

FIG. 4.

cinity of $\xi = -\infty$ by

$$\psi = (-\xi)^{-3/2}\cdot\frac{8}{3}\cdot 2^{-1/3}\left(\frac{4}{9}\rho\right)^{2/3}\cdot\sum_{h=0}^{\infty}\frac{\Gamma[(5/2)+h]}{\Gamma(5/2)}\times\frac{(-)^h\left(\frac{4}{9}\rho\right)^h}{\Gamma(h+1)}$$

Hence,

$$\psi = \frac{8}{3}\cdot 2^{-1/3}\,(-\xi)^{-3/2}\cdot\left(\frac{4}{9}\rho\right)^{2/3}\left(1+\frac{4}{9}\rho\right)^{-5/2} \tag{34}$$

The treatment of the solutions for $\rho > 9/4$ is similar and yields the same result. The simplicity of the last expression is remarkable.

From this result one can derive a representation of the solution, by means of the functions G^a for negative values of λ, which holds through the entire subsonic region. Assume for this purpose that in the following Fourier integral the functions g_1 and g_2 are known:

$$\left(\frac{4}{9}\rho\right)^{2/3}\left(1+\frac{4}{9}\rho\right)^{-5/2} = \rho^{-1/12}\int_0^\infty g_1\left(\frac{\sqrt{|\lambda|}}{3}\right)\cdot\cos\left(\frac{\sqrt{|\lambda|}}{3}\log\rho\right)\cdot d\,\frac{\sqrt{|\lambda|}}{3} + \rho^{-1/12}\int_0^\infty g_2\left(\frac{\sqrt{|\lambda|}}{3}\right)\sin\left(\frac{\sqrt{|\lambda|}}{3}\log\rho\right)\cdot d\,\frac{\sqrt{|\lambda|}}{3} \tag{35}$$

Then because of Eq. (16), ψ can be expressed by

$$\psi = \frac{8}{3}\cdot 2^{-1/3}\cdot\left\{\int_0^\infty g_1\left(\frac{\sqrt{|\lambda|}}{3}\right)\cdot\cos\left(\frac{\sqrt{|\lambda|}}{3}\log\rho\right)\cdot G^a(\xi_1-|\lambda|)\cdot d\,\frac{\sqrt{|\lambda|}}{3} + \int_0^\infty g_2\left(\frac{\sqrt{|\lambda|}}{3}\right)\cdot\sin\left(\frac{\sqrt{|\lambda|}}{3}\log\rho\right)\cdot G^a(\xi,-|\lambda|)d\,\frac{\sqrt{|\lambda|}}{3}\right. \tag{36}$$

The important question is the range of values ξ in which this expression converges. It was mentioned previously that the convergence of such expressions is the same as the convergence of the corresponding asymptotic representations. Using Eqs. (16), (17), (18), (19), and (20), one obtains approximately

$$\psi \sim \frac{4}{3}\cdot 2^{-1/3}\cdot\rho^{-1/12}\,\xi^{-1/4}\,(1-\xi^3)^{1/12}\left\{\int_0^\infty g_1\left(\frac{\sqrt{|\lambda|}}{3}\right)\cdot\frac{\cos\left(\frac{\sqrt{|\lambda|}}{3}\log\rho\right)}{\sqrt{|\lambda|}/3}\cdot\sinh\left[\frac{\sqrt{|\lambda|}}{\rho}\cdot\nu(\xi)\right]\cdot d(\sqrt{|\lambda|}/3) + \int_0^\infty g_2\left(\frac{\sqrt{|\lambda|}}{3}\right)\cdot\frac{\sin\left(\frac{\sqrt{|\lambda|}}{3}\log\rho\right)}{\sqrt{|\lambda|}/3}\sinh\left[\frac{\sqrt{|\lambda|}}{3}\,\nu(\xi)\right]\cdot d(\sqrt{|\lambda|}/3)\right\} \tag{37}$$

where $\nu(\xi)$ has been defined in Eq. (15b). With the definition of complex variable ζ given in Eq. (19), the last expression can be written as

$$\psi \sim \frac{4}{3}\cdot 2^{-1/3}\,\rho^{-1/12}\,\xi^{-1/4}\,(1-\xi^3)^{1/12}\cdot Im\left\{\int_0^\infty g_1\left(\frac{\sqrt{|\lambda|}}{3}\right)\cdot\frac{\sin\left(\frac{\sqrt{|\lambda|}}{3}\zeta\right)}{\frac{\sqrt{|\lambda|}}{3}}\cdot d(\sqrt{|\lambda|}/3) - \int_0^\infty g_2\left(\frac{\sqrt{|\lambda|}}{3}\right)\cdot\frac{\cos\left(\frac{\sqrt{|\lambda|}}{3}\zeta\right)}{\frac{\sqrt{|\lambda|}}{3}}\cdot d(\sqrt{|\lambda|}/3)\right\}$$

or

$$\psi \sim \frac{4}{3}\cdot 2^{-1/3}\cdot\rho^{-1/12}\cdot\xi^{-1/4}\,(1-\xi^3)^{1/12}\cdot Im\int_0^\infty g_1\left(\frac{\sqrt{|\lambda|}}{3}\right)\cdot d\,\frac{\sqrt{|\lambda|}}{3}\cdot\int\cos\left(\frac{\sqrt{|\lambda|}}{3}\zeta\right)d\zeta + \int_0^\infty g_2\left(\frac{\sqrt{|\lambda|}}{3}\right)\cdot\frac{d\sqrt{|\lambda|}}{3}\int\sin\left(\frac{\sqrt{|\lambda|}}{3}\zeta\right)\cdot d\zeta$$

In the region of uniform convergence, the sequence of the integrations can be interchanged,

$$\psi \sim \frac{4}{3}\cdot 2^{-1/3}\,\rho^{-1/12}\,\xi^{-1/4}\,(1-\xi^3)^{1/12}\cdot Im\int d\zeta\left[\int_0^\infty g_1\left(\frac{\sqrt{|\lambda|}}{3}\right)\cdot\cos\left(\frac{\sqrt{|\lambda|}}{3}\,\zeta\right)\frac{d\sqrt{|\lambda|}}{3}+\int_0^\infty g_2\left(\frac{\sqrt{|\lambda|}}{3}\right)\cdot\sin\left(\frac{\sqrt{|\lambda|}}{3}\,\zeta\right)\frac{d\sqrt{|\lambda|}}{3}\right]$$

The second integrations can be carried out in a closed form because of Eqs. (35) and (19),

$$\psi \sim \frac{4}{3}\cdot 2^{-1/3}\cdot\xi^{-1/4}\,(1-\xi^3)^{1/12}\left(\frac{4}{9}\rho\right)^{-1/12}\cdot Im\int d\zeta\left(\frac{4}{9}\cdot e^{\zeta}\right)^{3/4}\cdot\left(1+\frac{4}{9}\,e^{\zeta}\right)^{-5/2} \tag{38}$$

The particular solutions occurring in Eqs. (36) and (37) have an exponential behavior in the ξ-direction. The limit of convergence will be given by a line $\xi = \text{const.}$ or $\nu(\xi) = \text{const.}$ In the complex ζ-plane, at least one singularity will lie at the line of convergence. The singularities of the integrand in Eq. (28) are the same as the singularities of the integral. The line $\xi = -\infty$ corresponds to $\nu(\xi) = 0$. Obviously the singularities of the integrand in Eq. (38) lie at

$$e^{\zeta} = -4/9$$

or

$$\zeta = \log 4/9 + i\pi(2n+1)$$

where n is an integral number. Hence it follows that the development of Eq. (37), and therefore also Eq. (36), converges for

$$-\pi < \nu(\xi) < \pi$$

By Eq. (15b) we then find that in terms of ξ the expression converges for $\xi < 0$—i.e., in the entire subsonic part of the hodograph plane. This shows that the inner and outer representation match along the entire line of convergence $\rho = 9/4$.

As a check one can determine, from the original inner and outer representations, ψ_ξ along the sonic line (it will also appear as a hypergeometric series) and see whether it fulfills the matching conditions at point 0. From the point of view of the construction of the solution this check is unnecessary.

(5) The Pressure Distribution on the Pressure Side of the Plate

Putting the stream density at sonic speed equal to 1, one has the relation

$$y = \psi$$

The x coordination is determined by

$$x_\eta = (\gamma+1)^{1/3}\cdot\eta\cdot\psi_\theta$$

$$x_\theta = (\gamma+1)^{1/3}\psi_\eta$$

From the definitions for ρ and ξ [Eqs. (5)], one finds, for $\bar\theta \neq 0$,

$$\partial\rho/\partial\bar\theta = 0$$

$$\partial\xi/\partial\bar\theta = (-\bar\eta)^{-3/2}\cdot(-\xi)^{5/2}$$

Remembering the definitions (2) and (3) for $\bar\eta$ and $\bar\theta$, one thus finds, from Eq. (34),

$$x_\eta = -4\left(\frac{\gamma+1}{2}\right)^{1/3}\cdot\left(\frac{3}{2}\theta_0\right)^{-1/3}\times\left[\frac{-\eta}{\left(\frac{3}{2}\theta_0\right)^{2/3}}\right]^{3/2}\cdot\left[1+\frac{(-\eta)^3}{\left(\frac{3}{2}\theta_0\right)^2}\right]^{-2.5}$$

Putting the origin of the x,y-system into the stagnation point and introducing a variable of integration

$$\tau = -\eta/[(3/2)\theta_0]^{2/3}$$

one obtains

$$x = 4\left(\frac{\gamma+1}{2}\right)^{1/3}\cdot\left(\frac{3}{2}\theta_0\right)^{1/3}\times\int_\infty^{\tau=-\eta/[(3/2)\theta_0]^{2/3}}\tau^{1.5}\,(1+\tau^3)^{-2.5}\,d\tau$$

The overall length of the plate is given by

$$L = 4\left(\frac{\gamma+1}{2}\right)^{1/3}\left(\frac{3}{2}\theta_0\right)^{1/3}\int_\infty^0\tau^{1.5}\,(1+\tau^3)^{-2.5}\,d\tau$$

Here x and L appear with a negative sign. In order to obtain the positive sign (which corresponds to Figs. 1, 2, and 3), the expression must be multiplied with -1. By the substitution

$$\tau^3 = v/(1-v)$$

the last integral assumes the form

$$\int_\infty^0\tau^{1.5}\,(1+\tau^3)^{-2.5}\,d\epsilon = -\frac{1}{3}\int_0^1 v^{-1/6}(1-v)^{2/3}\,dv$$

This is a B-Integral (reference 6, page 212). One finds

$$\int_\infty^0\tau^{1.5}(1+\tau^3)^{-2.5}\,d\tau = -\frac{1}{3}\,\frac{\Gamma(5/6)\cdot\Gamma(5/3)}{\Gamma(5/2)}$$

thus

$$|L| = \frac{4}{3}\cdot\left(\frac{\gamma+1}{2}\right)^{1/3}\cdot\left(\frac{3}{2}\theta_0\right)^{1/3}\cdot\frac{\Gamma(5/6)\cdot\Gamma(5/3)}{\Gamma(5/2)}$$

The lower part of Fig. 5 shows $\eta/[(3/2)\theta_0]^{2/3}$ versus x/L. Since the pressure coefficient is, in the present approximation, expressed by

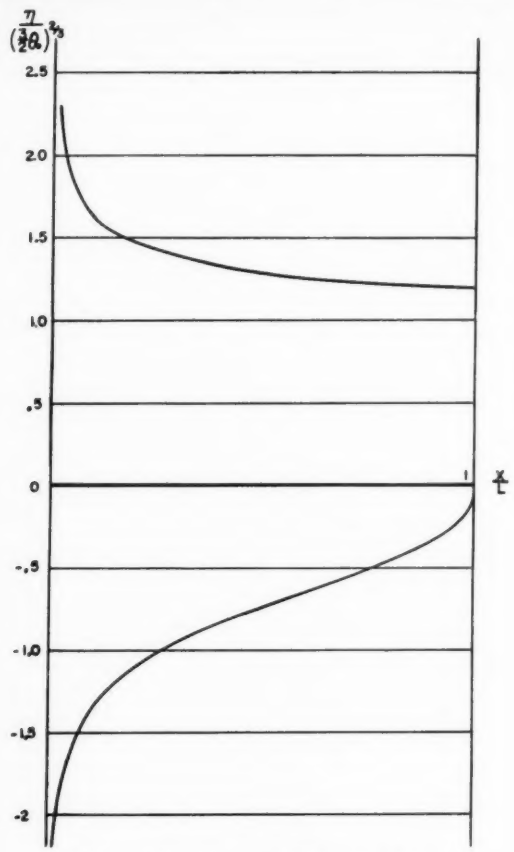

FIG. 5. Pressure distributions over plate.

$$c_p = -2(\gamma + 1)^{-1/3} \cdot \eta$$

this figure can be interpreted as a representation of

$$-c_p/2(\gamma + 1)^{-1/3} \cdot [(3/2)\theta_0]^{2/3}$$

Occasionally one may be interested in the behavior of the flow at a far distance from the body. It can be characterized by ψ along the sonic line. The portion of the solution which is singular at point 0 is represented by the second term of Eq. (31a). One has, with $b = 5/6$,

$$\psi = z^{2/3} \cdot \frac{\Gamma(5/3)^2}{\Gamma(5/2)\Gamma \cdot (5/6)} \cdot (1 - z)^{-5/3} \cdot F(-5/6, 5/6, -2/3, 1 - z)$$

Remembering that

$$z = (\theta/\theta_0)^2$$

one obtains as the behavior of ψ along the sonic line in the vicinity of point 0

$$\psi = 2^{-5/3} \frac{\Gamma(5/3)^2}{\Gamma(5/2) \cdot \Gamma(5/6)} \cdot \left[\left(1 - \frac{\theta}{\theta_0}\right)^{-5/3} + \frac{19}{12} \left(1 - \frac{\theta}{\theta_0}\right)^{-2/3} \right]$$

This expression corresponds to a plate with a length given by Eq. (40). With the assumption made previously that the stream density at sonic speed is 1, one then obtains for a plate of length L as the behavior of ψ along the sonic line in the vicinity of point 0

$$\psi = -L \cdot 2^{-5/3} \cdot \frac{3}{4} \cdot \left(\frac{\gamma + 1}{2}\right)^{-1/3} \cdot \frac{\Gamma(5/3)}{\Gamma(5/6)^2} \times \left(\frac{3}{2}\theta_0\right)^{-1/3} \left[\left(1 - \frac{\theta}{\theta_0}\right)^{-5/3} + \frac{19}{12} \left(1 - \frac{\theta}{\theta_0}\right)^{-2/3} \right]$$

(6) The Pressure Distribution on the Suction Side of the Plate

At a first glance the task of determining the pressure distribution at the suction side of the plate appears rather hopeless, because of the presence of the cavitation region. However, the size of the cavitation region depends upon the angle of attack. If the angle of attack is made smaller, then the region of the plate which is influenced by the cavitation region becomes smaller, so that, for a sufficiently small angle of attack, the boundary condition in the cavitation region need to be introduced only in a very rough form. We have here the same reasoning as in the boundary condition for the pressure side of the plate. Mathematically, the diminishing importance of the cavitation region expresses itself by the fact that the map of its boundary moves to infinity in the $\bar{\eta}$, $\bar{\theta}$-plane as θ_0 tends to zero.

Moreover, the region of the flow field in which the transonic approximation cannot be applied shrinks with decreasing angle of attack; thus it is even possible to apply transonic approximations for the determination of the pressure distribution.

Thus one obtains the following problem: By the previous investigations the flow field up to the limiting Mach wave AE has been determined; one must find the flow downstream of it. One possible method of approach is the method of characteristics.

To reduce the amount of numerical work the solution is continued beyond the limiting Mach wave 0E by analytical means up to the line $\bar{\theta} = 0$. For $\bar{\eta} > 0$ the location of this line in the physical plane can be found in a general manner, since the representation of the solution along the line $\bar{\theta} = 0$ is known for $\bar{\eta} < 0$. One can use for this purpose Eqs. (3) and (43) of reference 4. In the continuation of the solution beyond the limiting Mach wave E0, the line $\bar{\theta} = 0$ does not represent the surface of the flat plate (as one might suppose because of the value for $\bar{\theta}$ which prevails), but it represents a line in the flow field where the velocity vector is parallel to the plate surface.

One difficulty must still be overcome: As one goes along the line $\bar{\theta} = 0$ or along the limiting characteristic E0 toward the leading edge, the value of $\bar{\eta}$ tends to infinity. Thus one does not have a starting condition

for the method characteristics. Moreover, the compression waves coming from the sonic line are reflected at the plate as compression waves and then coalesce to form a shock. It appears desirable to take into account the presence of this shock. Therefore the flow field in the vicinity of the leading edge has been determined analytically. For large values of ρ the term $\rho^{-11/6} \cdot G^a [\xi, (21/4)^2]$ predominates in the subsonic region, as well in its continuation beyond the line E0. If the preshock solution has this form, then the shock can be determined by the method shown in reference 9. The only difference between the problem of reference 9 and the present one is the value of λ.

The solution for the flow thus obtained has been used for the flow field in the vicinity of the leading edge, in a region where the neglect of the other terms contributes less than about 10 per cent of the entire solution. This region covers about 5 per cent of the length of the plate.

The rest of the pressure distribution is then obtained by the method of characteristics. The result is shown in Fig. 5.

The pressure distribution thus obtained is close to the expression which the formula for x valid in the subsonic region would yield if it is also applied in the supersonic region—i.e., if one expresses x as

$$x = 4\left(\frac{\gamma+1}{2}\right)^{1/3}\left(\frac{3}{2}\theta_0\right)^{1/3}\int_{\infty}^{\tau=\eta/[(3/2)\theta_0]^{2/3}} \times \tau^{1.5}\,(1-\tau^2)^{-2.5}\,d\tau$$

This result would have been obtained if one had admitted in the supersonic region a multiply-covered region of the physical plane (a fold) instead of the shock. If such a fold and the change of state occurring in it is rather small, the replacement of a shock by the fold is quite harmless. In the present case, however, the value of $\bar{\eta}$ along a stream line which passes the fold would go to infinity (at the last Mach wave of the Meyer expansion) and then return to finite values. Under these circumstances a more careful computation appeared desirable. The result, however, shows that even here the effect of the shock on the pressure distribution over the plate is rather small.

(7) Discussion of the Results

The pressure obtained by a Meyer expansion which deflects a sonic parallel flow by an angle θ_0 gives a quantity suitable for comparison with the pressures that arise in the present case. One obtains then $\eta/[(3/2)\theta_0]^{2/3} = 1$. This is also the value that would be obtained at the suction side of the plate if the flow were extended to infinity beyond the trailing edge (or, in other words, this is the asymptot of the curve $\eta/[(3/2)\theta_0]^{2/3}$ versus x on the suction side). The average value of $\eta/[(3/2)\theta_0]^{2/3}$ on the suction side is 1.37. The same average on the pressure side is 0.81. The center of pressure of the upper side lies at 46 per cent; the center of pressure at the pressure side, at 35 per cent; the center of pressure of the entire wing, at 42 per cent of the chord.

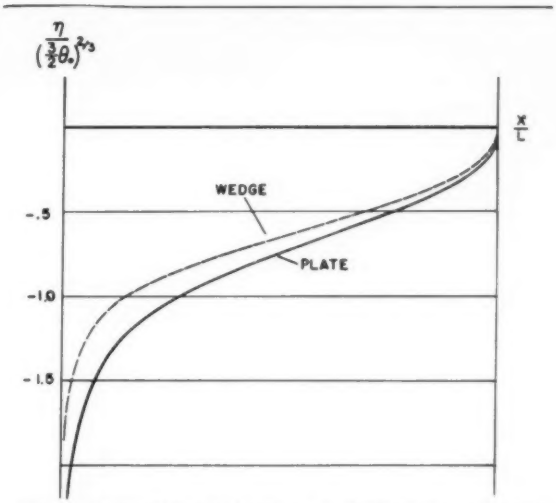

Fig. 6. Comparison of the pressure distribution on the pressure side of the plate with pressure distributions at a wedge with the same slope of the side.

That the values of $\eta/[(3/2)\theta_0]^{2/3}$ at the suction side are larger than 1 (than those obtained by a Meyer expansion) is caused by the centrifugal forces of the air which "spills" over. At the leading edge the pressure tends to infinity. This is due to the approximation used. η at the leading edge is proportional to $x^{-1/5}$. The behavior is the same for both sides of the plate. The power of x which occurs here is dictated by the lowest negative power of ρ which occurs in the outer solution—i.e., it is caused by the expression $\rho^{-11/6}G^a[\xi(21/4)^2]$. We remember that originally the outer solution contained also a term with $\rho^{-5/6}$ and that this term was omitted because of the condition that the stagnation point is also a branch point of the stream lines. At first it may appear surprising that the behavior at the leading edge is connected to a condition at the stagnation point, however in the present case the stagnation point lies close to the leading edge and its distance from the leading edge tends to zero with the angle of attack. This explains its strong influence on the pressure distribution at the leading edge. One sees that the pressure recovery in the vicinity of the leading edge need not be typical for the flow over a sharp edge in cases where the stagnation point lies at a distance from the edge.

In Fig. 6 the pressure distribution on the pressure side has been compared with the pressure distribution at the side of a wedge with a half nose angle of θ_0. The boundary conditions at the trailing edge are the same. At the leading edge a difference exists due to the pressure build up caused by the centrifugal forces of the air which spills over. The general character of the two curves is similar; the order of magnitude of the pressure is the same.

REFERENCES

[1] Guderley, Gottfried, *Two-Dimensional Flow Patterns with a Free Stream Mach Number Close to One*, AF Technical Report 6343, ATI No. 122738, May, 1951.

[2] Guderley, Gottfried, and Yoshihara, Hideo, *Two-Dimensional Unsymmetric Flow Patterns at Mach Number 1*, Journal of the Aeronautical Sciences, Vol. 20, No. 11, p. 757, November, 1953.

[3] Langer, R. E., *On Asymptotic Solutions of Ordinary Differential Equations with an Application to Bessel Functions of Large Order*, Transactions, Am. Math. Soc., pp. 23–64, 1931.

[4] Guderley, Gottfried, *Singularities at the Sonic Velocity*, Technical Report F-TR-1171 ND Wright-Patterson Air Force Base.

[5] Seifert, H., *Zur Asymptotischen Integration von Differentialgleichungen*, Mathematische Zeitschrift 48, p. 173; Springer Verlag, Berlin, 1942.

[6] Copson, E. T., *An Introduction to the Theory of a Complex Variable;* Oxford University Press.

[7] Guderley, G., and Yoshihara, H., *The Flow over a Wedge Profile at Mach Number 1*, Journal of the Aeronautical Sciences, Vol. 17, No. 11, p. 723, November, 1950.

[8] Marschner, Bernard, Thesis, California Institute of Technology, 1953.

[9] Barish, David T., and Guderley, Gottfried, *Asymptotic Forms of Shock Waves in Flows over Symmetrical Bodies at Mach One*, Journal of the Aeronautical Sciences, Vol. 20, No. 7, p. 491, July, 1953.

Results of Some Base Pressure Experiments at Intermediate Reynolds Numbers with $M = 2.84$

(*Continued from page 260*)

(from 3.3 to 10.4) as Reynolds Number decreases from 430,000 to 49,000.

(3) No noteworthy effects of base pressure orifice location ($0.30 \leq r/r_0 \leq 0.90$) and sting diameter ($0.177 \leq d/D \leq 0.233$) on the base pressure coefficient were observed.

REFERENCES

[1] Crocco, L., and Lees, L., *A Mixing Theory for the Interaction Between Dissipated Flows and Nearly Isentropic Streams*, Journal of the Aeronautical Sciences, Vol. 19, No. 10, p. 649, October, 1952.

[2] Bogdonoff, S. M., *A Preliminary Study of Reynolds Numbers Effect on Base Pressure at $M = 2.95$*, Journal of the Aeronautical Sciences, Vol. 19, No. 3, p. 201, March, 1952.

[3] Perkins, E. W., *Experimental Investigation of the Effects of Support Interference on the Drag of Bodies of Revolution at a Mach number of 1.5*, NACA RM A8B05, May 7, 1948.

[4] Chapman, D. R., *An Analysis of Base Pressure at Supersonic Velocities and Comparison with Experiment*, NACA TN 2137, July, 1950. Also NACA TR 1051, 1951.

[5] U.C.L.A. Staff Members, *Report on Supersonic Wind Tunnel*, Internal Report, Dept. of Engineering, University of California at Los Angeles, July, 1950.

[6] Davis, M. A., *Calibration of the Mach Number 2.9 Nozzle in the Supersonic Wind Tunnel*, Masters Thesis, Dept. of Engineering, University of California at Los Angeles, January, 1952.

[7] Maslach, G. J., *A Precision Manometer for Low Pressures*, Review of Scientific Instruments, Vol. 23, No. 7, p. 367, July, 1952.

Notice to Contributors

Manuscripts submitted for publication *must* be double- or triple-spaced originals. There should be wide margins on both sides of the sheets and triple spacing around formulas to allow for the marking of directions to the printer.

Original drawings (jet black India ink on white paper or tracing cloth) should accompany the manuscript. (*Blueprints are not acceptable.*) Photographs *must* be on glossy paper. The smallest lettering on 8- by 10-in. figures should be no less than ¼ in. high.

Only the simplest formulas should be typewritten, all others should be carefully written in pen and ink. The differences between capital and lower-case letters and Greek symbols should be clearly distinguished.

See Inside Back Cover of this issue for further details.

Readers' Forum

BRIEF REPORTS of investigations in the aeronautical sciences and discussions of papers published in the JOURNAL are presented in this special department. The publication will be completed as soon as possible after receipt of the material. The Editorial Committee does not hold itself responsible for the opinions expressed by the correspondents.

An Exact Solution for Two-Dimensional Linear Panel Flutter at Supersonic Speeds

Martin Goland and Yudell L. Luke
Associate Director for Engineering Sciences, and Section Head for Analysis, Respectively, Engineering Division, Midwest Research Institute, Kansas City, Mo.
January 4, 1954

Introduction

SEVERAL WRITERS HAVE RECENTLY GIVEN attention to the calculation of the flutter behavior of a thin panel, such as occurs in wing, tail, or fuselage coverings. In this type flutter, the basic structure supporting the panel acts essentially as if rigid, while the panel vibrates normal to its own plane. In analyzing the phenomenon, the attempts to date have employed the generalized coordinate approach, using the lower normal modes of the panel as coordinates.

In the present note, a theoretically exact solution is deduced for the supersonic flutter of two-dimensional panels of uniform thickness—i.e., uniform plates of infinite width—supported on beams running in the width direction. The supersonic flow is directed normally to the supporting beams and is past one surface of the plate. The fluid on the other side of the plate is stagnant, and it is assumed that its pressure remains sensibly constant. [The flutter of a "flag," with flow past both surfaces of the flag, can be derived from the present results by multiplying the pressure $P(x)$ by the factor 2.]

The present study is restricted to a simply supported panel resting on two rigid beams. However, a straightforward extension of the theory permits taking into account other types of panel end support, beams capable of elastic deflection, and the case of a panel resting on many supports.

In practice, the problem of interest is the panel of finite span, rather than the two-dimensional panel. However, it is hoped that the present analysis and its results will throw light on the mechanisms of this new type of flutter and will thus enable an evaluation to be made of the validity of using a Lagrangian approach to the finite-span panel problem, in which only the first few normal panel modes are used as coordinates.

Equations of Motion

Consider a rectangular panel of great width and of length $2b$, the panel being supported on rigid beams along the two wide edges (i.e., the leading and trailing edges). A supersonic stream with undisturbed velocity V and density ρ passes over one side of the panel, directed normally to the supported edges. The panel is of uniform thickness and composition everywhere.

The elastic behavior of the panel, depending on its rigidity, may fall within the elastic membrane province, may be described by the Bernoulli-Euler bending mechanism, or (in actuality) is a combination of the two. For the present analysis, the integro-differential equations for pure membrane or for pure bending action only are deduced. It will be seen that the technique of solution is essentially the same in both instances. A combination of membrane and bending behavior can also be dealt with without difficulty.

Now let x be a dimensionless coordinate with origin at the leading edge of the panel and running in the stream direction to the trailing edge, where x has the value 2. Since a linear analysis is contemplated, during flutter the panel motion can be described as $z(x, t) = z(x) \cdot b \cdot e^{j\omega t}$. Here b is the panel semichord, ω is the flutter frequency, and t is the time. The dimensionless function $z(x)$ describes the shape of the panel during the flutter motion. In the further work, since the exponential $e^{j\omega t}$ occurs throughout in the usual fashion, it will be omitted from the mathematical development.

Then, for a membrane of mass m per unit area and with a tension T per unit width in the x-direction, it is readily shown that the equation of motion is

$$(T/b)\,(d^2z/dx^2) + m\omega^2 bz = P \tag{1}$$

Here $P = P(x)$ is the excess of pressure caused by the panel deflection, and $z = z(x)$ is taken positive when the panel distorts into the stream. The factors $1/b$ and b in the first and second terms arise from the fact that x and z are nondimensional.

The fundamental natural frequency of the uniform membrane is given by $\omega_n = (\pi/2b)\,(T/m)^{1/2}$, and so Eq. (1) can be put in the alternate form

$$(d^2z/dx^2) + (\pi^2/4)\,(k^2/k_n^2)z = (b/T)P \tag{2}$$

where $k = \omega b/V$ and $k_n = \omega_n b/V$. The boundary conditions for the membrane problem are

$$\text{at } x = 0 \text{ and } x = 2; \quad z = 0 \tag{3}$$

For the plate in bending, a similar derivation of the equation of motion leads to

$$(d^4z/dx^4) - (m\omega^2 b^4/D)\,z = -(b^3/D)P \tag{4}$$

where D is the flexural rigidity of the plate and the other symbols have the same significance as before. The fundamental natural frequency for the simply supported plate is $\omega_n = (\pi^2/4b^2) \times (D/m)^{1/2}$, and so an alternate form for Eq. (4) is

$$(d^4z/dx^4) - (\pi^4/16)\,(k^2/k_n^2)z = -(b^3/D)P \tag{5}$$

where k and k_n are as previously defined. The boundary conditions for the plate problem are

$$\text{at } x = 0 \text{ and } x = 2; \quad z = d^2z/dx^2 = 0 \tag{6}$$

With regard to the pressure $P(x)$, an elegant expression has been given by Miles.[1] Converting from his x-coordinate (running from -1 to $+1$, instead of the present 0 to 2) to the present definition for x, the expression for P is

$$P = \frac{\rho U}{\beta}\left[w(0)\cdot G(x) + \int_0^x G(x-\xi)\cdot\left(\frac{dw}{d\xi} + jkw\right)\cdot d\xi\right] \quad (7)$$

where ρ is the air density, U the speed, M the Mach number, and $\beta^2 = M^2 - 1$. Also,

$$G(x) = e^{-j\kappa Mx}\cdot J_0(\kappa x) \quad (8)$$

$$w = U[(dz/dx) + jkz] \quad (9)$$

where $\kappa = mk/\beta^2$, and $w(0)$ is the value of the downwash w at $x = 0$. (J_0 represents the Bessel function of the first kind.)

Combining Eqs. (2) and (5) with Eq. (7) yields the integrodifferential equations governing the membrane and plate flutter problems.

Solution by Laplace Transforms

The solution for the membrane problem is now given. While the plate problem is not solved explicitly, it will be seen that the procedure is identical with that used for the membrane, both problems being amenable to solution by straightforward Laplace transform techniques.

Combining Eqs. (2) and (7) and noting that $z = 0$ at $x = 0$, the integrodifferential equation to be solved is

$$\frac{d^2z}{dx^2} + \alpha^2k^2z = \gamma\left\{z_{x0}G(x) + \int_0^x G(x-\xi)\cdot\left[\frac{d^2z}{d\xi^2} + 2jk\frac{dz}{d\xi} - k^2z\right]\cdot d\xi\right\} \quad (10)$$

where z_{x0} is the value of dz/dx at $x = 0$, $\alpha^2 = \pi^2/4k_n^2$, and after some manipulation it can be shown that

$$\gamma = (\pi^2/4\beta)\cdot(\rho b/m)\cdot(1/k_n^2) \quad (11)$$

Now let $\bar{z}(p)$ be the Laplace transform of $z(x)$ in the Carslaw and Jaeger notation. Then, using the product theorem, the transformed Eq. (10) becomes, subject to the Eq. (3) boundary conditions,

$$\{p^2 + \alpha^2k^2 - \gamma\bar{G}(p)\cdot(p + jk)^2\}\,\bar{z} = z_{x0} \quad (12)$$

where $\bar{G}(p)$ is the Laplace transform of $G(x)$. It can be shown that

$$\bar{G}(p) = [(p + j\kappa M)^2 + \kappa^2]^{-1/2} \quad (13)$$

and so, after some algebraic manipulation,

$$\bar{z}(p)/z_{x0} = [A(p)/D(p)] + [B(p)/D(p)]\cdot\bar{G}(p) \quad (14)$$

where

$$D(p) = (p^2 + \alpha^2k^2)^2\,[(p + j\kappa M)^2 + \kappa^2] - \gamma^2(p + jk)^4 \quad (15)$$

$$A(p) = (p^2 + \alpha^2k^2)\,[(p + j\kappa M)^2 + \kappa^2] \quad (16)$$

$$B(p) = \gamma(p + jk)^2\,[(p + j\kappa M)^2 + \kappa^2] \quad (17)$$

Now let $F_1(x)$ be the inverse transform of $A(p)/D(p)$. Since $A(p)/D(p)$ is the ratio of polynomials, the inverse transform is readily deduced. Similarly, let $F_2(x)$ be the inverse transform of $B(p)/D(p)$; the latter is again a ratio of polynomials. It then follows that the solution for z is

$$z(x)/z_{x0} = F_1(x) + \int_0^x F_2(\xi)\cdot e^{-j\kappa M(x-\xi)}\,J_0[\kappa(x-\xi)]\,d\xi$$
$$= F_1(x) + \int_0^x F_2(x-\xi)\cdot e^{-j\kappa M\xi}\,J_0(\kappa\xi)\,d\xi \quad (18)$$

subject to the boundary condition $z = 0$ at $x = 2$.

If a flutter solution exists, the manner of arriving at the flutter condition is now evident. For a given set of values for M and ρ (i.e., for a given altitude and Mach Number, so that the U value is also determined), flutter will occur for those k-values that result in $z = 0$ at $x = 2$. The mode shape at flutter is then given by Eq. (18).

If a flutter solution does not exist, there will be no finite k-values that lead to satisfaction of the $x = 2$ boundary condition.

The solution for the beam proceeds in analogous fashion, save that *two* boundary conditions must be satisfied at $x = 2$ in order for flutter to occur.

Analysis of the Results

Unfortunately, the analytic solutions to the membrane and plate problems are too complicated to permit many general conclusions to be drawn concerning the flutter mechanism. Information for practical configurations can be gained only by numerical calculations for specific cases; this is a drawback that evidently characterizes all phases of the flutter problem.

Furthermore, the numerical calculations, even for a single panel, are lengthy. For each combination of panel parameters and ρ, M, and k, the roots of the Eq. (15) polynomial must be determined. The value of Eq. (18) must then be calculated at $x = 2$ to see whether a zero value for $z(2)$ results. If not, further k trials must be attempted. The evaluations of Eq. (18) entail considerable labor because of the convolution integrals involved.

Because of the lengthy character of the numerics, the present authors have been unable to immediately plan any detailed numerical studies. Hence, the reason for this partially complete presentation of the results.

It is of interest to note certain conclusions applicable to the cases where γ is either very small or very large. For γ very small and approaching zero, the solution evidently approaches the case of simple panel vibrations in a vacuum—i.e., vibration in the panel normal modes.

For γ very large, it can be shown that flutter of both the membrane and the plate *cannot occur*. It can be shown by residue theory that, for γ large and for the membrane, the Eq. (18) expression for $z(x)$ reduces to

$$\frac{z(x)}{z_{x0}} = \frac{1}{2}\frac{e^{\gamma x}}{\gamma} + \frac{1}{2}\int_0^x e^{\gamma(x-\xi)}\,e^{-j\kappa M\xi}\,J_0(\kappa\xi)\,d\xi \quad (19)$$

which is of order $e^{\gamma x}/\gamma$. It is evident from Eq. (19) that $z(2)$ cannot be zero for any finite k—i.e., *for large γ a physically feasible flutter mode is nonexistent*. For the plate, a similar result is obtained.

It can also be shown without difficulty that flutter cannot occur for the membrane if the Mach Number M is sufficiently large. However, the lower boundary on M has not been determined.

It is thus seen that panel flutter does not exist for all configurations. The precise flutter boundaries must be determined through detailed numerical study.

Reference

[1] Miles, J. W., *The Aerodynamic Forces on an Oscillating Air Foil at Supersonic Speeds*, Journal of the Aeronautical Sciences, Vol. 14, No. 6, pp. 351-358, June, 1947.

Nose Shapes for Minimum Pressure Drag at Supersonic Mach Numbers

Leland H. Jorgensen

Aeronautical Research Scientist, Ames Aeronautical Laboratory NACA, Moffett Field, Calif.

January 6, 1954

Introduction

Nose shapes theoretically optimized for minimum pressure drag for given fineness ratio have been derived by Newton[1, 2] and von Kármán.[3] Because of the assumptions made in the derivations, one might expect the Newtonian shape to have minimum drag for hypersonic Mach Numbers and the von Kármán shape to have minimum drag for high fineness ratios and

low supersonic Mach Numbers. However, for moderate fineness ratios and moderate supersonic Mach Numbers, one might expect that other shapes are possible which have less drag than either the Newtonian or the von Kármán. It is the purpose of this note to present the derivation of several such nose shapes and to compare their profiles and drags with those for the Newtonian and von Kármán shapes. The derivation is accomplished by the use of an equation for calculating pressure distributions developed by Bolton-Shaw and Zienkiewicz.[4]

Symbols

B = a constant, $1.117M_0$
C = defined by Eq. (10)
C_D = pressure-drag coefficient, $D/q_0\pi y_2^2$
D = pressure drag
I_D = defined by Eq. (4)
M = Mach Number
p = static pressure
p_t = total pressure
q = dynamic pressure
x, y = coordinates with origin at vertex
y', y'' = dy/dx and d^2y/dx^2, respectively
$x_2/2y_2$ = fineness ratio
Z = By'

Subscripts

0 = free-stream conditions
1 = values at vertex
2 = values at base

Derivation of Nose Shapes

The pressure-distribution equation of Bolton-Shaw and Zienkiewicz may be expressed as

$$p/p_0 = 1.014e^n \tag{1}$$

where

$$n = 1.405\,M_0y' - 0.288\,M_0\sqrt{y'^2 - 2yy''} - \frac{0.157y'}{\sqrt{y'^2 - 2yy''}} \tag{1a}$$

By derivation, this equation is valid for computing pressure distributions over shapes (not too dissimilar from circular-arc ogives) for which the Mach Number divided by the fineness ratio is between about 0.5 and 1. For fineness ratio 3 and Mach Numbers between 1.5 and 3, pressure distributions computed by Eqs. (1) and (1a) for an approximate Newtonian shape and for a von Kármán shape agree well with those computed by Van Dyke's second-order theory[5] (see Fig. 1). (The approximate Newtonian shape, defined by $y = y_2(x/x_2)^{3/4}$, was suggested by A. J. Eggers, of the Ames Aeronautical Laboratory.) It is also observed in Fig. 1 that there is little or no loss in the accuracy of the pressure distributions computed by Eq. (1) if terms containing y'' in Eq. (1a) are omitted—that is, if Eq. (1a) is reduced to

$$n = 1.117M_0y' - 0.157 \tag{1b}$$

This simplification greatly aids the derivation procedure and is justified on the basis of the pressure-distribution comparisons in Fig. 1.

The pressure drag of a given nose shape may be expressed in coefficient form by

$$C_D\frac{q_0}{p_0} = \frac{D}{q_0\pi y_2^2}\left(\frac{q_0}{p_0}\right) = \frac{2}{y_2^2}\int_{x_1}^{x_2}\left(\frac{p - p_0}{p_0}\right)yy'\,dx \tag{2}$$

Substituting Eqs. (1) and (1b) into Eq. (2) yields

$$C_D\frac{q_0}{p_0} = \frac{1}{y_2^2}\left(\frac{2.028}{e^{0.157}}\right)\int_{x_1}^{x_2} e^{By'}yy'\,dx + \left(\frac{y_1}{y_2}\right)^2 - 1 \tag{3}$$

where $B = 1.117M_0$.

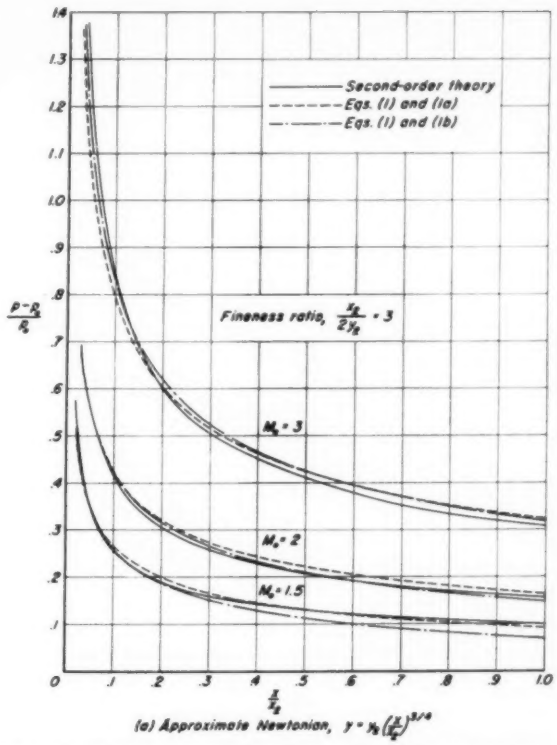

(a) Approximate Newtonian, $y = y_2(x/x_2)^{3/4}$

Fig. 1.- Comparison of pressure distributions computed by various methods.

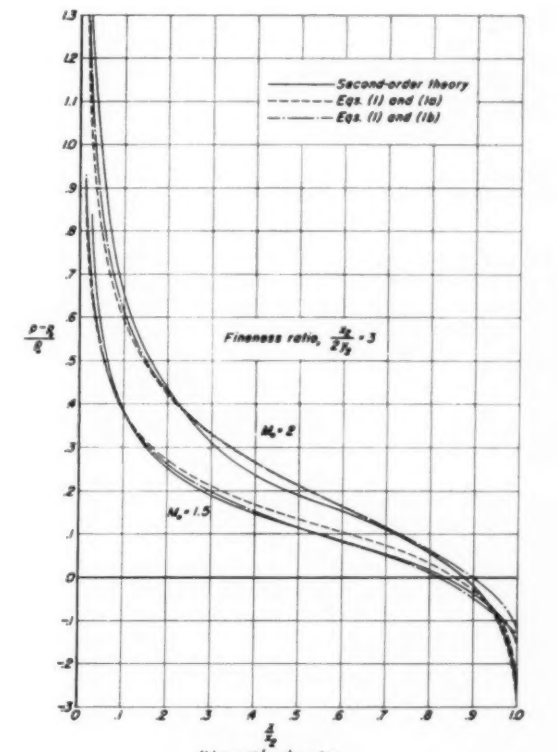

(b) von Kármán ogive

Fig. 1.- Concluded.

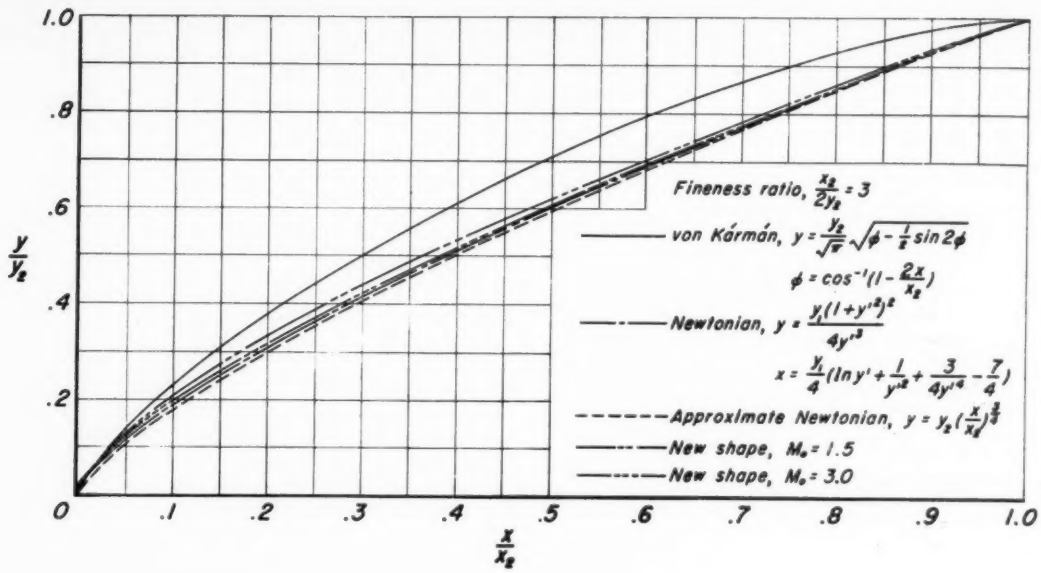

Fig. 2.– Comparisons of profiles of minimum drag noses for given length and base diameter.

As becomes apparent later, it is convenient at this point to express the total pressure drag as the sum of the pressure drag on a finite area of infinite slope at the vertex plus the pressure drag over the remaining profile. Taking the pressure drag at the vertex as $D_1 = p_{t_1}\pi y_1^2$, the equation to be minimized may be written as

$$I_D = \left(C_D \frac{q_0}{p_0} + 1\right)\left(\frac{e^{0.157}}{2.028}\right) y_2^2 = \frac{e^{0.157}}{2.028}\left(\frac{p_{t_1}}{p_0} + 1\right) y_1^2 + \int_{x_1}^{x_2} e^{By'} yy'\, dx \quad (4)$$

Since the integrand function, $e^{By'}yy'$, is independent of x, the first integral of Euler's equation yields

$$Byy'^2\, e^{By'} = \text{const.} \quad (5)$$

If one of the extreme points (y_1 or y_2) is on the x-axis and $y'^2e^{By'}$ is not infinite, then no usable solution is obtained. This same condition arises in the Newtonian analysis. With y_2 fixed, however, y_1 may be obtained by satisfying the terminal condition that[6]

$$\left\{\frac{\partial}{\partial y}(e^{By'}yy') - \frac{d}{dy}\left[\frac{e^{0.157}}{2.028}\left(\frac{p_{t_1}}{p_0} + 1\right) y^2\right]\right\}_{y=y_1} = 0 \quad (6)$$

By letting $Z = By'$, $Z_1 = By_1'$, and $Z_2 = By_2'$, Eq. (6) reduces to

$$e^{Z_1}(Z_1 + 1) = \frac{e^{0.157}}{1.014}\left(\frac{p_{t_1}}{p_0} + 1\right) \quad (7)$$

where

$$\frac{p_{t_1}}{p_0} = \left(\frac{6M_0^2}{5}\right)^{7/2}\left(\frac{7M_0^2 - 1}{6}\right)^{-5/2} \quad (7a)$$

Eq. (5) may be written as

$$y = (Z_2^2 y_2 e^{Z_2}) Z^{-2} e^{-Z} \quad (8)$$

Since

$$x = \int \frac{dy}{y'} = B\int \frac{dy}{Z}$$

then,

$$x = -(Z_2^2 y_2 e^{Z_2})\frac{B}{6}\left[\ln Z - Z + \frac{Z^2}{4} - \frac{Z^3}{18} + \frac{Z^4}{96} + \cdots + e^{-Z}\left(\frac{1}{Z} - \frac{1}{Z^2} - \frac{4}{Z^3}\right) + C\right] \quad (9)$$

When $x = x_1 = 0$, $y = y_1 \neq 0$, $Z = Z_1 \neq 0$, therefore,

$$C = -\ln Z_1 + Z_1 - \frac{Z_1^2}{4} + \frac{Z_1^3}{18} - \frac{Z_1^4}{96} - e^{-Z_1}\left(\frac{1}{Z_1} - \frac{1}{Z_1^2} - \frac{4}{Z_1^3}\right) \quad (10)$$

Minimum-drag nose shapes can be computed by the following steps:

(1) For given M_0, solve for Z_1 by Eqs. (7) and (7a).

(2) Solve for C by Eq. (10).

(3) For given fineness ratio $x_2/2y_2$, solve for Z_2 using Eq. (9).

(4) For values of Z from Z_1 to Z_2, solve for corresponding values of y/y_2 using Eq. (8) and values of x/y_2 or x/x_2 using Eq. (9).

Profile and Pressure-Drag Comparisons

Nose shapes resulting from the use of the previously derived equations are a function of both Mach Number and fineness ratio. Although the condition of vertex bluntness is imposed, this bluntness is generally small, y_1/y_2 being less than about 2 per cent for fineness ratios of 3 and greater. For most pressure-drag calculations, the drag contribution of the blunt vertex is negligible.

Nose profiles, computed for a fineness ratio of 3 and for Mach Numbers of 1.5 and 3, are compared with the Newtonian and von Kármán profiles in Fig. 2. (Also shown for comparison is the three-quarter-power profile which closely approximates the Newtonian.) It is evident that the new shapes, although lying between the Newtonian and von Kármán, are in best agreement with the Newtonian shape. In fact, there is little difference between the new shape for $M_0 = 3$ and the Newtonian shape. All of the shapes have infinite slopes at their vertices, and all, except the von Kármán, have finite base slopes.

Pressure-drag coefficients computed by second-order theory for the various shapes are compared in Table 1.

TABLE 1

Fineness Ratio 3 Shapes	C_D $M_0 = 1.5$	$M_0 = 2$	$M_0 = 3$
New shapes	0.0845	0.0773	0.0686
Newtonian	0.0877	0.0778	0.0689
von Kármán	0.0895	0.0857	...

It is interesting to note that the pressure-drag differences between the shapes at a given Mach Number are small. Thus, for most design purposes, any one of these shapes may be considered for a minimum-drag nose.

REFERENCES

[1] Newton, Isaac, *Principia—Motte's Translation Revised*, Univ. of Calif. Press, pp. 333, 657–661, 1946.

[2] Todhunter, I., *Researches in the Calculus of Variations*, G. E. Stechert, New York, pp. 167–173, Reprint 1924.

[3] von Kármán, Th., *The Problem of Resistance in Compressible Fluids*. GALCIT Pub. No. 75, 1936. (From Roma Reale Accad. d'Italia, Vol. XIV, 1936.)

[4] Bolton-Shaw, B. W., and Zienkiewicz, H. K., *The Rapid, Accurate Prediction of Pressure on Non-Lifting Ogival Heads of Arbitrary Shape, at Supersonic Speeds*, English Electric Co. Rept. L. A. t.034, June, 1952.

[5] Van Dyke, Milton D., *Practical Calculation of Second-Order Supersonic Flow Past Nonlifting Bodies of Revolution*, NACA TN No. 2744, 1952.

[6] Courant, R., and Hilbert, D., *Methoden der Mathematischen Physik*, Vol. 1, pp. 179–180, Julius Springer, Berlin, 1931.

Streamline Curvature Effects for Finite Wings in Wind Tunnels

Alan Pope

Supervisor, Experimental Aerodynamics Division, The Sandia Corporation, Albuquerque, N.M.

September, 1953

SUMMARY

A method of applying the Lotz τ correction to wings is outlined, suitable for the case of finite span wings in wind tunnels.

INTRODUCTION

THE CASE OF STREAMLINE CURVATURE EFFECTS for two-dimensional models has been discussed by Glauert[1] and Allen and Vincenti.[2] The case for large models of finite span has been covered by Sivells and Deters[3] and Swanson and Toll.[4] However, the methods presented in the last two references require several hours to solve, and a simpler correction of adequate accuracy seems worth while.

GENERAL THEORY

The basis for a streamline curvature effect is found in the variation (along the chord) of the upwash induced by the tunnel boundaries. Numerical values of this variation for reasonable wings in reasonable wind tunnels indicates that the angle induced by the upwash varies almost linearly along the chord, so that to all intents and purposes the wing in a wind tunnel is in a circularly bent flow, or, conversely, the wing has had added to it the loading on a circular arc airfoil whose curvature and angle of attack corresponds to the boundary induced curvature of the flow.

The circular arc airfoil[5] has the following characteristics of interest to this specific problem: First, its loading is composed of a flat plate loading and an elliptic loading. The portion that is a flat plate loading is proportional to the angle of attack between the "horizontal" chord line and the relative wind. The elliptic loading is proportional to the amount of camber, which in turn defines the angle of zero lift. Since the angle of zero lift is essentially the slope of the circular arc airfoil at its three-quarter point, the elliptic correction is defined by the *difference* between the boundary induced upwash at the half-chord (where the slope is parallel to the chord) and at the three-quarter chord. The flat-plate correction, which has no moment about the quarter-chord point, is defined by the *difference* in boundary induced upwash at the quarter-chord and that at the half-chord. The upwash *at* the quarter-chord is covered in the customary wall connections written in the form

$$\Delta\alpha = \delta(S/C)\, C_L \quad (57.3)$$
$$\Delta C_D = \delta(S/C)\, C_L^2$$

where

S = wing area
C = tunnel cross-sectional area
δ = factor based on model span and tunnel shape

Since the variation of boundary induced angle is linear, the variation between quarter- and half-chord is the same as that between half- and three-quarter chord. Hence, once we find the (flat plate) angle of attack correction for streamline curvature $\Delta\alpha_{sc}$, the additive (elliptical loading) lift correction will be

$$\Delta C_{L_{sc}} = -\Delta\alpha_{sc} \cdot a$$

where a = slope of the wing lift curve (either measured or theoretical is satisfactory), and the additive moment correction (since the moment of an elliptic load is zero about the half-chord) is

$$\Delta C_{m(c/4)sc} = -0.25\Delta C_{L_{sc}}$$

From the above corrections, we see that the finite wing in a closed tunnel acts like a wing with excessive camber at an excessive angle of attack. The additive corrections increase the measured angle of attack to account for the angle change and reduce the lift and negative moment.

The method for obtaining the numerical values for the streamline curvature effect is that given by Lotz,[6] who expresses the downwash aft of the wing lifting line (assumed at the quarter-chord) according to

$$\tau = \frac{\text{additional boundary induced upwash aft of quarter-chord line}}{\text{boundary induced upwash at quarter-chord line}}$$

The value of the additive angular correction is then

$$\Delta\alpha_{sc} = \tau\Delta\alpha$$

Values of τ are given in Figs. 1 and 2 (replotted from references 6 and 9) for a wide number of tunnel cross sections and model spans. The "tail length" used for wings should be one-fourth of the M.A.C. (Additional values in reference 9.)

The size of $\Delta\alpha_{sc}$ is usually negligible (around $0.03C_L$) for wings of high aspect ratio. For reflection plane models or low aspect ratio models, it can rise to $0.3C_L$ or more and becomes large enough for inclusion.

EFFECT OF COMPRESSIBILITY

The effect of compressibility on the wing streamline curvature correction is to increase the effective chord by $1/\sqrt{1 - M^2}$. This increased length should be used in determining τ. In many cases the streamline curvature correction at near sonic speeds can exceed 0.5°.

Example: Find the streamline curvature correction at low speed and $M = 0.85$ for a wall mounted semispan panel model having the following dimensions: Panel span 7.00 ft., wing area 32.67 sq.ft., M.A.C. = 2.46 ft., taper ratio = 0.5, wing aspect ratio = 6.0, airfoil = 65-006. 7- by 10-ft. tunnel.

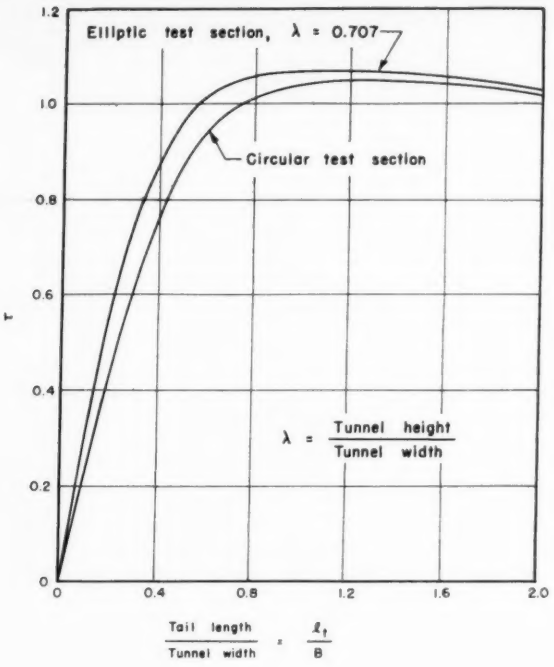

FIGURE 1

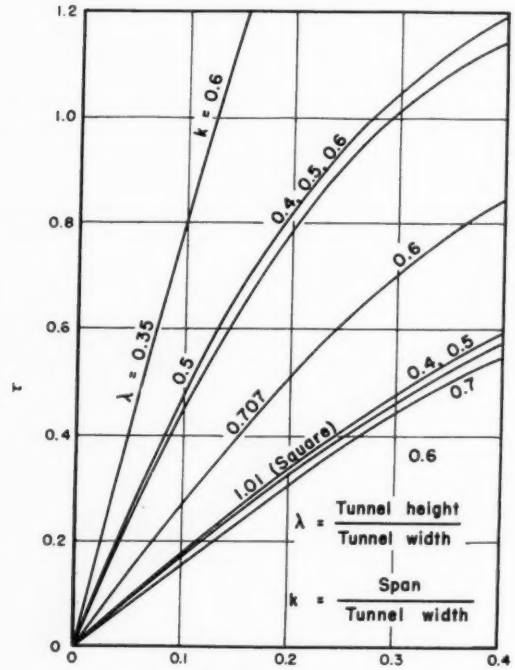

FIGURE 2

(1) From page 22 of reference 4 the boundary induced upwash at the wing results in an angular correction of

$$\Delta\alpha = 1.078C_L$$

(2) From Fig. 2, using an extrapolated value for a tunnel height-width ratio of 0.35 and a "tail length" of 2.46/4 = 0.615, $l_t/B = 0.615/20 = 0.0307$, and $\tau = 0.25$,

$$\Delta\alpha_{sc} = (0.25)\,(1.078C_L) = 0.269C_L$$

(3) A similar example using the unit vortex approach (page 22 of reference 4) yields a value of $0.254C_L$. The difference of 0.015° (at $C_L = 1.0$) is not surprising in view of the uncertainties of the extrapolation and the fact that reference 4 uses an average value rather than that at the centerline. Better agreement would reasonably be expected for a floor mounted model, since the tunnel shape would then be more reasonable.

(4) At $M = 0.85$,

$$l_t/B(1 - M^2)^{1/2} = 0.0307/[1 - (0.85)^2]^{1/2} = 0.0583$$

and $\tau = 0.475$. $\Delta\alpha_{sc}$ then equals $(0.475)\,(1.078C_L) = 0.513C_L$.

References

[1] Glauert, H., *Wind Tunnel Interference on Wings, Bodies and Airscrews*, R. and M. 1566, 1933.

[2] Allen, H. Julian, and Vincenti, Walter G., *Wall Interference in a Two-Dimensional-Flow Wind Tunnel with Consideration of the Affect of Compressibility*, NACA TR No. 782, 1944.

[3] Sivells, James C., and Deters, Owen J., *Jet-Boundary and Planform Corrections for Partial-Span Models with Reflection Plan, End Plate or No End Plate in a Closed Circular Wind Tunnel*, NACA TR No. 843, 1946.

[4] Swanson, Robert S., and Toll, Thomas A., *Jet-Boundary Corrections for Reflection Plane Models in Rectangular Wind Tunnels*, NACA TR No. 770, 1943.

[5] Pope, Alan, *Basic Wing and Airfoil Theory*, p. 110; McGraw-Hill Book Company, Inc., New York, 1951.

[6] Lotz, I., *Corrections of Downwash in Wing Tunnels of Circular and Elliptic Sections*, NACA TM No. 801, 1936.

[7] Silverstein, Abe, and Katzoff, S., *Experimental Investigation of Wind Tunnel Interference on Downwash behind an Aerofoil*, NACA TR No. 609, 1937.

[8] Pope, Alan, *Wind Tunnel Testing*; John Wiley & Sons, Inc., New York, 1947.

[9] Silverstein, Abe, *Wind Tunnel Interference with Particular Reference to Off-Center Positions of the Wing and to the Downwash at the Tail*, NACA TR No. 547, 1935.

Wind-Tunnel Model Position for Transonic Testing

Alan Pope

Supervisor, Experimental Aerodynamics Division, The Sandia Corporation, Albuquerque, N.M.

January 4, 1954

IT APPEARS THAT KEEPING a wind-tunnel model exactly on the tunnel centerline is much more important for transonic testing than for subsonic or supersonic testing, since unsymmetric wave reflections may cause serious errors in pitching moment measurements. The transonic case differs from the supersonic one in that the structure of the detached shock and its reflection cannot be computed, and, hence, the Mach Number range in which trouble may be expected can only be obtained empirically.

The situation is as follows:

Consider a body in a transonic wind tunnel at a very low supersonic Mach Number (Fig. 1), and let its location be closer to the floor than the ceiling. The bow shock wave reflected from the floor will strike the body further forward than will the shock reflected from the ceiling, and a nose-down pitching moment will appear that would not occur in free flight. This extraneous pitching moment becomes larger when one wave completely

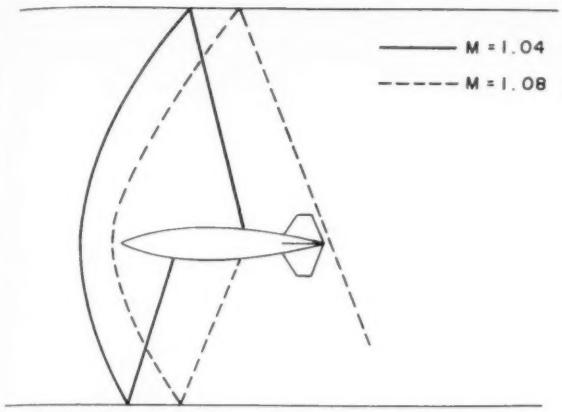

FIG. 1. Bow shock pattern for model low in wind tunnel.

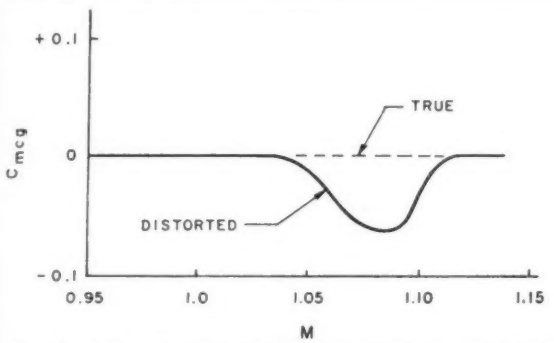

FIG. 2. Distortion of pitching motion curve by asymmetrical transonic reflection, model low in tunnel. The strength, shape, and extent of the distortion vary for every model-tunnel combination.

misses the body (see dotted lines in Fig. 1) largely because the asymmetric pressure is then farthest from the center of gravity.

A moment curve for a finned body of revolution is shown in Fig. 2 for one case that resulted in a maximum erroneous trim of 17° angle of attack. Visual observation methods were finally used to determine the region of reflection free data.

While the region and magnitude of the detached shock reflection phenomenon vary for each model-tunnel combination, it appears safe to conclude that transonic detached shock reflection errors will not be serious with regard to lift and drag, that their pitching moment contribution may be minimized by keeping the model on the tunnel centerline, and that the Mach range in which they exist must be determined by visual or other empirical methods.

Similar Solutions of Compressible Laminar Boundary-Layer Equations

Clarence B. Cohen
Aeronautical Research Scientist, Lewis Flight Propulsion Laboratory, NACA, Cleveland, Ohio
January 11, 1954

IN A RECENT NOTE,[1] Drs. Li and Nagamatsu treated the compressible laminar boundary-layer equations having similarity-type solutions. It was indicated that four classes of solutions are possible. In the present note transformations are given which reduce three of these classes to only one, and the remaining class is also discussed.

In reference 1, the boundary-layer equations resulting from application of Stewartson's transformation[2] were subjected to the similarity requirements:

$$\left.\begin{aligned} \psi &= Z^a V_1^p f(\eta) \\ S &= S_w g(\eta) \\ Y &= \eta Z^b V_1^q \end{aligned}\right\} \tag{1}$$

where

V_1 = transformed free-stream velocity
S = $(H/H_1) - 1$
H = stagnation enthalpy
(Z, Y) = transformed longitudinal and normal coordinates, respectively

This led to the system of ordinary differential equations,

$$\left.\begin{aligned} f''' &= K_1 f'^2 - K_2 f f'' - K_3(1 + S_w g) \\ g'' &+ K_2 f g' = 0 \end{aligned}\right\} \tag{2}$$

with the boundary conditions

$$\begin{aligned} f(0) = f'(0) = 0, \quad g(0) = 1 \\ \eta \to \infty, \quad f' \to K_6, \quad g \to 0 \end{aligned} \tag{3}$$

Four classes of similarity resulted, corresponding to four combinations of a, b, p, and q. These classes were distinguished by their external-velocity distributions, differential equations, and boundary conditions, all involving various parameters, K_i. [For class (3) the given definitions of K_2 and K_6 were incomplete.] The velocity distributions were as follows:

$$\left.\begin{aligned} &\text{Class (1):} \quad V_1 = [(1 + 2q)(K_3 Z + C)]^{1/(1+2q)} \\ &\text{Class (2):} \quad V_1 = Ce^{K_1 Z} \\ &\text{Class (3):} \quad V_1 = (K_9/m) Z^m \\ &\text{Class (4):} \quad V_1 = CZ^{K_5} \end{aligned}\right\} \tag{4}$$

The differential equations and boundary conditions of classes (1) and (3) can, however, be reduced to those of class (4) by the following transformations:

$$\left.\begin{aligned} &\text{Class (1)} \begin{cases} f_4 &= f_1 \sqrt{(1 + 2q_1)K_{1,1}} \\ \eta_4 &= \eta_1 \sqrt{(1 + 2q_1)K_{1,1}} \\ K_{3,4} &= (1 + 2q_1)^{-1} \end{cases} \\ &\text{Class (3)} \begin{cases} f_4 &= f_3 (K_{6,3})^{(2p_3 - 1)/2(q_3 - p_3 + 1)} \\ \eta_4 &= \eta_3 (K_{6,3})^{(2q_3 + 1)/2(q_3 - p_3 + 1)} \end{cases} \end{aligned}\right\} \tag{5}$$

where the last subscript on any quantity identifies the class in which that quantity is defined.

Class (4) itself can be reduced further through the following transformation:

$$\left.\begin{aligned} \bar{f} &= f_4 \sqrt{(K_{3,4} + 1)/2} \\ \bar{\eta} &= \eta_4 \sqrt{(K_{3,4} + 1)/2} \\ S &= S_w g_4 \end{aligned}\right\} \tag{6}$$

and the corresponding external velocity can be written

$$V_1 = C(Z - Z_0)^m \tag{6a}$$

The resulting system of equations is

$$\left.\begin{aligned} \bar{f}''' + \bar{f}\bar{f}'' &= \beta(f'^2 - 1 - S) \\ S'' + \bar{f}S' &= 0 \\ \bar{f}(0) = \bar{f}'(0) = 0, \quad S(0) &= S_w \\ \bar{f}'(\infty) = 1, \quad S(\infty) &= 0 \end{aligned}\right\} \tag{7}$$

which is identical with the system developed in reference 2. Thus, class (2) remains the only distinct similarity type.

Class (2) is a limiting case of class (4) which, however, cannot be obtained by transformation alone from class (1), (3), or (4), but arises from considering the special combination: $a = b =$

0, $p = 1/2$, $q = -1/2$ in Eqs. (1). This corresponds to the case $K_{3,4} \to \infty$ of case (4) and can be reduced to the form of Eqs. (7) with $\beta = 2.0$ by the transformation

$$\left.\begin{aligned} \bar{f} &= f_2 \sqrt{K_1/2} \\ \bar{\eta} &= \eta_2 \sqrt{K_1/2} \\ S &= S_w g \end{aligned}\right\} \tag{8}$$

where $K_1 > 0$ (favorable pressure gradient).

For $K_1 < 0$ (unfavorable gradient) the same transformation, but with $(-K_1)$ replacing (K_1), gives the same boundary conditions, but applied to the new system

$$\bar{f}''' = f\bar{f}'' - 2(\bar{f}'^2 - 1 - S) \tag{9a}$$

$$S'' + \bar{f}S' = 0 \tag{9b}$$

From an examination of the right member of Eq. (9a) for $S = 0$ (the insulated-wall case) in the neighborhood of $f' = 1$, it can be seen that no solution that does not indefinitely oscillate about $f' = 1$ is possible. No such simple conclusions have been deduced for the case with heat transfer, which thus may be a distinct case.

References

[1] Li, Ting-Yi, and Nagamatsu, Henry T., *Similar Solutions of Compressible Boundary Layer Equations*, Readers' Forum, Journal of the Aeronautical Sciences, Vol. 20, September, 1953.

[2] Stewartson, K., *Correlated Incompressible and Compressible Boundary Layers;* Proceedings Royal Soc., Vol. A200, 1949.

The Method of Superposition of Planar Wave Systems

Wallace D. Hayes*
Office of Naval Research, London, England
January 7, 1954

THE PURPOSE OF THIS NOTE is to show the solution of a linearized supersonic flow problem by means of the method of the superposition of planar wave systems. The equation for the velocity potential is taken in the form

$$\phi_{xx} + \phi_{yy} - \phi_{zz} = 0 \tag{1}$$

after the application of the Prandtl-Glauert transformation and z is taken in the downstream direction. The problem of interest is to determine the potential at a point in the upper half space (for which $y > 0$), with no incoming waves (null initial conditions), and with ϕ_y given on the upper side of the plane $y = 0$.

The solution to this problem has been obtained by Clarkson[1] and may be expressed

$$\phi(x_0, y_0, z_0) = -\frac{1}{\pi}\int\int_\Gamma \phi_y(x, 0, y)\,\frac{dx\,dz}{R} \quad (y_0 > 0) \tag{2}$$

where R is given by

$$R = \sqrt{(z_0 - z)^2 - (x_0 - x)^2 - y_0^2} \tag{3}$$

and Γ is the region on the plane $y = 0$ for which $(z_0 - z) > 0$ and R is real. Clarkson used the mathematically elegant method of Riesz; the result may also be obtained by other methods. The method of this note is based on the concept that the solution in a singularity-free region, under certain reasonable conditions, may be represented as the superposition of planar wave systems, the superposition consisting of an integration over the wave orientation angle θ as a parameter. In the present example the limitation to the upper half space with no incoming waves limits θ to a range of π, and the general solution may be expressed

$$\phi(x, y, z) = \int_0^\pi f(z - x\cos\theta - y\sin\theta, \theta)\,d\theta \tag{4}$$

In terms of the general solution of Eq. (4) the normal derivative on the plane $y = 0$ takes the form

$$\phi_y(x, 0, z) = -\int_0^\pi f'(z - x\cos\theta, \theta)\sin\theta\,d\theta \tag{5}$$

and the integral appearing in Eq. (2) may be expressed

$$-\frac{1}{\pi}\int\int_\Gamma \phi_y\,\frac{dx\,dz}{R} = \int_0^\pi F(x_0, y_0, z_0, \theta)\,d\theta \tag{6}$$

where

$$F = \frac{1}{\pi}\int\int_\Gamma f'(z - x\cos\theta, \theta)\,\frac{\sin\theta}{R}\,dx\,dz \tag{7}$$

The transformation is now made

$$-\zeta = (z_0 - z) - (x_0 - x)\cos\theta \tag{8a}$$

$$\sqrt{\zeta^2 - y_0^2\sin^2\theta}\cos\psi = (x_0 - x) - (z_0 - z)\cos\theta \tag{8b}$$

for which the functional determinate may be shown to be

$$J\begin{pmatrix}\psi, & \zeta\\ x, & z\end{pmatrix} = \frac{\sin\theta}{R} \tag{9}$$

The region Γ' corresponds to the inequalities

$$0 \leqq \psi \leqq \pi; \quad -\infty < \zeta \leqq -y_0\sin\theta \tag{10}$$

The function F may now be evaluated

$$F = \frac{1}{\pi}\int_{-\infty}^{-y_0\sin\theta}\int_0^\pi f'(z_0 - x_0\cos\theta + \zeta, \theta)\,d\psi\,d\zeta$$

$$F = f(z_0 - x_0\cos\theta - y_0\sin\theta, \theta) \tag{11}$$

whence the desired result Eq. (2) follows immediately from Eqs. (4) and (6).

In case $y_0 = 0$, a much simpler transformation may be used, in which the variable z is retained and ψ is defined by

$$\cos\psi = (x_0 - x)/(z_0 - z) \tag{12}$$

In the ensuing analysis the relation

$$\int_0^\pi \frac{d\psi}{1 - \cos\theta\cos\psi} = \frac{\pi}{\sin\theta} \tag{13}$$

is used.

Reference

[1] Clarkson, M. H., *A Second-Order Theory for Three-Dimensional Wings in Supersonic Flow*, Defense Research Lab. Report No. DRL-332, University of Texas, May 1, 1953. To be published in Quart. Jour. Math. Appl. Mech.

Comments on "Ripple-Type Buckling of Sandwich Columns"[1]

Paul Seide
Research Engineer, Structural Research Group, Northrop Aircraft, Inc., Hawthorne, Calif.
December 21, 1953

IN A RECENT PAPER,[1] Eringen concludes that wrinkling of sandwich columns will take place in neither the symmetric nor the antisymmetric modes found by other writers but in an asymmetric mode. The author also emphasizes that the solution of a two-dimensional mixed boundary value problem of elasticity for a rectangular orthotropic medium, as reported in his Doctoral

* Scientific Liaison Officer. The opinions expressed here are those of the writer and do not necessarily reflect those of the U.S. Navy.

Dissertation,[2] is necessary. The writer has only recently had the opportunity to read this paper in detail and has come to the conclusion that neither of the author's statements is correct for the problem solved. In addition, an effect that may be important has been neglected. The following derivation will indicate the defects of the author's presentation.

In order for the problem under consideration to be in the form of an eigenvalue problem and to have a reasonably simple solution, it must be stated as follows:

A sandwich column is compressed into a state of uniform axial strain (Fig. 1). Prior to buckling, there is no friction between the load applying mechanism and the ends of the core so that movement of the ends perpendicular to the middle surface of the core is permitted. After buckling, no further movement of the ends perpendicular to the middle surface of the core is permitted, and the axial load applied to the structure remains constant. A similar device was used in reference 3 to simplify the problem treated there. Other formulations of the problem will result in formidable complications of the final results. The faces of the sandwich are of equal thickness and of the same material. It is assumed that they may be analyzed by the usual methods of elementary beam theory. The core is an orthotropic elastic medium.

If the destabilizing effect of axial forces in the core is neglected, stresses and displacements in the core are subject to the following boundary conditions:

$$v(0, y) = v(L, y) = 0 \tag{1}$$

$$\sigma_x(0, y) = \sigma_x(L, y) = 0 \tag{2}$$

$$\frac{1}{12} E_f t^3 \frac{\partial^4 v(x, h/2)}{\partial x^4} + \sigma_{cr} t \frac{\partial^2 v(x, h/2)}{\partial x^2} - \frac{t}{2} \frac{\partial \tau_{xy}(x, h/2)}{\partial x} + \sigma_y\left(x, \frac{h}{2}\right) = 0 \tag{3}$$

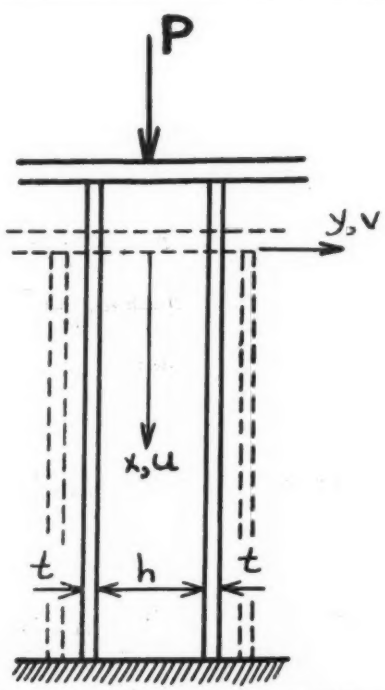

FIG. 1. Sandwich column prior to buckling.

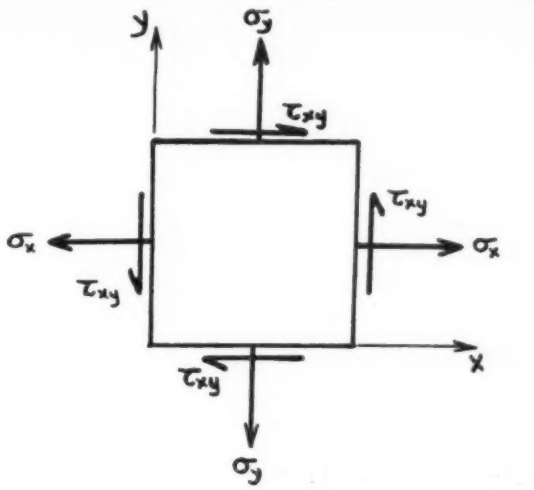

FIG. 2. Positive directions of core stresses.

$$\frac{1}{12} E_f t^3 \frac{\partial^4 v(x, -h/2)}{\partial x^4} + \sigma_{cr} t \frac{\partial^2 v(x, -h/2)}{\partial x^2} - \frac{t}{2} \frac{\partial \tau_{xy}(x, -h/2)}{\partial x} - \sigma_y\left(x, -\frac{h}{2}\right) = 0 \tag{4}$$

$$\frac{t}{2} \frac{\partial^2 v(x, h/2)}{\partial x^2} + \frac{1}{E_f t} \int_0^x \tau_{xy}\left(x, \frac{h}{2}\right) dx - \frac{\partial u(x, h/2)}{\partial x} = 0 \tag{5}$$

$$\frac{t}{2} \frac{\partial^2 v(x, -h/2)}{\partial x^2} + \frac{1}{E_f t} \int_0^x \tau_{xy}(x, -h/2)\, dx + \frac{\partial u(x, -h/2)}{\partial x} = 0 \tag{6}$$

where u, v, σ_x, σ_y, and τ_{xy} are displacements and stresses in the core, in addition to those existing prior to buckling (Figs. 1 and 2).

Conditions (1) and (2) for the ends of the sandwich column indicate the stated assumptions that no further displacements perpendicular to the middle surface of the core are permitted to take place and that the axial load applied to the column remains constant. These are identical with Eringen's boundary conditions for the ends.

Conditions (3) and (4) imply continuity of the faces and core in the direction perpendicular to the middle surface of the core. An error has been made in reference 1 in the formulation of these conditions, as will be shown, and leads to the deduction of an asymmetric mode of wrinkling. In Eqs. (6) of reference 1, which correspond to Eqs. (4) and (5) of the present note, both $\sigma_y(x, 0)$ [$= \sigma_y(x, -h/2)$ of the present note] and $\sigma_y(x, t)$ [$= \sigma_y(x, h/2)$ of the present note] have the same sign. However a positive value of σ_y acts *downward* on the upper face and *upward* on the lower face so that the faces are bent in opposite directions (see Figs. 2 and 3). With $v(x, h/2)$ and $v(x, -h/2)$ both having the same positive direction, it is readily seen that $\sigma_y(x, h/2)$ and $\sigma_y(x, -h/2)$ [or $\sigma_y(x, 0)$ and $\sigma_y(x, t)$] should have *opposite* signs. Positive values of the shear stress, on the other hand, act in opposite directions, but one is applied to the *bottom* of one face while the other acts on the *top* of the other face so that their effect is the same.

Conditions (5) and (6) imply continuity of the faces and core in the direction parallel to the middle surface of the core and are similar in concept to Eq. (A10) of reference 3. The first term in each represents the face strain due to bending, at the juncture of the face and core; the second term represents the face middle surface strain due to the shear stresses transmitted between the core and faces; the third term represents the core strain at the

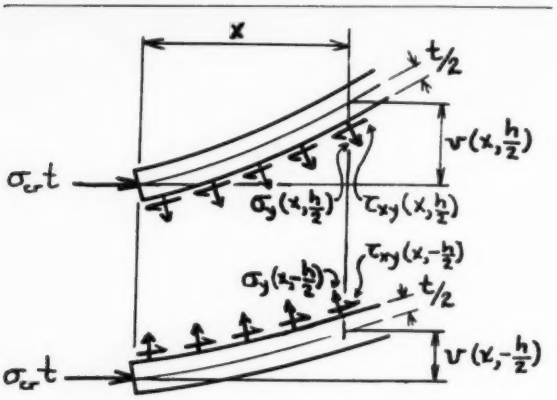

FIG. 3. Forces acting on top and bottom faces.

juncture of the core and faces. The sign difference in these two equations is due to strains being taken at the bottom of one face and top of the other. In most previous work, the first two terms have been neglected, and the conditions have been written as

$$u(x, h/2) \text{ or } (\partial u/\partial x)\,(x, h/2) = 0 \tag{7}$$

$$u(x, -h/2) \text{ or } (\partial u/\partial x)\,(x, -h/2) = 0 \tag{8}$$

Additional conditions that are specified are that the ends of the faces are simply supported—that is,

$$\frac{\partial^2 v\left(0, \frac{h}{2}\right)}{\partial x^2} = \frac{\partial^2 v\left(0, -\frac{h}{2}\right)}{\partial x^2} = \frac{\partial^2 v\left(L, \frac{h}{2}\right)}{\partial x^2} = \frac{\partial^2 v\left(L, -\frac{h}{2}\right)}{\partial x^2} = 0 \tag{9}$$

The solution of the problem as next given is similar to that of reference 4.

The stress-strain relations in the orthotropic core are given by

$$\left.\begin{aligned} \partial u/\partial x &= a_{11}\sigma_x - a_{12}\sigma_y \\ \partial v/\partial y &= -a_{12}\sigma_x + a_{22}\sigma_y \\ (\partial u/\partial y) + (\partial v/\partial x) &= (1/\mu_{xy})\tau_{xy} \end{aligned}\right\} \tag{10}$$

where a_{11}, a_{12}, and a_{22} are constants depending on the material properties and on whether the core is taken to be in a state of plane stress or in a state of plane strain [see Eqs. (1.3.3) and (1.3.4), reference 4, page 7]. It should be noted that E_f in Eqs. (3) and (4) is either E or $E/(1 - \nu^2)$, depending on whether the state is one of plane stress or plane strain.

Equilibrium of stresses in the core is satisfied by introducing Airy's stress function φ, such that

$$\left.\begin{aligned} \sigma_x &= \partial^2\varphi/\partial y^2 \\ \sigma_y &= \partial^2\varphi/\partial x^2 \\ \tau_{xy} &= -\partial^2\varphi/\partial x\partial y \end{aligned}\right\} \tag{11}$$

Compatibility of strains is satisfied if

$$\frac{\partial^4\varphi}{\partial x^4} + 2K\frac{\partial^4\varphi}{\partial x^2\partial\eta^2} + \frac{\partial^2\varphi}{\partial\eta^4} = 0 \tag{12}$$

where

$$\eta = \epsilon y$$
$$\epsilon = \sqrt[4]{a_{22}/a_{11}}$$
$$K = (1/2\sqrt{a_{11}a_{22}})\,[(1/\mu_{xy}) - 2a_{12}]$$

A solution of Eq. (12) which satisfies Eqs. (1), (2), and (9) is given by

$$\varphi = (A \sinh \nu_1 y + B \sinh \nu_2 y + C \cosh \nu_1 y + D \sinh \nu_2 y) \sin (m\pi x/L) \tag{13}$$

where

$$\nu_1 = \frac{m\pi\epsilon}{L}\left(\sqrt{\frac{K+1}{2}} + \sqrt{\frac{K-1}{2}}\right)$$
$$\nu_2 = \frac{m\pi\epsilon}{L}\left(\sqrt{\frac{K+1}{2}} - \sqrt{\frac{K-1}{2}}\right)$$

from which

$$\left.\begin{aligned} \sigma_y &= -\left(\frac{m\pi}{L}\right)^2 (A \sinh \nu_1 y + B \sinh \nu_2 y + C \cosh \nu_1 y + D \cosh \nu_2 y) \sin\frac{m\pi x}{L} \\ \tau_{xy} &= -\left(\frac{m\pi}{L}\right)(\nu_1 A \cosh \nu_1 y + \nu_2 B \cosh \nu_2 y + \nu_1 C \sinh \nu_1 y + \nu_2 D \sinh \nu_2 y)\cos\frac{m\pi x}{L} \\ \frac{\partial u}{\partial x} &= \left\{\left[\nu_1^2 a_{11} + \left(\frac{m\pi}{L}\right)^2 a_{12}\right](A \sinh \nu_1 y + C \cosh \nu_1 y) + \left[\nu_2^2 a_{11} + \left(\frac{m\pi}{L}\right)^2 a_{12}\right](B \sinh \nu_2 y + D \cosh \nu_2 y)\right\}\sin\frac{m\pi x}{L} \\ v &= -\left[\frac{\nu_1^2 a_{12} + (m\pi/L)^2 a_{22}}{\nu_1}(A \cosh \nu_1 y + C \sinh \nu_1 y) + \frac{\nu_2^2 a_{12} + (m\pi/L)^2 a_{22}}{\nu_2}(B \cosh \nu_2 y + D \sinh \nu_2 y)\right]\sin\frac{m\pi x}{L} \end{aligned}\right\} \tag{14}$$

The substitution of Eqs. (14) into Eqs. (5) and (6) and the addition and subtraction of these equations yield

$$A\left\{\left(\nu_1\frac{h}{2}\right)^2 a_{11} + \left(\frac{m\pi h}{2L}\right)^2 a_{12} + \left[\frac{1}{2E_f}\frac{h}{t}\nu_1\frac{h}{2} - \frac{t}{h}\left(\frac{m\pi h}{2L}\right)^2\frac{[\nu_1(h/2)]^2 a_{12} + (m\pi h/2L)^2 a_{22}}{\nu_1(h/2)}\right]\coth \nu_1\frac{h}{2} + \right.$$
$$\left. B\left\{\left(\nu_2\frac{h}{2}\right)^2 a_{11} + \left(\frac{m\pi h}{2L}\right)^2 a_{12} + \left[\frac{1}{2E_f}\frac{h}{t}\nu_2\frac{h}{2} - \frac{t}{h}\left(\frac{m\pi h}{2L}\right)^2\frac{[\nu_2(h/2)]^2 a_{12} + (m\pi h/2L)^2 a_{22}}{\nu_2(h/2)}\right]\coth \nu_2\frac{h}{2}\right\} = 0 \tag{15a}$$

$$C\left\{\left(\nu_1\frac{h}{2}\right)^2 a_{11} + \left(\frac{m\pi h}{2L}\right)^2 a_{12} + \left[\frac{1}{2E_f}\frac{h}{t}\nu_1\frac{h}{2} - \frac{t}{h}\left(\frac{m\pi h}{2L}\right)^2\frac{[\nu_1(h/2)]^2 a_{12} + (m\pi h/2L)^2 a_{22}}{\nu_1(h/2)}\right]\tanh \nu_1\frac{h}{2}\right\} +$$
$$D\left\{\left(\nu\frac{h}{2}\right)^2 a_{11} + \left(\frac{m\pi h}{2L}\right)^2 a_{12} + \left[\frac{1}{2E_f}\frac{h}{t}\nu_2\frac{h}{2} - \frac{t}{h}\frac{m\pi h}{2L}\right)^2\frac{[\nu_2(h/2)]^2 a_{12} + (m\pi h/2L)^2 a_{22}}{\nu_2(h/2)}\right]\tanh \nu_2\frac{h}{2}\right\} = 0 \tag{15b}$$

The substitution of Eqs. (14) into Eqs. (3) and (4) and the addition and subtraction of these equations yield

$$A\left\{1+\frac{t}{h}\nu_1\frac{h}{2}\coth\nu_1\frac{h}{2}+\frac{2}{h}\left[\frac{1}{12}E_f t^3\left(\frac{m\pi}{L}\right)^2-P\right]\frac{[\nu_1(h/2)]^2a_{12}+\left(\frac{m\pi h}{2L}\right)^2a_{22}}{\nu_1(h/2)}\coth\nu_1\frac{h}{2}\right\}+$$

$$B\left\{1+\frac{t}{h}\nu_2\frac{h}{2}\coth\nu_2\frac{h}{2}+\frac{2}{h}\left[\frac{1}{12}E_f t^3\left(\frac{m\pi}{L}\right)^2-P\right]\frac{[\nu_2(h/2)]^2a_{12}+\left(\frac{m\pi h}{2L}\right)^2a_{22}}{\nu_2(h/2)}\coth\nu_2\frac{h}{2}\right\}=0 \quad (16a)$$

$$C\left\{1+\frac{t}{h}\nu_1\frac{h}{2}\tanh\nu_1\frac{h}{2}+\frac{2}{h}\left[\frac{1}{12}E_f t^3\left(\frac{m\pi}{L}\right)^2-P\right]\frac{\left[\nu_1\left(\frac{h}{2}\right)\right]^2a_{12}+\left(\frac{m\pi h}{2L}\right)^2a_{22}}{\nu_1(h/2)}\tanh\nu_1\frac{h}{2}\right\}+$$

$$D\left\{1+\frac{t}{h}\nu_2\frac{h}{2}\tanh\nu_2\frac{h}{2}+\frac{2}{h}\left[\frac{1}{12}E_f t^3\left(\frac{m\pi}{L}\right)^2-P\right]\frac{\left[\nu_2\left(\frac{h}{2}\right)\right]^2a_{12}+\left(\frac{m\pi h}{2L}\right)^2a_{22}}{\nu_2(h/2)}\tanh\nu_2\frac{h}{2}\right\}=0 \quad (16b)$$

It is seen that the equations separate into two (sets—Eqs. 15a) and (16a) containing unknowns A and B and corresponding to an antisymmetrical wrinkling mode, and Eqs. (15b) and (16b) containing only the unknowns C and D and corresponding to a symmetrical wrinkling mode. These equations would not have separated with the same sign in front of $\sigma_y(x, h/2)$ and $\sigma_y(x, -h/2)$ in Eqs. (3) and (4). The wrinkling criterions are obtained by setting the determinant of the coefficients of A and B and of C and D in these equations equal to zero (to permit values of A and B or of C and D other than zero). Then

$$\sigma_{crA}=\frac{1}{3}\left(\frac{m\pi h}{2L}\right)^2E_f\left(\frac{t}{h}\right)^2+\frac{1}{2}\frac{h}{t}\frac{\dfrac{1+\frac{t}{h}\nu_1\frac{h}{2}\coth\nu_1\frac{h}{2}}{\alpha_1+\gamma_1\coth\nu_1\frac{h}{2}}-\dfrac{1+\frac{t}{h}\nu_2\frac{h}{2}\coth\nu_2\frac{h}{2}}{\alpha_2+\gamma_2\coth\nu_2\frac{h}{2}}}{\dfrac{\beta_1\coth\nu_1\frac{h}{2}}{\alpha_1+\gamma_1\coth\nu_1\frac{h}{2}}-\dfrac{\beta_2\coth\nu_2\frac{h}{2}}{\alpha_2+\gamma_2\coth\nu_2\frac{h}{2}}} \quad (17a)$$

$$\sigma_{crS}=\frac{1}{3}\left(\frac{m\pi h}{2L}\right)^2E_f\left(\frac{t}{h}\right)^2+\frac{1}{2}\frac{h}{t}\frac{\dfrac{1+\frac{t}{h}\nu_1\frac{h}{2}\tanh\nu_1\frac{h}{2}}{\alpha_1+\gamma_1\tanh\nu_1\frac{h}{2}}-\dfrac{1+\frac{t}{h}\nu_2\frac{h}{2}\tanh\nu_2\frac{h}{2}}{\alpha_2+\gamma_2\tanh\nu_2\frac{h}{2}}}{\dfrac{\beta_1\tanh\nu_1\frac{h}{2}}{\alpha_1+\gamma_1\tanh\nu_1\frac{h}{2}}-\dfrac{\beta_2\tanh\nu_2\frac{h}{2}}{\alpha_2+\gamma_2\tanh\nu_2\frac{h}{2}}} \quad (17b)$$

where

$$\alpha_{1,2}=[\nu_{1,2}(h/2)]^2a_{11}+(m\pi h/2L)^2a_{12}$$
$$\beta_{1,2}=\frac{\{[\nu_{1,2}(h/2)]^2a_{12}+(m\pi h/2L)^2a_{22}\}}{\nu_{1,2}(h/2)}$$
$$\gamma_{1,2}=(1/2E_f)(h/t)\nu_{1,2}(h/2)-(t/h)(m\pi h/2L)^2\beta_{1,2}$$

Eqs. (17a) and (17b) are readily applicable to those sandwich structures for which $K > 1$. For $K < -1$, both ν_1 and ν_2 are pure imaginary quantities, and the equations must be revised by converting the hyperbolic functions of a pure imaginary number into their trigonometric equivalents. For $|K| < 1$, ν_1 and ν_2 are complex, and the complex functions in the right sides of Eqs. (17a) and (17b) must be transformed into their real equivalents. For $|K| = 1$, the criterions can be obtained by finding the limit of Eqs. (17) as $|K| \to 1$. In all cases the resulting values of σ_{cr} are real. In calculating values of σ_{cr}, the right sides of Eqs. (17a) and (17b) must be minimized with respect to the quantity $m\pi h/2L$, which is present in $\nu_1(h/2)$, $\nu_2(h/2)$, α_1, α_2, β_1, β_2, γ_1 and γ_2, for given values of the material constants and geometric properties of the sandwich structure. For a finite value of L, it is necessary to take m equal to the integers 1, 2, 3, ... However, since the wrinkling wave length is small compared with the length L of the column, it is customary to consider L to be infinite and to consider the quantity L/m to be a wave length λ, which may vary continuously. The minimization in this case is probably best done numerically than analytically. However, it might be possible to solve the equation for the analytical minimum for the quantity h/t, thus obtaining corresponding values of σ_{cr} and h/t for given values of the material constants and the buckle wave-length parameter $m\pi h/2L$.

Comparisons may be made with the results of other analyses of the problem. Eqs. (17) are presumably similar to those of references 5 and 6, which investigate the problem with identical assumptions, according to reference 4. The solution of reference 4 is expressible as

$$\left.\begin{aligned}\sigma_{crA}&=\frac{1}{3}\left(\frac{m\pi h}{2L}\right)^2E_f\left(\frac{t}{h}\right)^2+\frac{1}{2}\frac{h}{t}\frac{(1/\alpha_1)-(1/\alpha_2)}{(\beta_1/\alpha_1)\coth\nu_1(h/2)-(\beta_2/\alpha_2)\coth\nu_2(h/2)}\\ \sigma_{crS}&=\frac{1}{3}\left(\frac{m\pi h}{2L}\right)^2E_f\left(\frac{t}{h}\right)^2+\frac{1}{2}\frac{h}{t}\frac{(1/\alpha_1)-(1/\alpha_2)}{(\beta_1/\alpha_1)\tanh\nu_1(h/2)-(\beta_2/\alpha_2)\tanh\nu_2(h/2)}\end{aligned}\right\} \quad (18)$$

In this solution the effect of transmitted shear stresses on bending of the faces is neglected, and relative displacements between the core and faces due to stretching and bending of the faces are permitted. The corrected solution of reference 1 is obtained by placing γ_1 and γ_2 equal to zero in Eqs. (17), in which case the actual location of the juncture of the core and faces is partially taken into account by considering the effect of shear stresses on bending of the faces but allowing relative displacements between the core and faces.

Thus, the problem stated in reference 1 has both the symmetric and antisymmetric wrinkling modes found in other investigations and is readily solvable in terms of simple functions. It should be noted that wrinkling takes place in sinusoidal waves as implied by Eringen's analysis but of which a false impression may have been given by Fig. 1 of his paper. For other boundary conditions for the curve and faces, the elaborate analysis made by Eringen of the boundary value problem with mixed boundary conditions would be necessary, but it is doubtful that an asymmetric buckle pattern would result so long as both faces were of equal thickness, of the same material, and subject to the same boundary conditions.

REFERENCES

[1] Eringen, A. Cemal, *Ripple-Type Buckling of Sandwich Columns*, Journal of the Aeronautical Sciences, Vol. 19, No. 6, pp. 409–417, June, 1952.

[2] Eringen, A. Cemal, *Solution of the Two-Dimensional Mixed-Mixed Boundary Value Problem of Elasticity for Rectangular, Orthotropic Media and Application to the Buckling of Sandwich Beams*, Thesis for Ph.D. in Applied Mechanics, Polytechnic Institute of Brooklyn, June, 1948. (The writer has been unable to obtain this reference.)

[3] Seide, Paul, *The Effect of Longitudinal Stiffeners Located on One Side of a Plate on the Compressive Buckling Stress of the Plate-Stiffener Combination*, NACA TN No. 2873, 1953.

[4] Norris, C. B., Ericksen, W. S., March, H. W., Smith, C. B., and Boller, K. H., *Wrinkling of the Facings of Sandwich Constructions Subject to Edgewise Compression*, Forest Prod. Lab. Rept. 1810, 1949.

[5] Cox, H. L., *Sandwich Construction and Core Materials. Part III, Instability of Sandwich Struts and Beams*, Report No. 9226, Aero Res. Council, December, 1945.

[6] Williams, D., Leggett, D. M. A., and Hopkins, H. G., *Flat Sandwich Panels Under Compressive End Loads*, Rept. A. D. 3174, R.A.E., England, June, 1941.

Spin Effect on Base Pressure of Cone-Cylinders

R. Lehnert and S. M. Hastings
U.S. Naval Ordnance Laboratory, White Oak, Silver Spring, Md.
December 24, 1953

IN THE WIND-TUNNEL TESTING of spin-stabilized missiles, the effect of model rotation on its aerodynamic characteristics usually is disregarded. A few systematic experiments with rotating models have been carried out at subsonic speeds.[1, 2] Similar data at supersonic speeds were preliminary in character.[3]

Experiments were recently carried out at the Naval Ordnance Laboratory to determine the spin effect at zero angle of attack on the stability of the laminar boundary layer and on base pressure at supersonic speeds (Magnus effects are outside the scope of this investigation). A family of five cone-cylinders all having 25° apex angles and 2-in. diameters, varying in total length from $L/D = 6$ to 10, were tested at a Mach Number of 2.86 with spin rates varying from 0 to 43,000 r.p.m. The maximum r.p.m. corresponded to a value of approximately $^1/_6$ for the ratio of circumferential velocity to translational velocity. Spark-schlieren pictures were taken in order to determine the character of the boundary layer and wake flow. It has been shown previously that base pressure depends on the status of the boundary layer at the base,[4, 5] and therefore some correlation between the effect of spin on boundary-layer transition and on base pressure was expected.

Experimental values of the ratio of base pressure to free-stream static pressure are plotted versus Reynolds Number for various spin rates on Fig. 1 (Reynolds Numbers are based on free-stream conditions and the length, along the surface, from the cone tip to the cylinder trailing edge). From spark-schlieren photographs, it was found that the minima of the curves were obtained when boundary-layer transition occurred at the model base. When the boundary layer at the base is laminar (two short models, $L/D = 6$ and 7), increasing the model spin rate produces a considerable decrease in the base-pressure ratio. Spark-schlieren photographs show that the decrease in base pressure was accompanied by an upstream movement of transition in the wake mixing zone with increasing spin rate. This decrease becomes less pronounced when the boundary layer at the base becomes less stable (increasing body length), and the trend reverses when the boundary layer at the trailing edge has become fully turbulent, but the dependency is less pronounced.

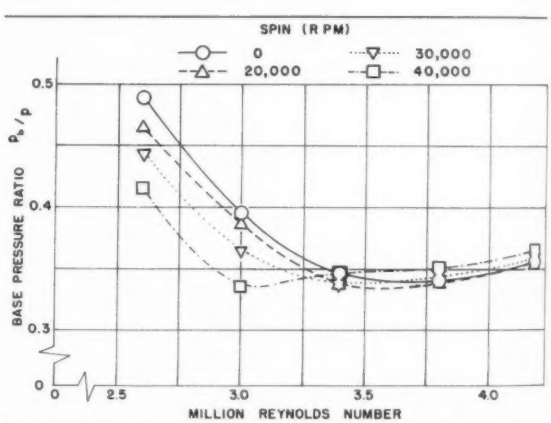

FIG. 1. The effect of spin on base-pressure ratios of 25° cone-cylinders at $M = 2.86$.

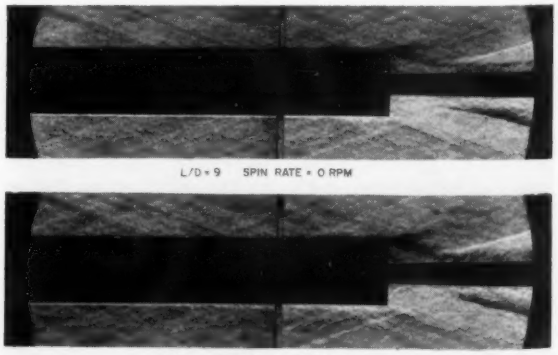

FIG. 2. The effect of spin on the location of boundary-layer transition on 25° cone-cylinders at $M = 2.86$.

The minima of the base-pressure ratio versus Reynolds Number curves occur at lower Reynolds Numbers with increasing spin rate. In addition, increasing the model spin rate from 0 to 43,000 r.p.m. shifted the average transition location on the model upstream by approximately one model diameter, corresponding to a change in Reynolds Number of about 0.5×10^6. The upstream shift of the transition location due to spin can be seen in the photographs of Fig. 2, which are given as an example. Consequently, we conclude that spin destabilizes the laminar boundary layer, thereby promoting transition.

It was feared that vibrations induced by the spinning of the model might have caused a destabilization of the laminar boundary layer. The model vibrations incurred during the spin test were therefore measured and simulated in frequency and amplitude with an electromagnetic vibrator. Base pressure and transition location were then measured on the nonspinning model and found to be independent of model vibration.

References

[1] Wieselsberger, C., *Ueber den Luftwiderstand bei gleichzeitiger Rotation des Versuchskoerpers*, Physikalische Zeitschrift, p. 84, 1927.

[2] Sann, B., *Widerstands-und Bodendruck-messungen an rotierenden Langgeschossen bei Unterschallgeschwindigkeit*, Deutsche Luftfahrtforschung Forschungsbericht Nr. 1048, ZWB/FB/1048, 1939.

[3] Lehnert, R., *Dreikomponenten-messungen am Modell einer 28 cm Sprenggranate fuer das Ferngeschuetz K 5*, Peenemuende Archive Report No. 66/68, 1942.

[4] Kurzweg, H. H., *Interrelationship Between Boundary Layer and Base Pressure*, Journal of the Aeronautical Sciences, Vol. 18, No. 11, p. 743, November, 1951.

[5] Chapman, D. R., *An Analysis of Base Pressure at Supersonic Velocities and Comparison with Experiment*, NACA TN No. 2137, July, 1950.

Buckling Loads for Columns of Variable Cross Section

B. E. Gatewood

Mechanics Department, USAF Institute of Technology, Wright-Patterson Air Force Base, Ohio

December 24, 1953

TIMOSHENKO[1] HAS DISCUSSED buckling of bars of variable cross section and has given tables for buckling coefficients for certain taper ratios and for certain types of cross section. This note presents curves for the buckling coefficient for all taper ratios and for any moment of inertia variation between constant and the sixth power. From Fig. 1, the taper ratio is defined as

$$\alpha = a/(a + l) \tag{1}$$

and the parameter m for moment of inertia (I) variation is defined by

$$I = I_1(x/a)^m \tag{2}$$

where for solid section $m = r + 3s$ with x^r the width variation and x^s the thickness variation. These variations are restricted to give minimum I about same axis for entire length.

With the coordinate system of Fig. 1, the differential equation for the deflection y is

$$x^m y'' + q^2 y = 0, \quad q^2 = \frac{Pa^m}{EI_1} \tag{3}$$

This can be written as Bessel's equation

$$t^2 v'' + tv' + (t^2 - n^2)\, v = 0 \tag{4}$$

where

$$y = \sqrt{x}\, v, \quad t = 2nqx^{-1/2n}, \quad n = \frac{1}{m - 2} \tag{5}$$

Thus

$$y = \sqrt{x}\,[AJ_n(t) + BY_n(t)] \tag{6}$$

in which $J_{-n}(t)$ may replace $Y_n(t)$ if n is not a whole number. For $m = 2$,

$$y = \sqrt{x}\,(A \exp\{i[q^2 - (1/4)]^{1/2} \log (x/a)\} + B \exp\{-i[q^2 - (1/4)]^{1/2} \log (x/a)\})$$

With boundary conditions $y = 0$ at $x = a$ and $y' = 0$ at $x = a + l$, the determinant for calculation of the buckling coefficient can be written as

$$J_n(2pn)\, Y_{n+1}(2pn\, \alpha^{1/2n}) - J_{n+1}(2pn\, \alpha^{1/2n})\, Y_n(2pn) = 0 \tag{7}$$

where J_{-n} may replace Y_n (n not integer) and

$$p^2 = Pa^2/EI_1 = q^2 a^{-1/n} \tag{8}$$

For given m and α, p can be obtained from Eq. (7). The results are shown in Fig. 1 for all α from 0 to 1 and m from 0 to 6, where

$$\left.\begin{aligned} P_{cr} &= \frac{\pi^2}{4}\frac{kEI_2}{l^2}, \quad \frac{\pi^2}{4}k = p^2(1 - \alpha)^2 \alpha^{m-2}, \text{ solid curves} \\ P_{cr} &= (2\pi^2)\frac{kEI_1}{a^2}, \quad 2\pi^2 k = p^2, \text{ dashed curves} \end{aligned}\right\} \tag{9}$$

Fig. 2 shows a cross plot of k against m with α as parameter.

Note that, for any m which makes n a multiple of one-half (such as $^4/_3$, $^8/_3$, $^8/_5$, 4), Eqs. (6) and (7) reduce to trigonometric expressions. For $m = 4$, Eqs. (6) and (7) are

$$\left.\begin{aligned} y &= x[A \cos (q/x) + B \sin (q/x)] \\ \tan p(1 - \alpha) &= -p\alpha \end{aligned}\right\} \tag{10}$$

Boyd[2] obtained this result of Eq. (10) by direct change of variable and made tests on steel pin-ended columns (both ends tapered) for $m = 4, 3$, and 1. The test results agree closely with the theoretical buckling load.

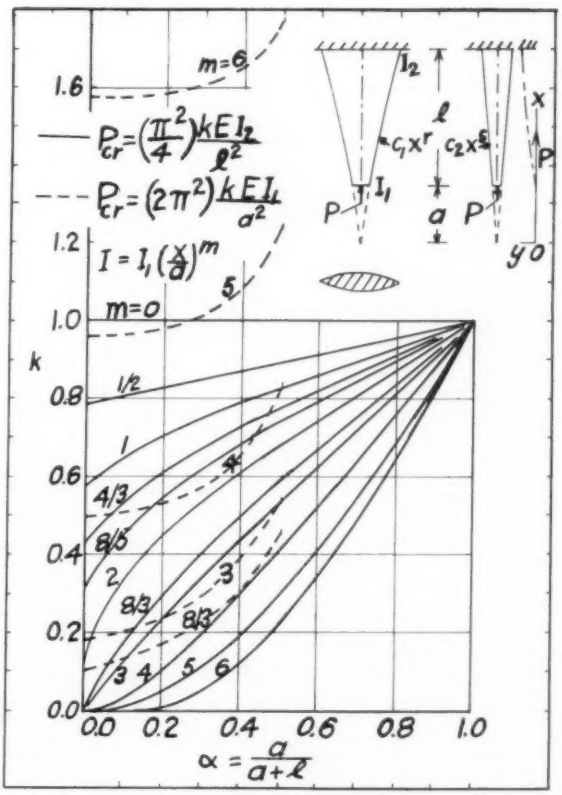

FIG. 1. Variation of buckling coefficient with taper ratio α.

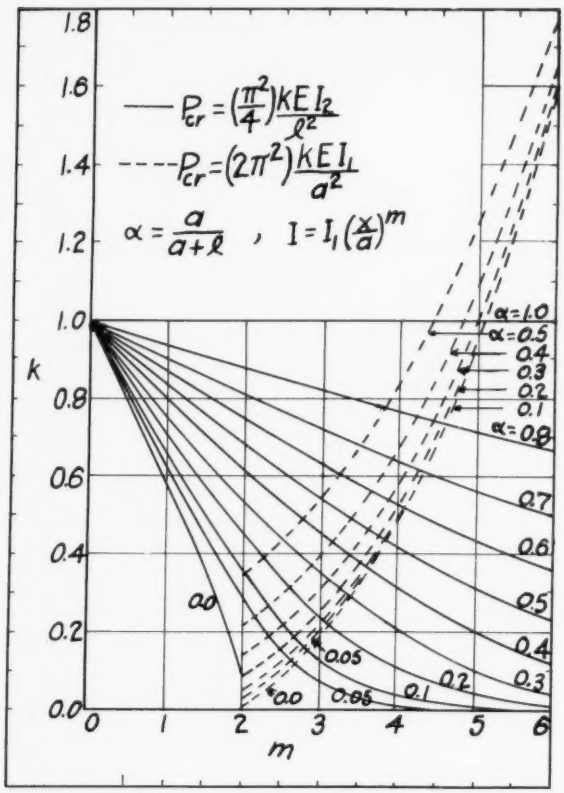

FIG. 2. Variation of buckling coefficient with parameter m.

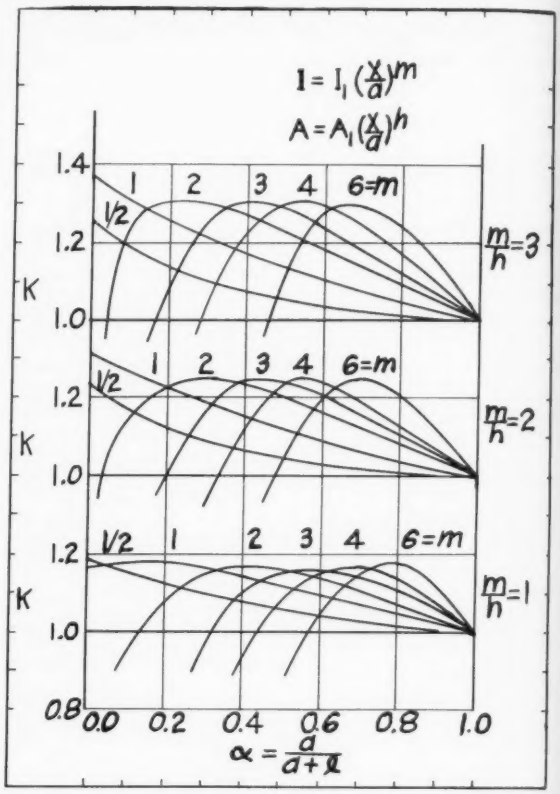

FIG. 3. Maximum values of K for minimum weight.

For design with given load, given length, and given type section, an interesting question is what value of the taper ratio α gives the column of least weight. If $A = A_1(x/a)^h$, then the average area is

$$A_0 = \frac{A_1}{(h+1)\alpha^h}\,\frac{1-\alpha^{h+1}}{1-\alpha} \tag{11}$$

whence, from Eq. (2), the moment of inertia corresponding to this average area is

$$I_0 = I_1\left(\frac{A_0}{A_1}\right)^{m/h} = I_2\left[\frac{1-\alpha^{h+1}}{(h+1)(1-\alpha)}\right]^{m/h} \tag{12}$$

Take $kI_2 = KI_0$, Eq. (9), whence

$$K = k\,\frac{(h+1)(1-\alpha)^{m/h}}{1-\alpha^{h+1}} \tag{13}$$

Now m and h are related through the width and thickness equations, c_1x^r and c_2x^s of the column. For solid columns $h = r + s$, $m = r + 3s$, and since $r \geq 0$, $s \geq 0$, Fig. 1,

$$1 \leq m/h \leq 3 \tag{14}$$

Fig. 3 shows values of K, Eq. (13), in regions of peak values for $m/h = 1$, 2, and 3. For given r and s, or m and h, read maximum K and corresponding α from Fig. 3; then Eqs. (9), (11), (12), and (13) give the column dimensions. A_1 may be restricted by $P/A_1 \leq$ yield stress of material; r and s are restricted in that minimum I should be about same axis over entire length. For constant load and constant length, the weight of the tapered column to the weight of the constant cross-section column is

$$W_t/W_c = K^{-h/m} \tag{15}$$

For round thin-walled columns, $m/h = 3$, and Eq. (15) checks Feigen's[3] results on tapered thin-walled columns for $m = 1$, 2, 3, and 4.

Recently, several authors[4–7] have considered stepped columns. In some cases the stepped column may be approximated by a continuous tapered column such as discussed above. A curve can be put through three points on the stepped column to determine α and m, whence k can be read from Fig. 1 or 2. For instance, in the example in Ram and Rao's paper,[7] use the three points $I_1/I_1 = 1$ at the wall, $I_2/I_1 = 0.81$ at $3L/8$ from wall, and $I_4/I_1 = 0.36$ at the tip to get $\alpha = 0.17$, $m = 0.56$, whence $k = 0.82$ or $(\pi^2/4)k = 2.02$; their result is 2.019. Also, columns with different taper ratios in several regions may be approximated by one taper ratio.

REFERENCES

[1] Timoshenko, S., *Theory of Elastic Stability*, pp. 128–139; McGraw-Hill Book Company, Inc., New York, 1936.

[2] Boyd, James E., *Tapered Struts, A Theoretical and Experimental Investigation*, Bulletin No. 25, The Engineering Experiment Station, The Ohio State University, September, 1923.

[3] Feigen, Morris, *Minimum Weight of Tapered Round Thin-Walled Columns*, Journal of Applied Mechanics, Vol. 19, No. 3, pp. 375–380, September, 1952.

[4] Hoblit, Frederic M., *Buckling Load of a Stepped Column*, Journal of the Aeronautical Sciences, Vol. 18, No. 2, pp. 124–126, 138, February, 1951.

[5] Silver, Gordon, *Critical Loads on Variable-Section Columns in the Elastic Range*, Journal of Applied Mechanics, Vol. 18, No. 4, pp. 414–420, December, 1951.

[6] Thomson, William T., *Matrix Solution of the n-Section Column*, Journal of the Aeronautical Sciences, Vol. 16, No. 10, pp. 623–624, October, 1949.

[7] Ram, G. Sri, and Rao, G. B. R., *Buckling of an N-Section Column*, Journal of the Aeronautical Sciences, Vol. 19, No. 1, pp. 66–67, January, 1952.

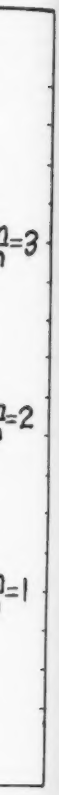

checks
1, 2,

l col-
nated
re. A
mn to
For
three
l, and
e k =
lumns
proxi-

w-Hill

Investi-
e Ohio

d Col-
ember,

of the
1.
Elastic
Decem-

rnal of

ournal